TECHNISCHE UNIVERSITÄT MÜNCHEN

Fakultät für Maschinenwesen

Lehrstuhl für Aerodynamik und Strömungsmechanik

Numerical Simulation of Submerged Cavitating Throttle Flows

Bruno Beban

Vollständiger Abdruck der von der Fakultät für Maschinenwesen der Technischen Universität München zur Erlangung des akademischen Grades eines

Doktor-Ingenieurs

genehmigten Dissertation.

Vorsitzender:		Prof. Dr.-Ing. Georg Wachtmeister
Prüfer der Dissertation:	1.	Prof. Dr.-Ing. Nikolaus A. Adams
	2.	Prof. Dr.-Ing. Romuald Skoda, Ruhr-Universität Bochum

Die Dissertation wurde am 06.06.2018 bei der Technischen Universität München eingereicht und durch die Fakultät für Maschinenwesen am 18.02.2019 angenommen.

Bruno Beban: *Numerical Simulation of Submerged Cavitating Throttle Flows*

Typesetting: LaTeX

To my grandfather Frane Beban.

Acknowledgements

First of all, I would like to express my sincere gratitude to my academic supervisor Prof. Dr.-Ing. Nikolaus Adams for giving me an opportunity for a research in the field of computational fluid dynamics. I greatly appreciate the freedom and support provided during my time at the Institute of Aerodynamics and Fluid Mechanics. Many thanks go to Prof. Dr.-Ing. Romuald Skoda from the Ruhr-Universität Bochum for willingly accepting the role of the second examiner of my dissertation. I would also like to thank Prof. Dr.-Ing. Georg Wachtmeister for chairing the examination committee.

A special thanks goes to Steffen, whose support and advices helped a lot to shape this work to its final form and for sharing his knowledge and expertise. I thank my fellow office mates Bernd and Theresa for the intense collaboration and stimulating discussions. It was a privilege working with you. Furthermore, many colleagues from the institute made my Ph.D. life easier – I am grateful to all of you with whom I have had the pleasure to work during this and other related projects.

I would also like to thank Olga Granić for carefully proofreading my dissertation.

And finally, a big thank goes to my family for all their encouragement and to my wife Ivana for her love, patience and unconditional support.

Abstract

Strict emission policies in the automotive Diesel sector push the optimization of injector components to the limit and drive the necessity to gain a deeper and more detailed insight into the flow dynamics of those systems. The main objective of this work is to enhance the understanding of cavitating flow dynamics in micro throttles, which are building blocks of every common rail injector. *CATUM*, the in-house tool developed at the Institute of Aerodynamics and Fluid Mechanics of Technische Universität München, provides a computational framework for high-fidelity computational fluid dynamics. In the present work, our contribution focuses on comprehensive investigations of canonical flow configurations at industry-relevant spatial scales and operating conditions in the valve chamber of a common rail injector. For this purpose, we utilize a fully compressible flow description in combination with the thermodynamic equilibrium model. The equation of state for Diesel calibration fuel ISO 4113 is proposed and extended with a non-condensable gas component. In the first set of investigations, different geometries of discharge throttles are examined, revealing a high-frequency cavity pulsation in the throttle, with a simultaneous development of the classic re-entrant jet and the bubbly shock. Erosion mechanisms responsible for the high pressure peaks on the material surfaces are identified as well. Simulations which include valve chamber configuration with a step-hole mounted on the throttle detect coupling between the intrinsic shedding instabilities emanating from the throttle and the collapse-driven development of pressure waves from the step-hole. The second part of investigations includes a separate assessment of non-condensable gas and turbulence on cavity dynamics. A possibility of pseudo-cavitation for high gas amount added to the working fluid is demonstrated. Computations with the novel ILES approach for cavitating flow simulation show qualitatively the same flow topology as inviscid simulations and an alteration of cavity dynamics.

Kurzfassung

Durch strenge Abgasrichtlinien für Dieselfahrzeuge wird die Optimierung von Injektorkomponenten bis an ihre Grenzen getrieben. Dies macht es notwendig, einen tieferen und detaillierteren Einblick in die Strömungsdynamik solcher Systeme zu gewinnen. Das Ziel der vorliegenden Arbeit ist es, die Kavitationsdynamik in Mikrodrosseln als Komponenten eines jeden Common-Rail-Injektors besser zu verstehen. In diesem Zusammenhang ermöglicht der am Lehrstuhl für Aerodynamik und Strömungsmechanik der Technischen Universität München entwickelte Strömungslöser CATUM eine zeitlich hochauflösende numerische Strömungssimulation. Die vorliegende Arbeit konzentriert sich auf die Untersuchung von kanonischen Strömungskonfigurationen mit industrierelevanten räumlichen Skalen und Betriebsbedingungen in der Ventilkammer eines Common-Rail-Injektors. Hierfür wird eine vollständig kompressible Strömungsbeschreibung in Kombination mit dem thermodynamischen Gleichgewichtsmodell verwendet. Genauer wird vorgeschlagen, die Zustandsgleichung für Diesel-Kalibrierungskraftstoff ISO 4113 einzusetzen und um die nicht kondensierbare Gaskomponente zu erweitern. Im ersten Teil der Untersuchung werden unterschiedliche Ablaufdrosselgeometrien untersucht, die eine hochfrequente Kavitätspulsation in der Drossel bei gleichzeitiger Bildung des klassischen Reentrant-Jets und des Kondensationsstoßes erzeugen. Weiterhin werden Erosionsmechanismen identifiziert, die für hohe Druckspitzen auf Bauteiloberflächen verantwortlich sind. In Simulationen, die eine Ventilkammerkonfiguration mit einem an der Drossel angebrachten Stufenloch abbilden, wird eine Kopplung zwischen den von der Drossel ausgehenden intrinsischen Shedding-Instabilitäten und der kollapsgetriebenen Entwicklung von Druckwellen aus dem Stufenloch identifiziert. Der zweite Teil der Untersuchung umfasst eine separate Bewertung des Einflusses von nicht kondensierbarem Gas und Turbulenz auf die Kavitation. Ferner wird die Möglichkeit der Pseudokavitation für hohe Gasmengen dargestellt, die dem Arbeitsfluid zugesetzt werden. Berechnungen mit

dem neuartigen ILES-Ansatz für kavitierende Strömungssimulationen zeigen qualitativ die gleiche Strömungstopologie wie die reibungsfreien Simulationen und eine Veränderung der Kavitationsdynamik.

Contents

Acknowledgements **i**

Abstract **iii**

Kurzfassung **v**

List of Figures **xi**

List of Tables **xvii**

1 Introduction **1**

1.1 Background and Motivation 1

1.2 Common Rail Injection System 3

1.3 State-of-the-Art 4

1.3.1 Experimental Research 5

1.3.2 Numerical Research 7

1.4 Objective of the Present Work 9

2 Fundamentals of Cavitation **11**

3 Numerical Method and Physical Model **17**

3.1 Numerical Method 17

3.1.1 Governing Equations 17

3.1.2 Finite Volume Method 19

3.2 Single-Fluid Cavitation Model for ISO 4113 Fuel 22

3.2.1 Liquid 23

3.2.2 Liquid-vapor mixture 25

3.3 Extension of the Single-Fluid Cavitation Model with Non-Condensable Gas Component 25

4 Flow in the Realistic Valve Chamber and Derivation of a Generic Model 29

4.1 Realistic Valve Chamber 29

4.1.1 Geometrical Model 29

4.1.2 Computational Setup and Numerical Grids 31

4.1.3 Results and Discussion 33

4.1.4 Erosion Assessment 38

4.2 Generic Model 40

4.3 Summary 42

5 Influence of Throttle Geometry 43

5.1 Computational Setup 43

5.2 Discharge Properties and Characterization of the Throttle Flow 44

5.3 Flow Field Topology 46

5.4 Grid Sensitivity Study 47

5.5 Analysis of Cavity Dynamics 52

5.5.1 Frequency Spectra 55

5.5.2 Strouhal Numbers and Estimation of the Re-entrant Velocity 55

5.6 Erosion Assessment 60

5.6.1 Wall Loads 60

5.6.2 Collapse Spectra 63

5.7 Summary 64

6 Influence of the Step-hole Diameter on the Cavity Dynamics 67

6.1 Computational Setup 67

6.2 Results 69

6.2.1 Instantaneous Flow Field 70

6.2.2 Erosion Assessment 76

6.3 Summary 81

7 Effects of Non-condensable Gas and Turbulence on the Throttle Flow **83**

7.1 Non-condensable Gas Effects 83

7.1.1 Estimation of the Non-condensable Gas Content 83

7.1.2 Computational Setup 85

7.1.3 Results 85

7.2 Turbulence Effects 89

7.2.1 Computational Setup 89

7.2.2 Results 91

7.3 Summary 94

8 Summary and Conclusion **97**

A Appendix **101**

A.1 Equilibrium Speed of Sound in Cavitating Flow 101

A.2 Cavity Dynamics in *Standard Diesel* Case 103

Bibliography **112**

List of Figures

1.1 Operating principle of a piezo common rail injector. Modified from Bartsch [6]. Red: High-pressure zone, Blue: Low-pressure zone. 4

2.1 Example of a phase diagram for one-component fluid. 12

2.2 (a)-(c) Different types of cavitation observed at NACA 16012 hydrofoil by Franc and Michel [42]. (b) Tip vortex cavitation at the model ship propeller [2]. 14

2.3 Experimental sequence of growth and non-spherical cavity collapse in the vicinity of a solid wall [107]. 15

2.4 (a) Cavitation damage on a propeller blade [74], (b) damage at the discharge throttle inlet of a fuel injector [108]. 15

3.1 Sketch of a four-cell stencil utilized in the numerical method. Numerical flux is computed through the gray area. 19

3.2 Barotropic relation between pressure and density for the test fluid ISO 4113. The dashed line depicts the equation of state for the variable temperature, whereas solid lines correspond to the equation of state for fixed temperatures. Symbols denote experimental measurements by Chorążewski et al. [27]. 24

3.3 Homogeneous mixture representation in the computational cell. 26

4.1 Utilized valve chamber of the common rail injection system. 30

4.2 *Level* 1 grid of the realistic valve chamber: (a) slice through the mid-plane; (b) blocking topology of the computational domain; (c) magnified view of the grid in the valve chamber. 32

4.3 Temporal evolution of the global vapor volume for operating points *OPA* (–), *OPB* (– –) and *OPC* (–.). Initial development of the flow field is shown only for *OPA* (left side of the figure). 33

4.4 Time-averaged topology of the flow field on the example of *OPA*. 35

4.5 Instantaneous snapshots of vapor volume fraction iso-contours $\alpha = 10\%$ colored by absolute velocity (left). Absolute velocity contours in the mid-plane (right). (a)-(b) *OPA*, (c)-(d) *OPB*, (e)-(f) *OPC*. 36

4.6 Detected wall loads on the pilot valve. (a) *OPA*, (b) *OPB*, (c) *OPC*. 39

4.7 (a) Detected collapse events on the example of OPA. Each event is depicted by a sphere whose size and color scales with the collapse pressure. (b) Cumulative rate of collapse events in the computational domain for investigated operating points. 39

4.8 Sketch of the generic valve chamber model. All dimensions are given in millimeters. 41

4.9 Sketches of generic throttle designs. Designs D and E feature a sharp-edged cylindrical throttle and a step-hole mounted on top of it. 41

5.1 Computational model of the generic valve chamber. 44

5.2 Top: Effect of the cavitation number on the discharge characteristics of the throttles. The solid line depicts theoretical behavior of the discharge for the sharp-edged throttle [80]. Bottom: OP1–cavitation inception, OP2–critical cavitation point (CCP), OP3–supercavitating regime, on the example of Design A. . 46

5.3 Time-averaged topology of the flow field on the example of Design A. 47

5.4 Topology of the block-structured grid and resolution at the *Level 3* grid. 48

5.5 Resolution of the throttle at different grid levels. Top: $Level$ 1, Middle: $Level$ 2, Bottom: $Level$ 3. 49

5.6 Temporal evolution of the vapor volume in the throttle (normalized with the throttle volume) and mass flow rate at the throttle exit at different grid resolutions. Diagrams on the right hand side show the time-averaged values of the relevant quantities. 50

5.7 Resolution of the cavitating sheet in the vicinity of the throttle intake at different grid levels. 51

5.8 Pre-multiplied power spectral density of the mass flow rate at the throttle outlet (top) and vapor volume in the throttle (bottom) for three different grid resolutions. 52

5.9 Temporal evolution of mass flow rate (blue curve) and vapor volume (green curve) during the time period $T = 0.05$ ms. Gray areas mark the cavity oscillation period. 54

5.10 Representative snapshots during one shedding cycle in Design A. Time instants (a)-(f) are marked in Fig. 5.9a. Instantaneous velocity w shown at mid-plane together with iso-surfaces of vapor volume fraction $\alpha = 10\%$. 56

5.11 Pre-multiplied power spectral density of the mass flow rate at the throttle outlet (top) and vapor volume in the throttle(bottom). 57

5.12 Space-time plot of the void fraction α in the vicinity of the throttle wall. The estimated velocities of the re-entrant motion are shown as well. 59

5.13 Temporal evolution of the integrated vapor volume in the throttle (green curve) shown together with the recorded collapse pressure (red bars). 61

5.14 Instantaneous snapshots of vapor cloud collapse in the discharge throttle of Design A. Disintegration of two vapor fragments (labeled with *I* and *II*) at different positions in the throttle is depicted. Footprints of the maximal wall loads are shown together with iso-contours of $\alpha = 10\%$. Start time $t = 1.5389$ ms, $\Delta t \approx 66 \cdot 10^{-9}$ *s*. 62

5.15 Distribution of the wall loads during the time interval $\Delta t = 0.2$ ms. 63

5.16 Convergence of cumulative collapse rates. Left: whole domain, Right: throttle . 65

5.17 Cumulative collapse rates. Left: whole domain, Right: throttle 65

6.1 Computational grid: (a) isometric view of the entire domain on the example of Design D (b) and (c) details of the fine grid in the throttle and step-hole region of Design D and Design E. Every fourth grid line is shown. 68

6.2 Temporal evolution of the mass flow rate at the throttle exit (solid blue curve) and vapor volume in the throttle (dashed green curve) for Design D. 70

6.3 Representative snapshots during one shedding cycle of Design D. Time instants (a)-(i) are marked in Fig. 6.2. Instantaneous streamwise velocity shown at mid-plane together with iso-surfaces of vapor volume fraction $\alpha = 10\%$, $\Delta t_{(a)-(i)} = 9.6 \cdot 10^{-6}$ s. 71

6.4 Representative snapshots depicting simultaneous development of the re-entrant jet and the bubbly shock in the throttle of Design D. (a)-(b) Propagation of the re-entrant jet on the lower throttle side, followed by the consecutive development of the bubbly shock (c)-(d). Instantaneous streamwise velocity shown at mid-plane together with iso-surfaces of vapor volume fraction $\alpha = 10\%$. 73

6.5 Estimation of the propagation velocity of the bubbly shock based on the vapor volume fraction contour plot. For each cell along the throttle wall, vapor volume fraction is averaged in the circumferential direction. The horizontal axis represents position and the vertical axis time. A dashed line on the diagram depicts a coherent collapse of the cavity sheet in the throttle for the case where reverse flow is dominated by the bubbly shock only. Velocity of the front is estimated to approximately 200 m/s. 73

6.6 Propagation of the pressure wave front in the throttle of Design D. Instantaneous pressure at the mid-plane, two-phase regions identified by the iso-surfaces of vapor volume fraction $\alpha = 10\%$, $\Delta t_{frame} = 2.2 \cdot 10^{-7}$ s. 74

6.7 Representative snapshots depicting the collapse of the toroidal vapor cloud in the step-hole of Design E. Instantaneous pressure at mid-plane together with iso-surfaces of vapor volume fraction $\alpha = 10\%$, $\Delta t_{(a)-(d)} = 2 \cdot 10^{-6}$ s. Two slices at xy-plane depict the cavitation-free liquid core of the high-speed jet. 76

6.8 Premultiplied power spectral density of the mass flow rate (left) and vapor volume (right). 77

6.9 Visualization of the cloud fragmentation and propagation of the shock fronts in the step-hole. Instantaneous static pressure at mid-plane and iso-surfaces of vapor volume fraction $\alpha = 10\%$, $\Delta t_{frame} = 6.3 \cdot 10^{-8}$ s. 77

6.10 Detected collapse events in Design D (left) and Design E (right). Each event is depicted by the sphere whose size and color scales with the collapse pressure. Collapses with intensity less than 0.2 GPa are not shown. 79

6.11 Temporal evolution of the integrated vapor volume in the throttle and step-hole V_{vap} (green curve) shown together with the recorded collapse pressure (red bars) for Design D and Design E. 80
6.12 Recorded surface loads in Design D (left) and Design E (right) during 0.2 ms. . 80
6.13 Coverage of the throttle and step-hole surfaces with the recorded wall pressure exceeding a certain threshold. 81

7.1 Effect of the prescribed fixed amount of non-condensible gas on the mixture density. 85
7.2 Time-averaged mixture density $\langle\rho\rangle$ at the mid-plane of the throttle. 86
7.3 Temporal evolution of the vapor volume in the throttle. 87
7.4 Pre-multiplied power spectral density of the mass flow rate at the throttle outlet (left) and the vapor volume in the throttle (right). 88
7.5 Cumulative collapse rates. Left: whole domain, Right: throttle 88
7.6 Computational grid at two refinement levels. Left: *Level 1* grid , right: *Level 2* grid. 90
7.7 Wall-normal resolution in the throttle. Left: *Level 1* grid, right: *Level 2* grid. . . . 90
7.8 Grid convergence of time-averaged quantities near throttle wall. Time-averaged velocity component $\langle w\rangle$ is plotted at the throttle exit as well. 91
7.9 Temporal evolution of the vapor volume in the throttle at both grid levels. . . . 91
7.10 Snapshots of the flow field during one cavity cycle. Instantaneous velocity w shown at mid-plane together with iso-surfaces of vapor volume fraction $\alpha = 10\%$. 92
7.11 Variation of the mean free path for different values of the vapor volume fraction α on the example of water vapor (blue curve) and Diesel calibration fuel (brown curve). 94

A.1 Equilibrium speed of sound for two-phase flow (blue curve) and the mixture viscosity (green curve) for different values of vapor volume fration α. 102
A.2 Representative snapshots during one shedding cycle in *Standard Diesel* case. Instantaneous velocity shown at mid-plane together with iso-surfaces of vapor volume fraction $\alpha = 10\%$. 103

List of Tables

3.1 Parameters for the liquid equation of state of the ISO 4113 test fuel. 23

3.2 Parameters for Eq. 3.19 24

4.1 Grid parameters for the investigated throttle configurations. 31

4.2 Investigated operating points. 32

4.3 Static pressures and jet velocities at the throttle exit. 37

4.4 Geometric properties of investigated throttle designs. 42

5.1 Grid parameters for investigated throttle configurations. $N_{cells,l}$-number of the cells along the throttle length, $N_{cells,d}$-number of cells across the throttle diameter, Δ_{wall}-height of the first near-wall cell. 48

5.2 Computational costs associated with different grid resolutions required for computation of 1 ms physical time. 51

5.3 Strouhal numbers St based on the estimated shedding frequency f_s, re-entrant flow velocity v_c and discharge throttle length. 58

7.1 Prescribed free gas contents. 84

7.2 Parameters of the utilized grids. 89

A.1 Thermodynamic properties of water at $T = 293.15$ K. 102

1 Introduction

1.1 Background and Motivation

Diesel engines, named after their inventor Rudolf Diesel, are internal combustion (IC) engines with widely and well established application in marine, railroad and road transportation vehicles. IC engines convert chemical energy stored in a fuel (Diesel or gasoline) by burning the fuel-air mixture within the cylinders. A Diesel engine compresses the air required for combustion, which raises gas temperature to the level which is sufficient for Diesel fuel to self-ignite when it is injected into the cylinder. A gasoline IC engine dominated the car sector for a long time, but after the introduction of a direct injection by Audi in 1989, and high pressure systems such as unit injector and common rail technology in the late 1990s, a new era of the Diesel engine had begun. These technological advancements have not only made it possible to tremendously increase the performance characteristics and efficiency of Diesel passenger cars but have also made them attractive to customers, reaching up to 50 % of new registrations in Europe [93].

During the past decade, European legislative bodies have imposed significant restrictions on the emission level of Diesel injections systems, thus challenging car manufacturers and suppliers to reduce pollution. Whereas EURO 4 (2005) standard for light duty vehicles limited emissions of nitrogen oxides (commonly referred to as NO_X) to 0.25 g/km and that of particulate matter (PM) to 0.025 g/km, the current EURO 6 (2014) reduces exhaust limits by approximately 70 % for NO_X and 80 % for PM [1]. Therefore, complex and novel strategies are

emerging in the automotive sector in order to conform to imposed polices.

Reduction of exhaust emissions can be classified into engine measures and downstream measures, which are frequently referred to as exhaust gas treatment. Since technical improvement of direct injection systems, one typical engine measure has become to increase the injection pressure. Nowadays, maximum injection pressure of current common rail injection systems in passenger cars reaches up to 3000 bar, with the tendency to additionally increase. This measure improves spray quality due to the enhanced atomization and dramatically reduces particulate emission, as less soot is produced in the combustion process [87]. Moreover, the whole injection process is the subject of a continuous improvement and optimization. As the increase of the injection pressure raises noise emission level, the fuel injection is usually split into pre-injection and main injection – the whole commonly known as a pilot injection. Furthermore, the start of injection and fuel quantity have to be optimized to the engine operating point – not only to reduce pollution, but also to optimize fuel consumption. Another effective engine measure which is nowadays implemented is the exhaust gas recirculation (EGR), which significantly reduces NO_X. Such advanced engine management is only achievable by using electronic control units, which have become standard in Diesel engines.

Downstream measures imply all apparatus installed in the exhaust gas system with the function to reduce engine emissions. This includes catalytic converters, Diesel particulate filters, sensors and auxiliary subsystems located downstream of the engine. However, for the efficient emission reduction, a coupling between engine and exhaust gas measures is inevitable.

Injection pressures of up to 3000 bar, coupled with small geometric dimensions of nozzles and throttles lead to high flow accelerations and promote the formation of vapor cavities in the injector components. However, cavitation in Diesel injection systems can have beneficial as well as detrimental effects. It is well known that cavitation-induced disturbances enhance fuel atomization and mixing process [94, 104]. Another benefit of nozzle cavitation is a deposit removal, since accumulation of sediment at the nozzle walls deteriorates spray quality and increases fuel consumption and emissions [19]. If the surrounding static pressure is higher than the saturation pressure of the liquid, vapor cavities collapse. The collapse of a cavity produces extremely high pressure pulses and leads to the formation of shock waves

[91, 86]. Early experimental work of Benjamin and Ellis [16] showed that, beside violent shock development, micro-jets arise due to the asymmetry of the cavities – these phenomena have been subject of numerous studies [e.g. 41, 67]. Repeated collapses in the proximity of solid walls will produce high surface loads, which can eventually lead to material erosion [43, 79, 70]. Erosive processes can thus alter the initial nozzle design and affect overall injector performance.

1.2 Common Rail Injection System

The common rail injection system is an advanced injection system that decouples fuel injection from the pressure generation. High pressure pump generates pressure separately from the injection cycle and stores it in the rail, which acts as a pressure accumulator. Thus, independent variation of pressure which is adjusted to the operating point is possible. The key components are the fuel injectors, which are connected with the short high pressure lines to the common fuel rail. Fuel injectors are equipped either with solenoid valves or piezo actuators that enable fast opening and closing of the nozzle, usually with several pre-injections. This features have made the common rail system appealing to the passenger car market, which strives towards more economic and environmentally friendly Diesel engines.

Figure 4.1 depicts a piezo common rail injector. Piezo common rail injectors are fitted with a piezoelectric actuator (1), which translates electrical signal received from the engine control unit into the working stroke. In the figure, red color corresponds to the high-pressure zone (fuel supply), whereas blue color represents low-pressure regions (fuel return). In its closed state, the piezo actuator is in the starting position and the valve mushroom (9) of the pilot valve (10) is closed. In this state, the piston chamber (11) is disconnected from the valve chamber (12) by the sealing seat (5). The nozzle needle (2) is suited in the lower part of the injector and is connected by the control piston (3) to the high-pressure control chamber (6). When the piezo actuator expands longitudinally, it transfers the motion via the valve piston (13) on the valve mushroom of the pilot valve. The valve mushroom thus exerts a force on the return spring (4), and the sealing seat between the piston chamber and the valve chamber opens. Fuel starts to flow through the discharge throttle (7) and pressure in the control chamber immediately decreases. Since the nozzle needle is subjected to the rail pressure of

the high-pressure chamber (8), the nozzle needle moves upwards and fuel injection begins.

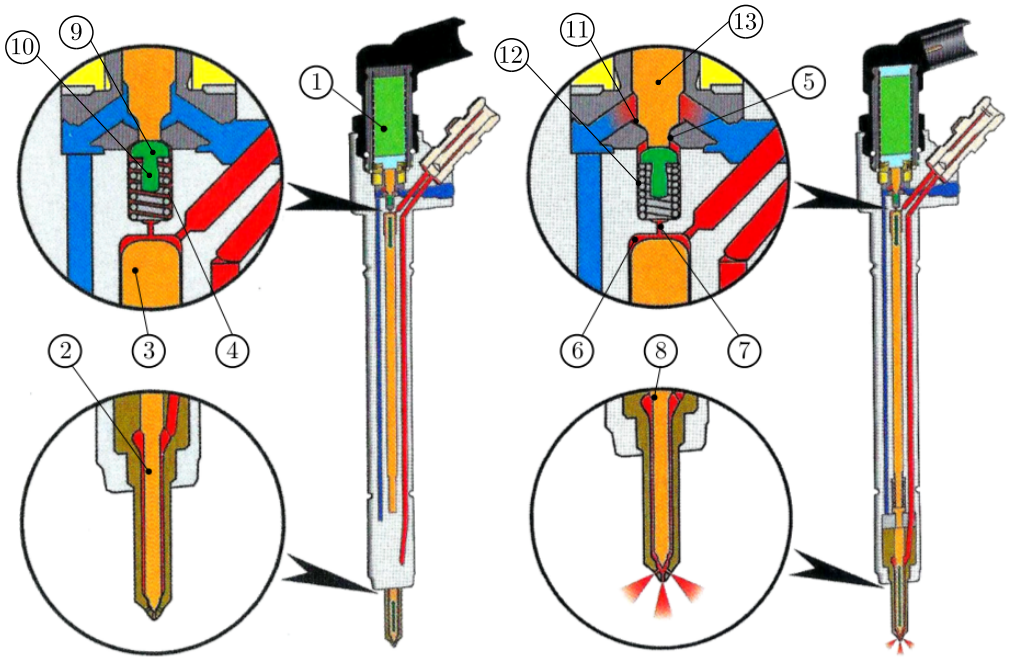

1: piezo actuator
2: nozzle needle
3: control piston
4: return spring
5: sealing seat
6: control chamber
7: discharge throttle
8: high-pressure chamber
9: valve mushroom
10: pilot valve
11: piston chamber
12: valve chamber
13: valve piston

Figure 1.1: Operating principle of a piezo common rail injector. Modified from Bartsch [6]. Red: High-pressure zone, Blue: Low-pressure zone.

1.3 State-of-the-Art

The following section provides a literature survey on experimental and numerical cavitation research relevant for Diesel injection systems applications. First of all, early experimental investigations of internal nozzle flows under cavitating and non-cavitating conditions are briefly summarized. Next, the focus is put on the studies of cavitating flows in scaled transparent replicas, which provide valuable information about cavitation structures forming in Diesel injector systems, such as string and vortex cavitation. Beside that, more recent exper-

imental findings in real-scale nozzles, together with novel X-ray measurement techniques are presented. Numerical research section summarizes the most significant achievements in cavitating flow modeling relevant for the present work. These have emerged rapidly during the last twenty years, as the computational resources became more available.

1.3.1 Experimental Research

Many experimental studies have been conducted in order to gain better understanding of cavitating flows in nozzles and throttles. Due to the high spatial and temporal resolution required, quantitative experimental investigations for Diesel injector applications are challenging – typical diameters of injector nozzles and throttles are 0.2 mm with very short injection times taking usually between 1 ms to 2 ms. High pressures and complex geometrical shapes are further limiting factors for the in-situ measurements. Hence, investigations are usually conducted using simplified and enlarged nozzle configurations under idealized flow conditions.

Early experimental investigations [17, 80, 71] focused on the study of cavitating and non-cavitating flows through nozzles and orifices with focus on discharge characteristics at different flow conditions. Fundamental research of Nurick [80] and Hall [52] provided valuable insights into the cavitation phenomena in sharp-edged nozzles. Nurick [80] also proposed a simple one-dimensional flow model that relates the discharge coefficient C_d to the cavitation number σ and supported it by experimental verification.

Assessing internal nozzle flow was for a long time possible only by applying planar nozzles [59, 73] and enlarged transparent models [26, 47]. Arcoumanis et al. [4] recognized that despite the analogy between cavitation structures in large-scaled replicas and real-sized nozzles – when dynamic similarity based on Reynolds and cavitation number is taken into account – evident differences in the cavity formation exist. Moreover, fluid properties at realistic injection pressures, which are by order of magnitude larger, change significantly. Measurements of Diesel-like fluid properties by Bazile et al. [11] showed an increase of the fluid viscosity up to 10 times due to the pressurization when compared to atmospheric conditions, accompanied by density changes of approximately 10%. Giannadakis et al. [50] demonstrated that such variations of fluid properties can affect cavitation and associated nozzle discharge. Different

authors have shown that cavitation may damage nozzle walls if those are subjected to high loads of collapsing vapor structures [48, 46, 58]. Gavaises et al. [48] linked erosion patterns to the transient cavitation structures in a scaled-up model. It is, however, not evident that erosion damage done to large-scale models at reduced pressure levels will relate to the same cavitation structures forming in real-size nozzles. Therefore, substantial effort has been put in manufacturing real-size transparent injectors which offer free optical access to the internal nozzle flow. Laser light sheet and shadowgraph techniques were applied by Badock et al. [5] for a real-size Diesel nozzle. However, authors were not able to measure the thickness of the cavity in the nozzle due to the existent light scattering. Blessing et al. [20] were among the first to apply the shadograph technique to a real-scale nozzle at injection pressure of 1200 bar. Reid et al. [92] used transparent nozzle at injection pressures up to 2000 bar for study of cavitation characteristics, but utilized simplified injector geometry instead. Nevertheless, acrylic and polycarbonate transparent nozzles are usually limited to lower operating pressures and may suffer from leakage effects associated with high pressures. Mitroglou et al. [77] verified flow similarity between large-scale and real-size nozzles and confirmed a positive effect of cavitation on the spray quality. Taking into the account the very small geometric dimensions, placing probes into the flow field is not possible at these scales, as the flow field will be altered substantially. Furthermore, surface roughness from plastic nozzles differs from that of their metal counterparts, which seems to play a role as well [34]. Whereas visible light measurements provide valuable information about transient flow behavior and topology, they lack in providing quantitative flow data. A major drawback of these methods lies in the scattering that is present at liquid-vapor interfaces as well, thus reducing light transmission.

Recent advances in X-ray measuring techniques have enabled a significant scientific breakthrough in obtaining quantitative data from three-dimensional cavitating flow fields [9, 32, 78]. Although used for spray measurements initially [61, 62, 89], these techniques are gaining in popularity. The main advantage of X-ray techniques is a reduced scattering between liquid-vapor interface, which makes them more suitable for the diagnostics of cavitating flows. Further benefits are the possibility to carry out measurements in non-transparent metal nozzles at the micron spatial resolution, which is essential for flow assessment in micro orifices. Duke et al. [34] performed measurements of submerged cavitating flow in a real-size beryllium

nozzle by means of X-ray radiography and extracted void fraction distribution along the nozzle. However, toxic properties of beryllium limited maximal allowable operating pressures of the test rig. A three-dimensional reconstruction of cavitating structures inside a large-scale model was provided by Mitroglou et al. [78], who utilized X-ray micro computed tomography. A new development of the X-ray fluorescence technique by Duke et al. [32] enabled for the first time simultaneous measurement of non-condensable gas and cavitation in a real-size nozzle. However, to the author's knowledge, there is no quantitative experimental data available for realistic injection pressures exceeding 2000 bar and throttle diameters on the order of several hundred microns operating in a submerged environment.

Several authors addressed the importance of non-condensable gas effects on the flow in hydraulic machinery [53, 60, 32]. Non-condensable gas may affect the performance of hydraulic systems by increasing the compressibility of the medium and consequently altering other properties, such as heat conduction, speed of sound and viscosity [101]. The experimental investigation of Iben et al. [60] demonstrated that cavitation enhances air release. Freudigmann et al. [44] linked an air-release to cavitation in the one-dimensional model and demonstrated good agreement with the experimental data. The coupling between cavitation and air release was numerically investigated by Mihatsch [75], who extended the single-fluid model to take into account diffusive release and absorption of gas, as well as degassing promoted by cavitation. Battistoni et al. [8] included a fixed amount of non-condensable gas into the mixture model and compared the results with X-ray radiography measurements of Duke et al. [33] for two different gas contents.

1.3.2 Numerical Research

Whereas experimental research of cavitating nozzle flows can be traced back to 1960s [17], first attempts of numerical simulation of cavitating flows for Diesel-relevant applications can be found in the 1990s, with the development of computational fluid dynamics (CFD). CFD gained rapidly in attractiveness for IC engine applications due to the aforementioned difficulties and challenges associated with the experimental studies, thus making it an ideal complement to experimental investigations. Delannoy [30] utilized a single-fluid mixture model for the study of cavitating flow in a Venturi nozzle. Several early studies examined the influence of the nozzle

entrance shape on the cavitation intensity in the nozzle [100, 96, 109]. Schmidt et al. [97], investigated cavitating flow in the injection nozzle and employed a single-fluid, compressible flow solver. The authors were able to assess discharge characteristics of different nozzle configurations. Yuan et al. [109] developed a combination of an incompressible volume-of-fluid (VOF) method and bubble growth and collapse model to study the effect of the nozzle inlet rounding on cavitation formation in the nozzle. The same method [see 110] was extended to take into account the free gas present at the nozzle exit, which enabled to assess numerically the hydraulic flip phenomenon. However, authors were not able to capture unsteady cavitation effects, assuming that the inclusion of the $k-\omega$ turbulence model overestimated viscous effects in cavitating regions. A similar approach was followed by Martynov et al. [72] in their study of cavitating nozzle flow. Several investigations adopted incompressible Reynlods-averaged Navier-Stokes (RANS) framework for predicting cavitating flow in single- and multi-hole injector nozzles [47, 3, 49]. Giannadakis et al. [49] developed a bubbly flow model in which the liquid phase was treated as a continuum in the Eulerian frame of reference, while dispersed vapor phase was tracked in the Lagrangian frame of reference. In order to overcome computational difficulties associated with tracking large number of vapor bubbles, authors utilized the stochastic approach, based on the agglomeration of bubbles into clusters which are being tracked instead. The same approach was used in the recent study of Strotos et al. [105], who accounted for the thermal effects in a realistic high pressure nozzle.

Schmidt et al. [98] developed a fully compressible flow solver utilizing a homogeneous mixture cavitation model. CFD analysis of single- and multi-hole nozzle using the same modeling approach was carried out in [102, 13, 14, 15]. It has been shown that compressible treatment of liquid and liquid-vapor mixture is essential for capturing collapse-induced shock formation, which is a driving mechanism for cavitation erosion [99]. Mihatsch et al. [76] utilized the same methodology for the radial-gap flow setup and related numerically obtained positions of vapor clouds collapse centers and intensity to the experimentally obtained material erosion rate. The main advantage of the proposed model was its intrinsic capability to assess cavitation erosion, without derivation of additional erosion models. Egerer et al. [39] investigated cavitating flow in a planar micro-throttle by means of a compressible large-eddy simulation (LES) and successfully reproduced experimental data. In the recent work of Örley et al. [83]

and Koukouvinis et al. [65], the authors focused on the erosion assessment of a multi-hole injector by including the dynamic needle movement in the compressible LES approach. Örley et al. [84] demonstrated the influence of the collapse-induced pressure disturbances near the nozzle exit on the promotion of primary brake-up. Further applications of LES and the homogeneous mixture model can be found in [95, 35].

1.4 Objective of the Present Work

Based on the literature review given in the preceding section, it becomes evident that cavitating throttle flows are a very attractive field of research, particularly for the automotive industry applications, where strict emission policies apply. The following work aims to provide a deeper insight into the flow dynamics of cavitating micro devices, employing a fully compressible computational framework. Thus, the major goals are to

- develop an equation of state for Diesel calibration fuel without and with the presence of non-condensable gas, based on the data available in the open literature,
- gain knowledge about the flow in the realistic valve chamber and derive a generic, but still application-relevant valve chamber model capable of representing principal flow features at an affordable computational effort, and
- numerically assess the cavitating throttle flow by means of high-fidelity CFD simulation with the utilization of developed generic designs and physical models.

This thesis is organized as follows. Following the introductory chapter, Chapter 2 briefly summarizes the fundamentals of cavitating flows and introduces the definitions used in the thesis. Chapter 3 outlines the numerical methods and the physical model utilized for investigations. In Chapter 4, we present the numerical results of the cavitating flow in the realistic valve chamber, followed by the description of the generic valve chamber. Chapters 5 and 6 discuss in detail the influence of the geometry, i.e. the throttle design and the step-hole diameter, on the cavity dynamics in the valve chamber. The flow dynamics in these investigations is assessed by means of inviscid simulations. In Chapter 7, we separately examine the influence

of the non-condensable gas and turbulence on the throttle flow. The work is concluded in Chapter 8, where the main findings and gained knowledge are summarized.

2 Fundamentals of Cavitation

This chapter briefly introduces fundamentals of cavitation and cavitation erosion. Cavitation can be defined as formation of vapor cavities (voids) in the liquid. *Hydrodynamic cavitation* appears if the flowing liquid is subjected to local acceleration, whereas *acoustic cavitation* arises in stagnant liquids when an oscillating pressure field is applied. In both cases, cavities arise if the static pressure drops below a certain threshold. Some examples of hydrodynamic cavitation include flows through Venturi and injection nozzles or around hydrofoils [47, 63, 42]. In medical applications, shock waves generated by extracorporeal shock wave lithotripters induce acoustic cavitation for the disintegration of kidney stones [28].

A phase diagram given in Fig. 2.1 depicts the difference between cavitation and *boiling*. The curve connecting the triple point to the critical point separates the liquid from the vapor phase and depends on temperature only. Boiling is a phase change from the liquid to the vapor state at a constant pressure and is accompanied by a temperature increase. Cavitation, in contrast, is a process in which the static pressure drops below the saturation (vapor) pressure along the approximately isothermal path. In reality, this process is non-isothermal and a minor temperature decrease in the liquid is observed (thermal delay) as the liquid supplies the latent heat of vaporization to complete the phase change.

Beside the described cavitation process, the liquid can undergo phase change at the pressures far below the vapor pressure. It is to be assumed that the liquid is purified, i.e. it doesn't contain gas bubbles or other impurities in the form of solid particles. In such meta-stable

states, the liquid sustains negative pressures (tensions) on the order of several hundreds of bars before it breaks down [22]. However, there is usually some amount and form of impurity present in the fluids utilized for industrial applications, which are, therefore, expected to rupture as soon as the static pressure reaches the vapor pressure, $p = p_{vap}$. Such "weak" spots in the liquid are known as cavitation nuclei.

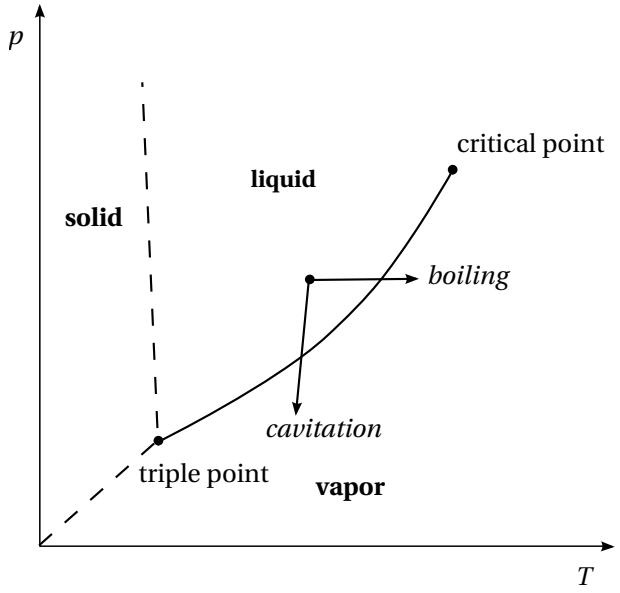

Figure 2.1: Example of a phase diagram for one-component fluid.

Cavitating flows are commonly characterized by the cavitation number σ [43]:

$$\sigma = \frac{p_{ref} - p_{vap}(T)}{\frac{1}{2}\rho_{ref} u_{ref}^2}, \tag{2.1}$$

where p_{ref} is the reference pressure at some fixed point in the flow and ρ_{ref} and u_{ref} are reference density and velocity, respectively. Depending on the field of application, the definition of the cavitation number may vary slightly. For the internal nozzle flow applications, the denominator in Eq. 2.1 is commonly replaced by the pressure difference $p_{in} - p_{out}$ across the nozzle or throttle. For the reference pressure, either p_{in} or p_{out} can be selected. Throughout

this work, we utilize the following definition [80]:

$$\sigma = \frac{p_{in} - p_{vap}(T)}{p_{in} - p_{out}} \,. \tag{2.2}$$

If the cavitation number is smaller than the cavitation number at *inception* σ_i, cavitation nuclei present in the bulk liquid grow explosively and further reduction of the cavitation number leads to *developed cavitaiton*.

This work investigates hydrodynamic cavitation in Diesel injector components in which different cavitation types may occur simultaneously. Brennen [21] distinguishes between the following types of cavitation:

- *traveling bubble cavitation*: Cavitation nuclei present in the free stream in the form of micro-size bubbles expand when advected to the low pressure regions, such as suction side of a hydrofoil or a turbine blade and collapse further downstream where pressure recovers. The growth of cavitation bubbles can either be initiated by the evaporation on the phase boundary or by the expansion of the gas present in the bubble. Holl [57] identifies the latter as *pseudo cavitation*, as bubbles may grow at pressures larger than the vapor pressure. Figure 2.2a depicts bubble cavitation on the suction side of a hydrofoil.

- *sheet or attached cavitation*: A cavity attaches to the leading edges of foil sections or turbine blades and, depending on the angle of attack and the cavitation number, it behaves either steady or unsteady. *Partial cavities*, which are the intermediate stage of cavitation development, do not oscillate at small angles of attack and cavitation numbers. However, for large values of the angle of attack and the cavitation number, cavities become unsteady and shed vapor clouds randomly or periodically. Figure 2.2b shows the sheet cavity attached to the leading edge of the hydrofoil and the shed vapor cloud in the vicinity of the trailing edge. For low cavitation numbers, the cavity doesn't close on the foil section, but further downstream instead. In this case, the whole suction side of the hydrofoil is immersed into the cavity, as shown in Fig. 2.2c. This form of

cavitation is also known as *supercavitation*.

- *cloud cavitation*: Cavity clouds usually form when an oscillating cavity sheet detaches from the foil surface. An example of the detached vapor cloud is shown in Fig. 2.2b.

- *vortex cavitation*: Vortex cavitation forms in the vortex cores if the pressure drops below the vapor pressure. One typical example are tip vortices on ship propellers, as depicted in Fig. 2.2d.

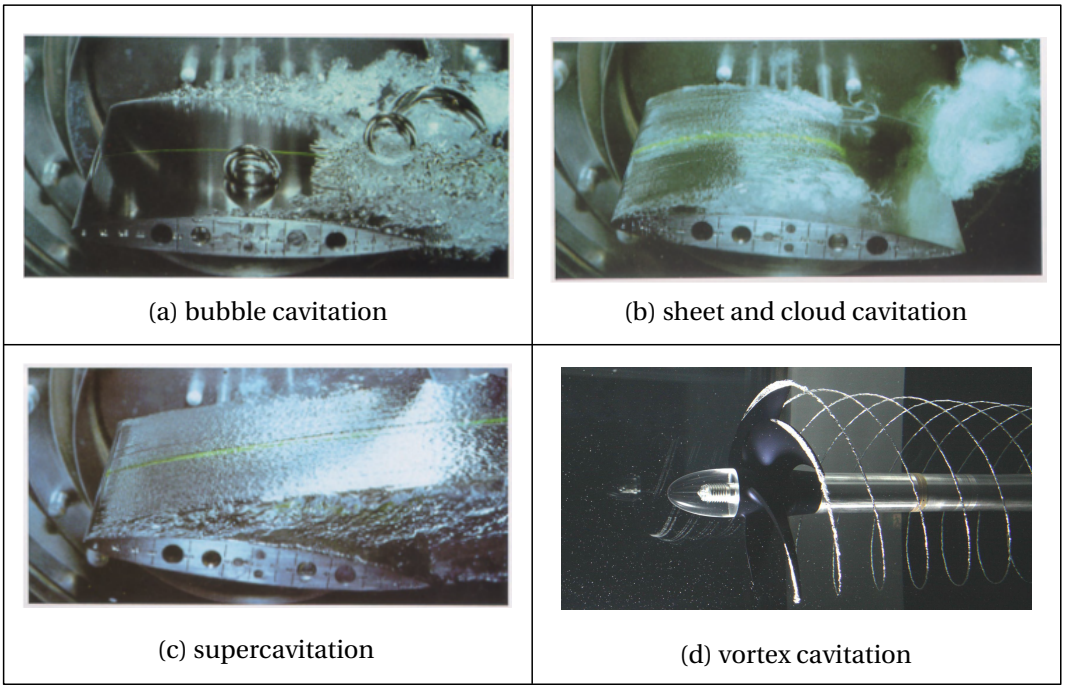

(a) bubble cavitation

(b) sheet and cloud cavitation

(c) supercavitation

(d) vortex cavitation

Figure 2.2: (a)-(c) Different types of cavitation observed at NACA 16012 hydrofoil by Franc and Michel [42]. (b) Tip vortex cavitation at the model ship propeller [2].

Vapor cavities produced in low pressure zones collapse when advected in regions where pressure recovers. The surrounding liquid accelerates towards the center of the cavity causing a compression of the cavity as vapor condenses at the interface. When the cavity bubble completely collapses, a shock front is developed, which propagates through the surrounding liquid. A spherical cavity collapse has been subject of numerous experimental studies [91, 106, 86]. Vogel et al. [106] measured peak pressures up to 6 GPa in the cavity at the final collapse stages. A non-spherical collapse occurs if the cavitiy collapses near a solid boundary. The main feature of the non-spherical cavity collapse is the additional development of the

micro-jet. In such a configuration, the upper side of the cavity accelerates inward more rapidly than the lower side, and a micro-jet directed toward the solid wall ruptures the cavity and impinges on the boundary, as shown in Fig. 2.3. Here, both the impact of the shock wave and the “water hammer” effect of the liquid jet may cause stresses on the order of several GPa on material surfaces [21]. Cavitation erosion usually develops if the surfaces of technical devices are exposed to the repetitive and coherent collapse of clouds of cavitation bubbles. Damaged areas are often localized, as depicted in Fig. 2.4.

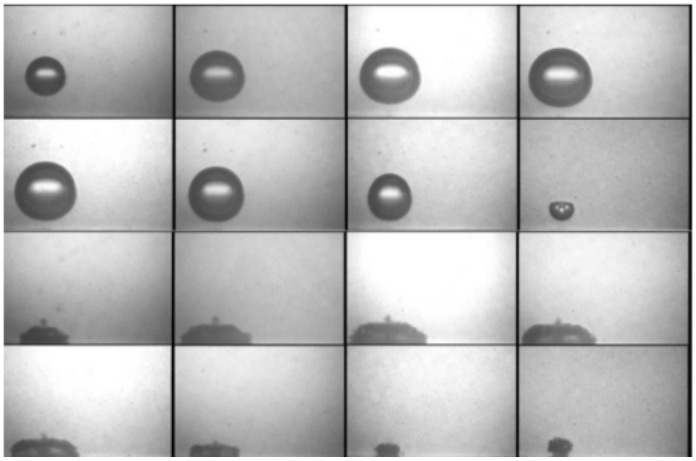

Figure 2.3: Experimental sequence of growth and non-spherical cavity collapse in the vicinity of a solid wall [107].

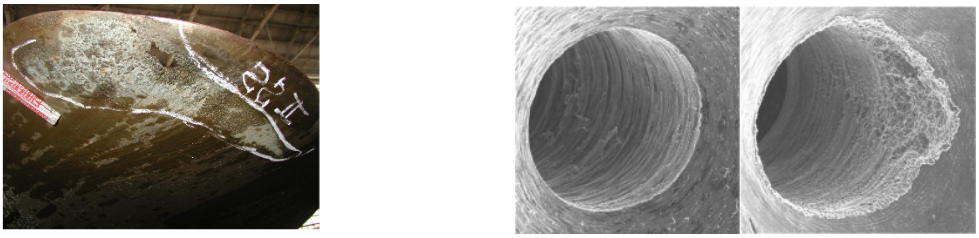

(a) (b)

Figure 2.4: (a) Cavitation damage on a propeller blade [74], (b) damage at the discharge throttle inlet of a fuel injector [108].

3 Numerical Method and Physical Model

This chapter outlines the numerical methods and physical model used in investigations. The first section provides an overview of the numerical method and the underlying numerical scheme utilized for the inviscid flow computations (*baseline scheme*), together with the discretization scheme employed for the large-eddy simulation of cavitating flow (*modified baseline scheme*). The second section describes the cavitation and the thermodynamic model for ISO 4113 calibration fuel without and with the presence of non-condensable gas.

3.1 Numerical Method

3.1.1 Governing Equations

Compressible Navier-Stokes equations without body forces can be written in compact vector form as

$$\frac{\partial \mathbf{U}}{\partial t} + \frac{\partial \mathbf{F}(\mathbf{U})}{\partial x_i} = 0, \tag{3.1}$$

where $\mathbf{U}$ is the vector of conserved quantities and the column vector $\mathbf{F}(\mathbf{U})$ denotes the physical flux. The first row of the differential vector equation (Eq. 3.1) resembles the continuity equation. Correspondingly, the second, third and fourth rows are momentum equations, while the fifth row is the energy equation. Further, we can split the physical flux vector into

the inviscid $\mathbf{F}^{\mathrm{I}}(\mathbf{U})$ and viscous part $\mathbf{F}^{\mathrm{V}}(\mathbf{U})$

$$\mathbf{F}(\mathbf{U}) = \mathbf{F}^{\mathrm{I}}(\mathbf{U}) + \mathbf{F}^{\mathrm{V}}(\mathbf{U}) \,, \tag{3.2}$$

respectively. The vector of conserved quantities and the physical flux vector $F_i(\mathbf{U})$ for the spatial direction i are defined as follows

$$\mathbf{U} = \begin{pmatrix} \rho \\ \rho u_1 \\ \rho u_2 \\ \rho u_3 \\ \rho E \end{pmatrix} \tag{3.3}$$

$$F_i^{\mathrm{I}}(\mathbf{U}) = u_i \cdot \begin{pmatrix} \rho \\ \rho u_1 \\ \rho u_2 \\ \rho u_3 \\ \rho H \end{pmatrix} + p \cdot \begin{pmatrix} 0 \\ \delta_{1i} \\ \delta_{2i} \\ \delta_{3i} \\ 0 \end{pmatrix} \qquad F_i^{\mathrm{V}}(\mathbf{U}) = - \begin{pmatrix} 0 \\ \tau_{i1} \\ \tau_{i2} \\ \tau_{i3} \\ u_j \tau_{ij} + q_i \end{pmatrix} , \tag{3.4}$$

with $\mathbf{F} = \sum_{i=1}^{3} F_i(\mathbf{U})$. Further, $E = e + \frac{1}{2}\left(u_1^2 + u_2^2 + u_3^2\right)$ is the specific total energy, $H = E + p/\rho$ is the specific total enthalpy and δ_{ji} denotes Kronecker delta symbol. The viscous stress tensor for a Newtonian fluid is defined as

$$\tau_{ij} = \mu\left(\frac{\partial u_i}{\partial x_j} + \frac{\partial u_j}{\partial x_i}\right) - \mu\frac{2}{3}\frac{\partial u_k}{\partial x_k}\delta_{ji} \,. \tag{3.5}$$

The heat flux q_i can be modeled proportionally to the local temperature gradient with Fourier's law of heat conduction

$$q_i = -k\frac{\partial T}{\partial x_i} \,, \tag{3.6}$$

where k denotes the thermal conductivity coefficient and T the static temperature.

3.1.2 Finite Volume Method

We discretize Eq. 3.1 by the finite volume method. The integral form of the conservation law applied to each control volume V_J

$$\frac{\partial}{\partial t}\int_{V_J}\mathbf{U}dV = -\oint_{S_J}\mathbf{F}d\mathbf{S} \tag{3.7}$$

states that the time change of a conserved quantity inside the computational cell depends only on the fluxes through the volume surfaces. The cell-averaged conservative variables are defined as

$$\mathbf{U}_J = \frac{1}{V_J}\int_{V_J}\mathbf{U}dV\,. \tag{3.8}$$

Our implementation of the numerical solver operates on the four-cell stencil, as depicted in Fig. 3.1. A modified Riemann solver is utilized for the flux computation at the cell interfaces, which is discussed in the next subsection. Representation of complex geometries is supported by the body-fitted, multiblock grid structure with the matching grid lines at block interfaces.

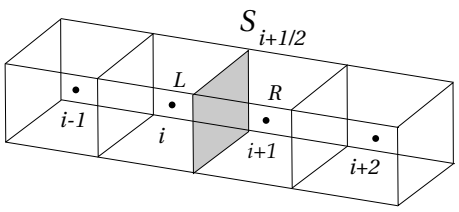

Figure 3.1: Sketch of a four-cell stencil utilized in the numerical method. Numerical flux is computed through the gray area.

Baseline Scheme

As the major focus of this thesis is put on inertia-driven instabilities, we use a physically inviscid formulation of the governing equations, thus omitting the contribution of the viscous fluxes, $\mathbf{F}^{\mathrm{V}}(\mathbf{U}) = 0$. Consequently, neither implicit nor explicit turbulence models are applied. We utilize a low-Mach-number consistent flux function for the approximation of the physical fluxes [98]. In the following, reconstructed cell-face values are marked with $\widetilde{\circ}$. The inviscid

part of the numerical flux function in x_1 direction at the cell face $S_{i+1/2}$ is given by

$$\mathbf{F}^{\text{num}}_{i+1/2} = \widetilde{u}^* \cdot \begin{pmatrix} \widetilde{\rho} \\ \widetilde{\rho}\widetilde{u}_1 \\ \widetilde{\rho}\widetilde{u}_2 \\ \widetilde{\rho}\widetilde{u}_3 \\ \widetilde{\rho}\widetilde{H} \end{pmatrix}^L + \widetilde{p}^* \cdot \begin{pmatrix} 0 \\ 1 \\ 0 \\ 0 \\ 0 \end{pmatrix}, \qquad \text{for } \widetilde{u}^* \geq 0 \tag{3.9}$$

where $\widetilde{u}^*$ is the velocity at the shared cell surface between the left (L) and right (R) neighbor control volume. For the negative mass flow rate ($\widetilde{u}^* < 0$), superscript L is replaced with R, i.e. the numerical scheme is upwind-biased. For the x_1 direction we compute transport velocity $\widetilde{u}^*$ as

$$\widetilde{u}^* = \frac{I^L \widetilde{u_1}^L + I^R \widetilde{u_1}^R + p^L - p^R}{I^L + I^R} \tag{3.10}$$

with acoustic impedances defined as

$$I^L = \frac{1}{4}\left(3\widetilde{\rho}^L + \widetilde{\rho}^R\right) \qquad I^R = \frac{1}{4}\left(\widetilde{\rho}^L + 3\widetilde{\rho}^R\right) \tag{3.11}$$

and the maximum speed of sound obtained from the neighboring cells, $c_{max} = \max\left(c_L, c_R\right)$. The interface pressure is reconstructed by the second-order central approximation, which ensures a low-Mach-number consistency [98]

$$\widetilde{p}^* = \frac{p^L + p^R}{2}\,. \tag{3.12}$$

Cell-face velocities are reconstructed using the total variation diminishing (TVD) limiter proposed by Koren [64], which is third-order accurate for smooth fields. First-order reconstruction of density and internal energy is employed. During the time-marching solution procedure, the vector of conserved quantities $\mathbf{U}$ is advanced by employing an explicit 4-stage, low-storage Runge-Kutta method. We use a constant Courant-Friedrichs-Levy (CFL) number of 1.4.

Modified Baseline Scheme

Egerer et al. [40] designed an efficient discretization scheme which operates on the four-cell stencil and is applicable for LES of compressible cavitating flows. The modified scheme localizes numerical dissipation to the regions in the flow field where discontinuities are detected. The inviscid flux function is extended with the regularization term **R** that accounts for the unresolved subgrid-scale dynamics, as given here for the x_1 direction at the cell face $S_{i+1/2}$

$$\mathbf{F}^{\mathrm{num}}_{i+1/2} = \widetilde{u}^* \cdot \begin{pmatrix} \widetilde{\rho} \\ \widetilde{\rho}\widetilde{u}_1 \\ \widetilde{\rho}\widetilde{u}_2 \\ \widetilde{\rho}\widetilde{u}_3 \\ \widetilde{\rho e} + \frac{1}{2}\widetilde{\rho} u_i^2 + \widetilde{p} \end{pmatrix} + \widetilde{p}^* \cdot \begin{pmatrix} 0 \\ 1 \\ 0 \\ 0 \\ 0 \end{pmatrix} - \left[1 - f(\beta)\right] \begin{pmatrix} R^{\rho} \\ R^{u_1} \\ R^{u_2} \\ R^{u_3} \\ R^{E} \end{pmatrix}, \tag{3.13}$$

where $f(\beta)$ is the sensor functional. The structure of the regularization term **R** is adopted from the Adaptive Local Deconvolution Method (ALDM) [55, 56]. Viscous flux contribution $\mathbf{F}^{\mathrm{V}}(\mathbf{U})$ is discretized by the second-order scheme. The reconstruction of conserved quantities switches from the central to an upwind-biased procedure based on the value of the sensor functional. In smooth regions, pressure and velocities are reconstructed by the linear fourth-order scheme, whereas density and internal energy are computed by the arithmetic mean. A detailed discussion of reconstruction procedures is provided by Egerer et al. [40]. Transport velocity $\widetilde{u}^*$ is redefined as

$$\widetilde{u}^* = \left[1 - f(\beta)\right]\left(\widetilde{u}^C - \frac{\widetilde{\Delta^3 p}^*}{I^L + I^R}\right) + f(\beta)\left(\frac{I^L \widetilde{u}^L + I^R \widetilde{u}^R + \widetilde{p}^L - \widetilde{p}^R}{I^L + I^R}\right) \tag{3.14}$$

where $\widetilde{u}^C$ is the interface velocity reconstructed by the fourth-order central scheme and $\widetilde{\Delta^3 p^*}$ denotes an approximation of the third pressure derivative [56]. We employ Ducros' vorticity-dilatation sensor [31] and vapor volume sensor [40] that activate the sensor functional if a

certain threshold value is exceeded

$$f(\beta) = \begin{cases} 1, & \text{if } \beta_{Durcros} > \beta^{th}_{Durcros} \,||\, \beta_{vapor} > \beta^{th}_{vapor} \\ 0, & \text{otherwise.} \end{cases} \tag{3.15}$$

For $f(\beta) = 1$, the baseline scheme recovers. We adopt $\beta^{th}_{Durcros} = 0.95$ and $\beta^{th}_{vapor} = 0.25$ for the flow sensor threshold values.

3.2 Single-Fluid Cavitation Model for ISO 4113 Fuel

In this investigation, we employ the calibration ISO 4113 fuel, based on the data available from the literature [27]. Two-phase modeling utilizes a single-fluid cavitation model that assumes the equilibrium phase change and homogeneous mixture. As shown in previous investigations [83, 98, 99, 76, 39], surface tension and slip velocity between phases can be neglected and single-fluid models are thus an appropriate choice. The equilibrium phase change allows for an instantaneous establishment of two-phase cavitating regions and considers thermodynamic balance between phases. Coexisting phases are thus described by saturation conditions, and share a common temperature $T = T_l = T_v$ and pressure $p = p_l = p_v$. Subscripts l and v represent the liquid and the vapor phase, respectively. These assumptions allow us to express the mixture density as a convex combination of the liquid and vapor saturation densities, $\rho_{l,sat}$ and $\rho_{v,sat}$, respectively, as

$$\rho = \alpha \rho_{v,sat}(T) + (1-\alpha)\rho_{l,sat}(T)\,, \tag{3.16}$$

where α denotes the vapor volume fraction. Pressure and temperature can be either computed from the mass-averaged internal energy, or, as chosen in this investigation, by assuming a barotropic dependency of pressure and density, $p = p(\rho)$. Barotropic relations improve the efficiency of the computations, as the energy balance is obsolete. However, further model assumptions to specify the thermodynamic path of the process are required. Typical paths are either isothermal or isentropic, resulting in constant temperature or in constant entropy. In the following, we derive approximate barotropic relations for the pure liquid as well as for the coexisting liquid-vapor equilibria.

3.2.1 Liquid

In the pure liquid, cell-averaged pressure is described by the barotropic equation of state which can be approximated by truncated Taylor series as

$$p = p_{sat} + A(\rho - \rho_{l,sat}) + B(\rho - \rho_{l,sat})^2, \qquad \rho \geq \rho_{l,sat}\,. \tag{3.17}$$

Parameters A and B have to be optimized to match experimental references. As an example, two isothermal paths fitted for temperatures $T = 323.15$ K and $T = 353.15$ K are plotted in Fig. 3.2. The resulting data fits show an excellent agreement with experimental values reported in literature [27]. However, we fit these parameters to represent a typical thermodynamic path as occurring in the system under investigation and consider an inlet temperature of 353.15 K. We investigate a high pressure reservoir discharging into a low pressure chamber. The bulk of the liquid undergoes adiabatic expansion. Additionally, viscous heating increases entropy and temperature. However, its amount will significantly depend on whether the liquid is in direct contact with the nozzle wall, or if it is separated by a vapor film. For this investigation, it is less relevant to describe both processes in detail, as our focus is on the dynamics of the flow within the discharge throttle. Although a more elaborate full thermodynamic model would be preferable, we believe that the efficient barotropic equation of state is sufficient to investigate the fundamental differences of flow features for the selected designs.

Property	A [m^2/s^2 × 10^6]	B [m^4/(kg s^2) × 10^4]	p_{sat} [Pa]	$\rho_{l,sat}$ [kg/m^3]
Value	1.292	1.8955	56.2	798.722

Table 3.1: Parameters for the liquid equation of state of the ISO 4113 test fuel.

In order to model the thermodynamic behavior as accurately as possible, we assume a temperature decrease of 15 K/1000 bar. The assumed value compares well with the adiabatic cooling/heating rates of paraffin components (n-Decane, n-Dodecane) of ISO 4113 fuel, obtained from the REFPROP database [69]. The saturation values at T= 323.15 K are $p_{sat} = 56.2$ Pa and $\rho_{l,sat} = 798.722$ kg/m^3. The resulting thermodynamic path is plotted in blue in Fig. 3.2. The parameters are summarized in Table 3.1. We compute the speed of sound in the liquid

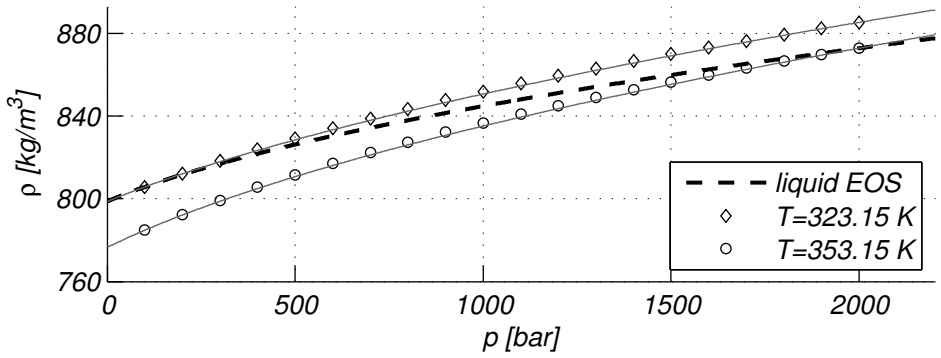

Figure 3.2: Barotropic relation between pressure and density for the test fluid ISO 4113. The dashed line depicts the equation of state for the variable temperature, whereas solid lines correspond to the equation of state for fixed temperatures. Symbols denote experimental measurements by Chorążewski et al. [27].

phase as derivative of the barotropic law

$$c_{liq} = \sqrt{A + 2 \cdot B(\rho - \rho_{l,sat})}\,. \tag{3.18}$$

Viscous effects are taken into account by empirical relation as given by Bazile et al. [11]

$$\mu(p, T^*) = A \cdot \exp\left(\frac{B}{T^* - C}\right) \cdot \exp\left[D \cdot \ln\left(\frac{p + E(T^*)}{p_{atm} + E(T^*)}\right)\right], \tag{3.19}$$

with $E(T^*) = E_0 + E_1 T^* + E_2 T^{*^2}$, and temperature T^* estimated by the adiabatic cooling/heating rate $dT/dp = 15 \times 10^{-8}$ [K/Pa] as

$$T^* = T_{ref} + \frac{dT}{dp} \cdot (p - p_{ref})\,. \tag{3.20}$$

The reference pressure and temperature are $p_{ref} = 2000$ bar and $T_{ref} = 353.15$ K, respectively. Table 3.2 summarizes parameters for Eq. 3.19.

A [$\times 10^{-2}$]	B [$\times 10^{-3}$]	C	D	E_0 [$\times 10^{3}$]	E_1	E_2 [$\times 10^{-3}$]
1.57172	1.31499	43.4857	8.80025	−1.61765	10.2744	−9.11075

Table 3.2: Parameters for Eq. 3.19

3.2.2 Liquid-vapor mixture

Modeling the thermodynamic behavior of liquid-vapor coexistence represents a challenge. Experimental data are mostly missing or not available in the open literature. Previous investigations [84, 83] indicated that a linear dependency between pressure and density is suitable. In this case we apply

$$p = p_{sat} + c_m^2(\rho - \rho_{l,sat}), \qquad \rho < \rho_{l,sat}. \tag{3.21}$$

However, we ensure that pressure and density are positive quantities by enforcing that $p \to 0$ if and only if $\rho \to 0$. Therefore, we assume that the equilibrium speed of sound of the mixture c_m is expressed by

$$c_m = \sqrt{\frac{p_{sat}}{\rho_{l,sat}}} = \text{const.} \tag{3.22}$$

For viscous flow calculations, we adopt the mixture viscosity model proposed by Beattie and Whalley [12]

$$\mu = \big(1-\alpha\big)\big(1+\frac{5}{2}\alpha\big)\mu_{liq} + \alpha\mu_{vap}\,, \tag{3.23}$$

where the viscosity of the vapor phase is $\mu_{vap} = 1 \times 10^{-7}$ Pas.

3.3 Extension of the Single-Fluid Cavitation Model with Non-Condensable Gas Component

Following the approach introduced by Mihatsch [75], we provide here building blocks from which the equation of state for the ISO 4113 fuel with a non-condensable gas component is extended. Components are identified with capital letters l-liquid, lv-liquid-vapor mixture and g-non-condensable gas, respectively. In general, a component is subscribed with i. Coexisting phases are in mechanical and thermodynamic equilibrium, sharing one temperature $T = T_l = T_{lv} = T_g$ and pressure $p = p_l = p_{lv} = p_g$ field. The effect of surface tension and of the slip between coexisting phases are neglected, $u = u_l = u_{lv} = u_g$. The gas phase is assumed

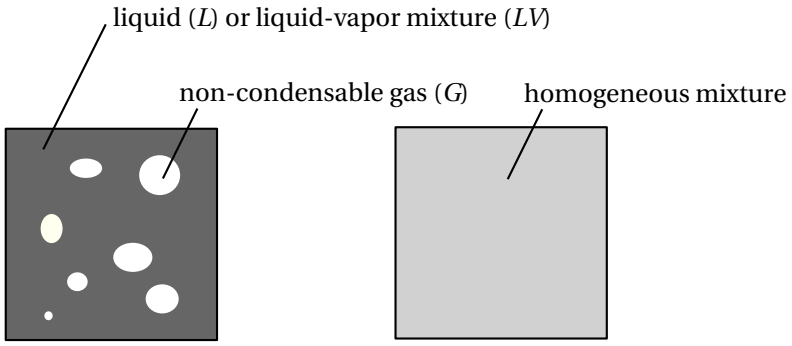

Figure 3.3: Homogeneous mixture representation in the computational cell.

to behave ideally and isothermally. Further, gas absorption and the release of gas from the solution are not included into the model. Thus, we prescribe a fixed amount of non-condensable gas that remains constant during the computation. Figure 3.3 represents a homogeneous mixture of a multicomponent fluid in the computational cell. Volume fraction β_i and mass fraction ε_i of component i are defined as follows

$$\beta_i = \frac{V_i}{V}\,, \tag{3.24}$$

$$\varepsilon_i = \frac{m_i}{m}\,. \tag{3.25}$$

The sum of volume and mass fractions over all components is

$$\sum_i \beta_i = 1 \qquad\qquad \sum_i \varepsilon_i = 1\,.$$

For the non-condensable gas, we apply the ideal gas law

$$p = \rho R T\,. \tag{3.26}$$

In the computational cell, two states are possible: mixture of non-condensable gas with the pure liquid or with the liquid-vapor. Therefore, we express the mixture density ρ as a convex combination of the liquid ρ_l, or the liquid-vapor mixture density ρ_{lv} and the non-condensable gas density ρ_g

$$\rho = \beta_{l/lv}\rho_{l/lv} + \beta_g\rho_g = (1-\beta_g)\rho_{l/lv} + \beta_g\rho_g\,. \tag{3.27}$$

The density of the component i can be related to the mixture density ρ as

$$\rho_i = \frac{m_i}{V_i} = \frac{\varepsilon_i m}{\beta_i . V} = \frac{\varepsilon_i}{\beta_i}\rho \tag{3.28}$$

Substituting the second term from Eq. 3.27 with Eq. 3.28 we get

$$\rho = (1-\beta_g)\rho_{l/lv} + \varepsilon_g \rho \tag{3.29}$$

After applying the ideal gas law (Eq. 3.26) and rearranging Eq. 3.29 we obtain

$$\Big(1-\varepsilon_g\Big)\rho - \left(1-\varepsilon_g RT\frac{\rho}{p}\right)\rho_{l/lv} = 0\,. \tag{3.30}$$

Equation 3.30 is of a general type, as no specific equation of state for the liquid or liquid-vapor mixture has been applied so far. By letting $p = p_{sat}$ and $\rho_{l/lv} = \rho_{l,sat}$ in Eq. 3.30, we can discriminate between states

$$\Big(1-\varepsilon_g\Big)\rho < \left(1-\varepsilon_g RT\frac{\rho}{p_{sat}}\right)\rho_{l,sat}\,. \tag{3.31}$$

If the inequality described by Eq. 3.31 is satisfied at the current time step, cavitation develops in the computational cell. Therefore, we compute the pressure by including the equation of state for the liquid-vapor mixture (Eq. 3.21) in Eq. 3.30 as follows

$$\Big(1-\varepsilon_g\Big)\rho - \left(1-\varepsilon_g RT\frac{\rho}{p}\right)\left(\rho_{l,sat} + \frac{p-p_{sat}}{c_m^2}\right) = 0\,. \tag{3.32}$$

The unknown pressure p is now obtained by solving the quadratic equation.

Otherwise, cavitation doesn't take place, and we compute the corresponding state from Eq. 3.17 which we include in Eq. 3.30

$$\Big(1-\varepsilon_g\Big)\rho - \left(1-\varepsilon_g RT\frac{\rho}{p_{sat} + A(\rho_l-\rho_{l,sat}) + B(\rho_l-\rho_{l,sat})^2}\right)\rho_l = 0\,. \tag{3.33}$$

Here, we first solve for density ρ_l by utilizing the iterative Newton-Raphson method and subsequently obtain the unknown mixture pressure p from Eq. 3.17. For the solution procedure,

the following functions are defined with $\Delta\rho = \rho_l - \rho_{l,sat}$

$$f_1(\rho) = \frac{(1-\varepsilon_g)\rho}{\rho_l} \quad \text{and} \quad g_1(\rho) = \frac{df_1(\rho)}{d\rho} \tag{3.34}$$

$$f_2(\rho) = \left(1 - \varepsilon_g RT \frac{\rho}{p_{sat} + A\Delta\rho + B\Delta\rho^2}\right) \quad \text{and} \quad g_2(\rho) = \frac{df_2(\rho)}{d\rho} \tag{3.35}$$

$$f_1(\rho) - f_2(\rho) = 0 \tag{3.36}$$

The procedure for the iterative pressure search is given in Algorithm 1.

Algorithm 1: Computation of the pressure with Newton-Raphson method

Result: mixture pressure p
/* Set initial values for $\Delta\rho$ and $d\Delta\rho$ */
if $p > p_{sat}$ **then**
  $\Delta\rho \leftarrow ComputeRho(p) - \rho_{l,sat}$;
else
  $\Delta\rho \leftarrow 1$;
end
$d\Delta\rho \leftarrow 1$;
/* Newton-Raphson iteration loop */
/* δ - termination criteria threshold */
while $|\Delta\rho| > \delta$ **do**
  $F \leftarrow f_1(\rho) - f_2(\rho)$;
  $dF \leftarrow g_1(\rho) - g_2(\rho)$;
  $d\Delta\rho \leftarrow -\frac{F}{dF}$;
  $\Delta\rho \leftarrow \Delta\rho + d\Delta\rho$
end
$p \leftarrow ComputeP(\rho)$

4 Flow in the Realistic Valve Chamber and Derivation of a Generic Model

In this chapter we present a simulation of flow in the realistic valve chamber of a common rail injector. Flow is examined for three operating points which differ in the imposed inlet pressure. We investigate general flow topology and assess erosive behavior for each operating point. The geometric complexity of the realistic valve chamber and high computational costs give the main motivation for the development of a generic model, which could enable more fundamental investigation of the submerged high-speed cavitating flows. The generic model of the valve chamber and its geometric properties are presented in the section at the end of this chapter.

4.1 Realistic Valve Chamber

4.1.1 Geometrical Model

The valve chamber of the common rail injector, together with its parts is one of the key components responsible for fast and time-accurate fuel delivery. Figure 4.1 illustrates the CAD model of the investigated valve chamber. The utilized model comprises the inlet channel (1), discharge throttle (2), return spring (3), piston chamber (4), valve piston (5), valve mushroom (6), pilot valve (7), valve chamber (8) and outlet passage (9). During fuel delivery, the sealing seat (10) opens, thus creating a pressure drop between the inlet channel and outlet passage. This state defines the operating points investigated in this chapter.

The discharge throttle, which separates a high-pressure region from a low-pressure region, operates deliberately in the choked flow regime – a regime which has been observed in different experimental and numerical studies [108, 103, 13, 15]. This flow phenomenon limits the mass flow rate through the throttle – the low and high pressure region are decoupled as the mass flow rate becomes practically independent of the downstream pressure variations, i.e. in the valve chamber. Furthermore, the choked flow regime is characterized by a formation of vapor cavities in the throttle. Nozzles and throttles operating in this regime may suffer from erosion damage [108]. In addition to this, intense cavitation in the valve chamber may lead to the damage of the exposed material surfaces if vapor cavities collapse near solid walls. It is therefore essential to obtain a detailed understanding of the flow dynamics of the system. So far, the only possibility to asses the three-dimensional, high-speed cavitating flow field in the mico-size valve chamber is by means of numerical simulation, as the placement of any experimental equipment directly into the flow field is physically not possible or would alter the flow field to a great extent.

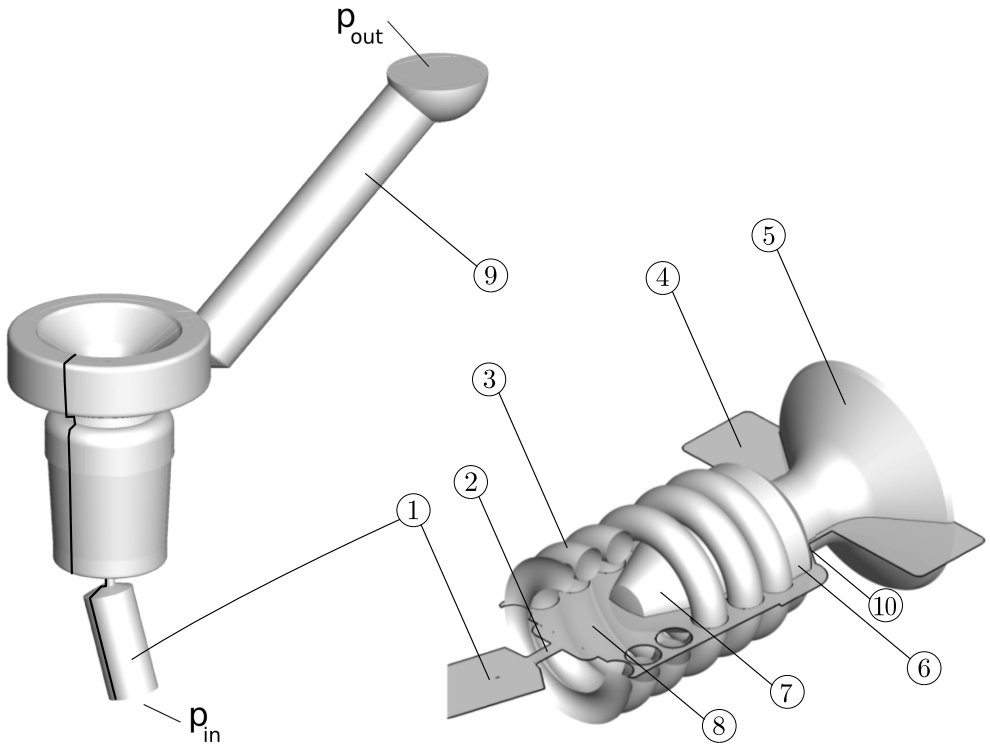

Figure 4.1: Utilized valve chamber of the common rail injection system.

4.1.2 Computational Setup and Numerical Grids

In this study, we employ Diesel test fuel (ISO 4113, Shell-V-Oil 1404) as a working fluid. Saturation properties are taken from Chorążewski et al. [27] for reference temperature $T = 323.15$ K. The barotropic equations of state for pure liquid and liquid-vapor mixture are defined in Chapter 3. As the main focus of this study is put on inertia-driven instabilities, we use a physically inviscid formulation of the governing equations. Neither implicit nor explicit turbulence models are applied. In order to reduce the computational cost and to speed-up the temporal advancement of the solution, we utilize the grid sequencing technique. Once a statistically stationary solution is obtained on the coarse grid, the flow field is interpolated on the finer grid level, where simulation continues. The numerical domain comprises 0.6×10^6 cells on the $Level$ 1 grid with the smallest cell size of 2×10^{-6} m. The $Level$ 2 grid is discretized with 2.6×10^6 hexahedral cells with the smallest cell size of 1×10^{-6} m. Properties of the $Level$ 1 grid and $Level$ 2 grid are summarized in Table 4.1. Highly complex block-structured topology of the numerical grid coupled to the large speed of sound in the liquid phase leads to very small time steps already on the $Level$ 1 grid, thus increasing computational costs dramatically. The utilized $Level$ 1 grid is shown in Fig. 4.2. Complex block-structured topology is depicted in Fig. 4.2 (b). The throttle and chamber regions, where cavitation is expected, are intentionally refined already on the $Level$ 1 grid (mid-plane shown in Fig. 4.1(c)). We adjust refinement of the $Level$ 2 grid manually in order to avoid the occurrence the very small cells in the regions which are not of interest and which decrease the numerical time step.

At the inlet boundary, we set static pressure as given in Table 4.2 and zero velocity gradient. At the outlet boundary, static pressure is set to $p_{out} = 10$ bar for all operating points and zero velocity gradient boundary condition is applied as well. Computation of 1 ms physical time for one operating point took approximately 40000 CPUh in total on the available supercomputing cluster.

	Total cell count [$\times 10^6$]	Min. cell size [$\times 10^{-6}$ m]	Time step [$\times 10^{-9}$ s]
Level 1	0.6	2	2.2
Level 2	2.6	1	0.6

Table 4.1: Grid parameters for the investigated throttle configurations.

operating point	p_{in} [bar]	p_{out} [bar]
OPA	2000	10
OPB	1400	10
OPC	700	10

Table 4.2: Investigated operating points.

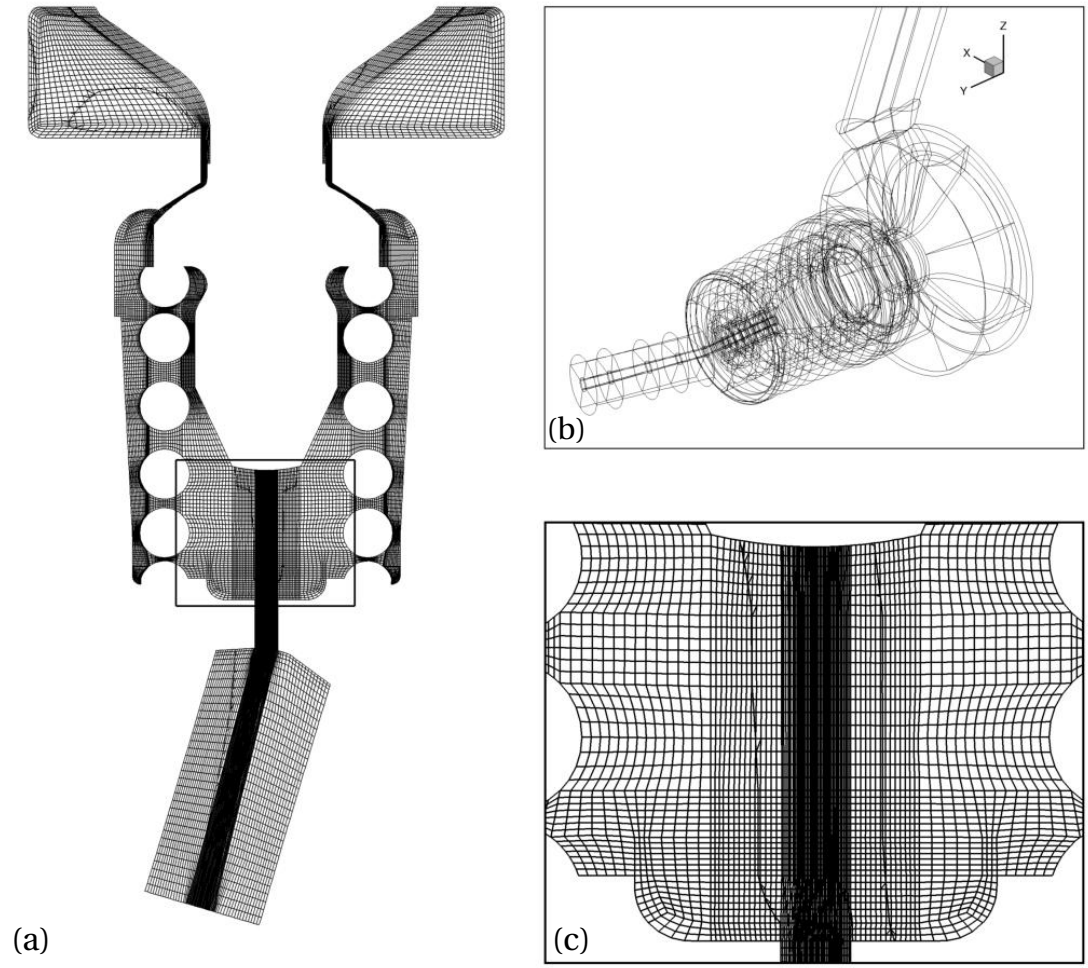

Figure 4.2: *Level* 1 grid of the realistic valve chamber: (a) slice through the mid-plane; (b) blocking topology of the computational domain; (c) magnified view of the grid in the valve chamber.

4.1.3 Results and Discussion

The main focus of this study is to demonstrate the effect of the increased rail pressure on temporal and spatial distribution of cavitating structures and enhanced cavitation erosion when the rail pressure is increased. We believe that the assessment of the flow field by means of numerical simulation can detect material surfaces in the valve chamber which may suffer from erosion damage when this engine measure is applied. For three operating points investigated, we present results obtained at the *Level* 2 grid.

Flow Topology and Cavitating Structures

Figure 4.3 shows the temporal evolution of the global vapor volume. During the initial flow development on the *Level* 1 grid, strong transients are observed (as shown on example of *OPA*), indicating the highly instationary behavior of the flow field. On the *OPA Level* 1 grid, a statistically stationary solution is reached after approximately 0.5 ms of physical time. A decrease in the global vapor volume with a decreased rail pressure is observed as well, thus suggesting a reduction in cavitation intensity.

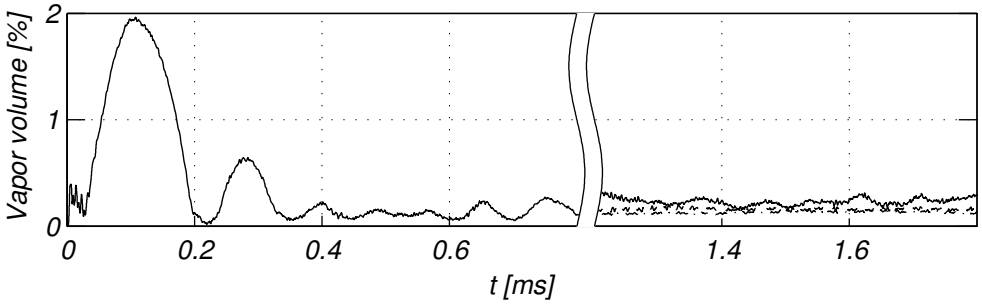

Figure 4.3: Temporal evolution of the global vapor volume for operating points *OPA* (–), *OPB* (– –) and *OPC* (–.). Initial development of the flow field is shown only for *OPA* (left side of the figure).

A three-dimensional topology of the flow field on the example of *OPA* is shown in Fig. 4.4. The imposed pressure difference between the inlet and the outlet boundary plane initiates fluid motion through the computational domain. After leaving the inlet channel, the fluid accelerates through the discharge throttle, with the axial velocity of the liquid jet reaching more than 600 m/s at this particular operating point. The high-speed liquid jet discharges

from the throttle, mixes with the surrounding liquid in the valve chamber and decelerates as it approaches the pilot valve. On the front side of the pilot valve, where a stagnation point forms, the fluid turns in the radial direction. It deflects on the flange of the pilot valve towards the constriction between the coils of the return spring (labeled with 1). Here, the flow impinges on the chamber walls, creating circulatory motion between the spring coils (2) on the one hand, while on the other, flowing towards the valve mushroom and the sealing seat (3). Through the sealing seat, additional pressure drop takes place, accompanied by velocity increase. As the fluid enters the piston chamber, a large circulatory flow pattern establishes (4) along the circumferential direction of the piston chamber. Flow in the valve chamber is characterized by a manifestation of different cavitation mechanisms (e.g. sheet cavitation and vortex cavitation). Figure 4.5 depicts iso-contours of instantaneous cavitating structures colored with the velocity magnitude (left column) and absolute velocity (right column) in the mid-plane for the investigated operating points. Cavitating structures are colored with velocity magnitude. Vapor structures look very similar between the operating points. In the discharge throttle, supercavitating sheet forms (1), due to a strong pressure drop between the inlet channel and the valve chamber. The observed supercavity in the throttle is not symmetric along the circumferential direction and attaches to the left side of the throttle. This is a consequence of the relative inclination of the inlet channel to the discharge throttle causing asymmetric throttle inflow. A similar cavity shape can be observed in injection nozzles when the flow sharply turns [23] or nozzle asymmetry is introduced [90].

By examination of 800 consecutive snapshots, with the temporal distance between two consecutive frames $\Delta t_{frame} \approx 1.1 \times 10^{-7}$ s (which correspond approximately to 0.09 ms of physical time or 140 throttle flow through times based on the throttle length and velocity at the throttle outlet), we observe a mostly stationary cavity in the throttle. Highly instationary vortex cavitation takes place in the low pressure vortex cores at the periphery of the high-speed liquid jet. Vapor clouds generated here are advected to the front side of the pilot valve, where they partially collapse. Flow turning at the sharp-edged flange of the pilot valve causes a strong pressure decrease and the formation of cavity sheets along the frontal flange edge. As these sheets detach from the pilot valve flange, they are advected into the constriction between the spring coils and collapse in the vicinity of coil surfaces. A thin cavity sheet is observed between

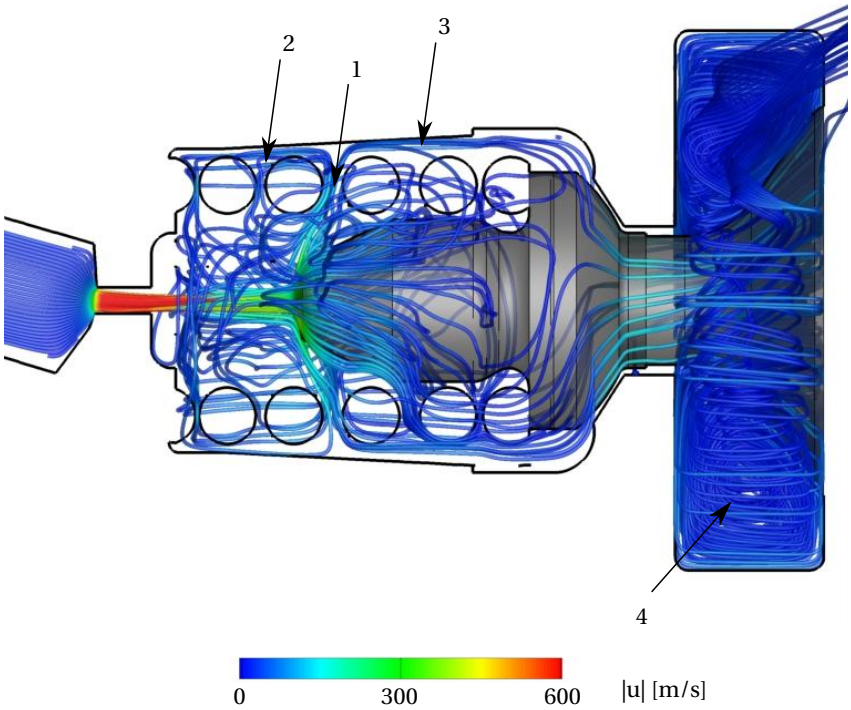

Figure 4.4: Time-averaged topology of the flow field on the example of *OPA*.

two first coils as well (2). A very small gap between two coils and a circulatory flow pattern shown in Fig. 4.4 are the origin of cavitation at this position. However, the most pronounced sheet at this position is observed for the operating point *OPA*. For all operating points, we observe cavitation in the channel above the sealing seat as well (3).

Snapshots of the instantaneous absolute velocity (Fig. 4.5, (b), (d), (e)) show a decrease in the jet velocity with the inlet pressure. Snapshots also demonstrate a slight deflection of the jet due to asymmetric throttle inflow. Disturbances at the jet periphery due to vortex cavitation are visible as well. A straightforward estimation of the exit velocity can be obtained by the Bernoulli equation for the incompressible flow. However, we do not know the chamber pressure *a priori*, as it is part of the solution. Therefore, we compute maximal theoretical velocity by assuming the expansion into the vacuum instead. Thus, the jet velocity at the throttle exit can be approximated as

$$v_{Bernoulli} = \sqrt{\frac{2p_{in}}{\rho_{in}}} \tag{4.1}$$

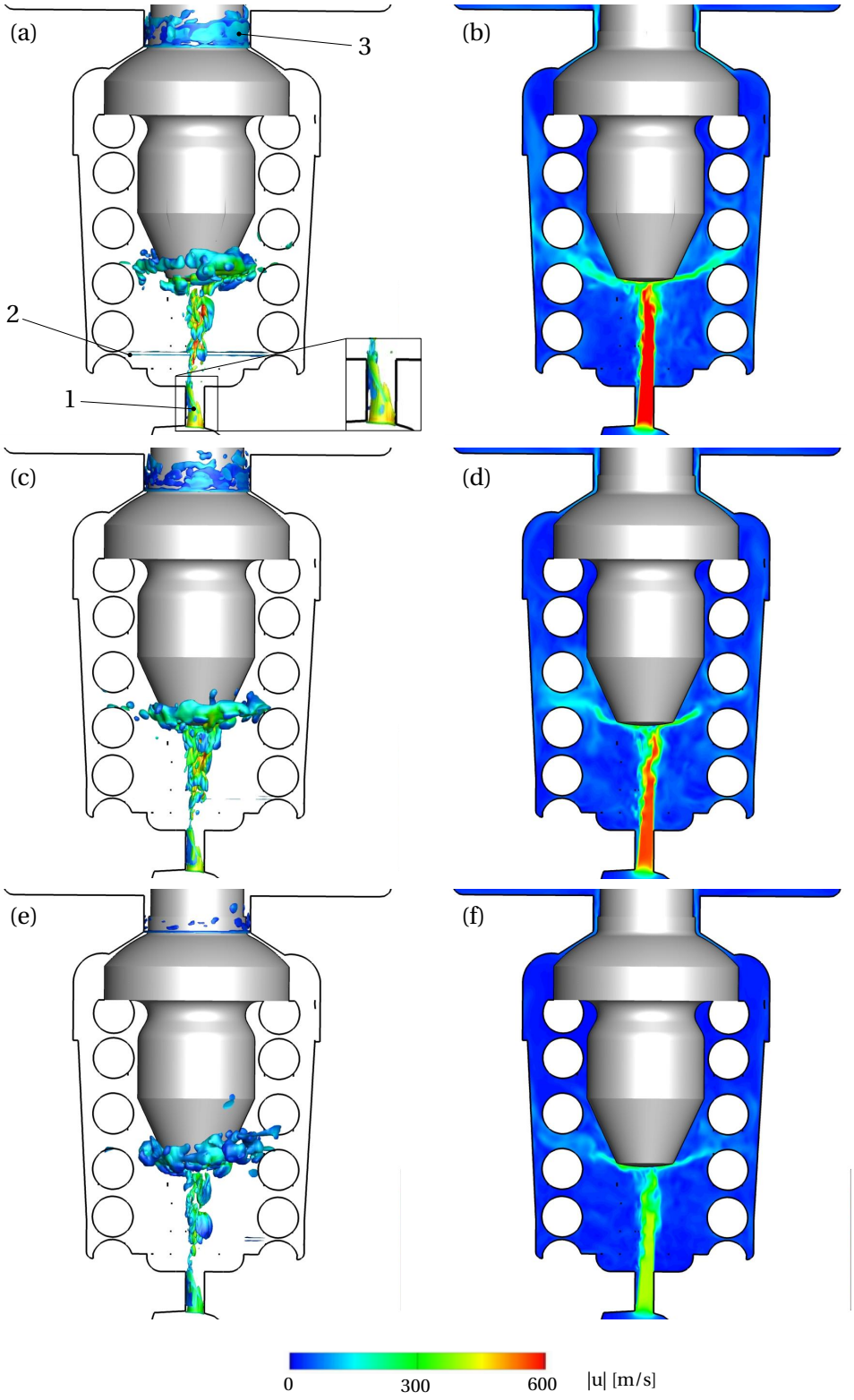

Figure 4.5: Instantaneous snapshots of vapor volume fraction iso-contours $\alpha = 10\%$ colored by absolute velocity (left). Absolute velocity contours in the mid-plane (right). (a)-(b) *OPA*, (c)-(d) *OPB*, (e)-(f) *OPC*.

where p_{in} and ρ_{in} are pressure and density at domain inlet, respectively. Table 4.3 summarizes static pressures and velocities at the throttle exit obtained from simulation and by Eq. 4.1. Pressure and velocity at the throttle exit have been obtained as surface averages of the time-averaged flow field. As expected, theoretical estimates are higher than numerically obtained values due to the expansion into the vacuum assumption and associated hydraulic losses.

We compute discharge coefficients C_d as

$$C_d = \frac{\dot{m}}{\dot{m}_{id}} = \frac{\dot{m}}{A_{th}\sqrt{2\rho_{in}(p_{in} - \langle p_{out}\rangle)}} \tag{4.2}$$

where $\dot{m}$ is the mass flow rate obtained from the simulation, and $\dot{m}_{id}$ a theoretical mass flow rate computed with the nominal throttle area A_{th} and surface-averaged pressure at the throttle outlet $\langle p_{out}\rangle$ obtained from the simulation.

Computed discharge coefficients are nearly the same for investigated operating points, C_d = 0.64. Consequently, we compute cavitation number σ with the surface-averaged pressure at the throttle outlet. Cavitation number σ = 1.03 stays approximately the same for the examined operating points as well. Experimental estimate of the discharge coefficient [80] for circular, sharp-edged orifices at cavitation numbers close to 1 is $C_d \approx 0.61$. We compute a higher value of the discharge coefficient for the investigated throttle geometries. The reason for this behavior can be explained by the magnified view of the supercavitating structure in the throttle (see Fig. 4.5). In the case of the symmetric inflow, the cavity will be distributed along the throttle walls in the circumferential direction, thus reducing nominal throttle area more effectively. This is, however, not the case with the asymmetric inflow, in which cavity attaches on the one side of the nozzle.

operating point	$\langle p_{throttle\ exit}\rangle$ [bar]	$v_{Bernoulli}$ [m/s]	$\langle v_{simulation}\rangle$ [m/s]
OPA	55	676	643
OPB	40	570	534
OPC	24	401	388

Table 4.3: Static pressures and jet velocities at the throttle exit.

4.1.4 Erosion Assessment

Predicting cavitation erosion is crucial for design optimization and improving injector performance. The utilized numerical method resolves the spatial and temporal development of cavitating structures and captures collapse events of isolated vapor clouds. A qualitative estimation of the flow aggressiveness can be obtained by recording maximum wall pressures in each cell during computation. Figure 4.6 shows footprints of the wall loads on the pilot valve. We observe a successive rise of the wall loads with the increase of the inlet pressure. Areas with maximal loads are detected on the pilot valve front. High pressure regions around the stagnation point on the pilot valve front are expected as stagnation point pressure proportionally scales with the imposed inlet pressure. This case also demonstrates a drawback of utilization of maximal pressure criterion as erosion indicator, as it cannot distinguish between stagnation point pressure and pressure peaks originating from the collapses of vapor clouds. Material surfaces with increased wall loads are observed on the pilot valve flank as well. Due to non-symmetrical jet discharging from the throttle, distribution of the wall loads on the flank is non-uniform along the circumferential direction. Distinctive footprints from isolated collapse events can be identified as well. However, for a detailed erosion assessment, more quantitative information about the collapses, including their location, strength, and number density is essential. For this purpose, we employ an algorithm developed by Mihatsch et al. [76], which records collapses of isolated vapor clouds during computation. The algorithm relies on the physical phenomena of a collapsing cavity behaving as a sink in the flow field. It detects computational cells where complete condensation occurs and evaluates velocity divergence in their vicinity. Once a collapse is detected, its position, time, and instantaneous pressure are stored. A more detailed description of the algorithm can be found in the aforementioned publication. Figure 4.7 (a) shows spatial distribution of detected collapse events within the computational domain on the example of *OPA*. A single event is represented by a sphere whose size and color are proportional to the strength of the event. Events are identified predominantly in the valve chamber with a few in the channel above the sealing seat. The scatter plot reveals a dense collapse accumulation in the shear layer between the throttle exit and the pilot valve. Events are detected near material surfaces between the spring coils as well. As the cavity sheet in the throttle is relatively stable, no events are identified here. A

quantitative comparison between the investigated operating points is shown in Fig. 4.7 (b). A diagram depicts cumulative rates of collapse events detected in the whole simulation domain for *OPA*, *OPB* and *OPC*, respectively. We define the cumulative collapse rate as a number of collapse events detected above specific pressure threshold and normalized by time. From the diagram we can read that approximately four time more events per second above 6000 bar are detected for *OPA* than for *OPB*. No events above this threshold are found for *OPC*. This plot clearly demonstrates the increase in the collapse event intensity and quantity with an increased rail pressure.

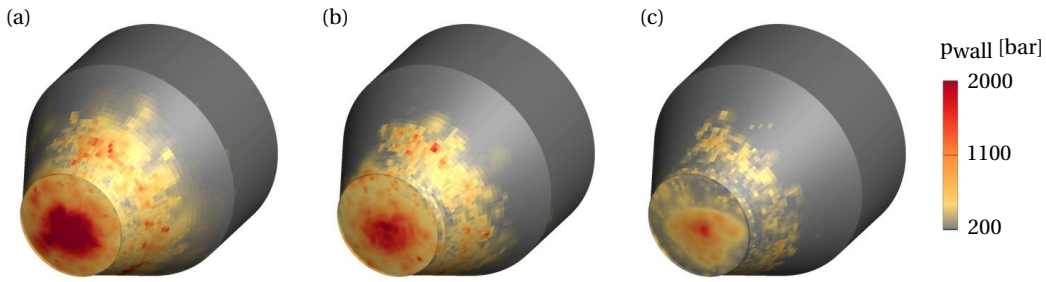

Figure 4.6: Detected wall loads on the pilot valve. (a) *OPA*, (b) *OPB*, (c) *OPC*.

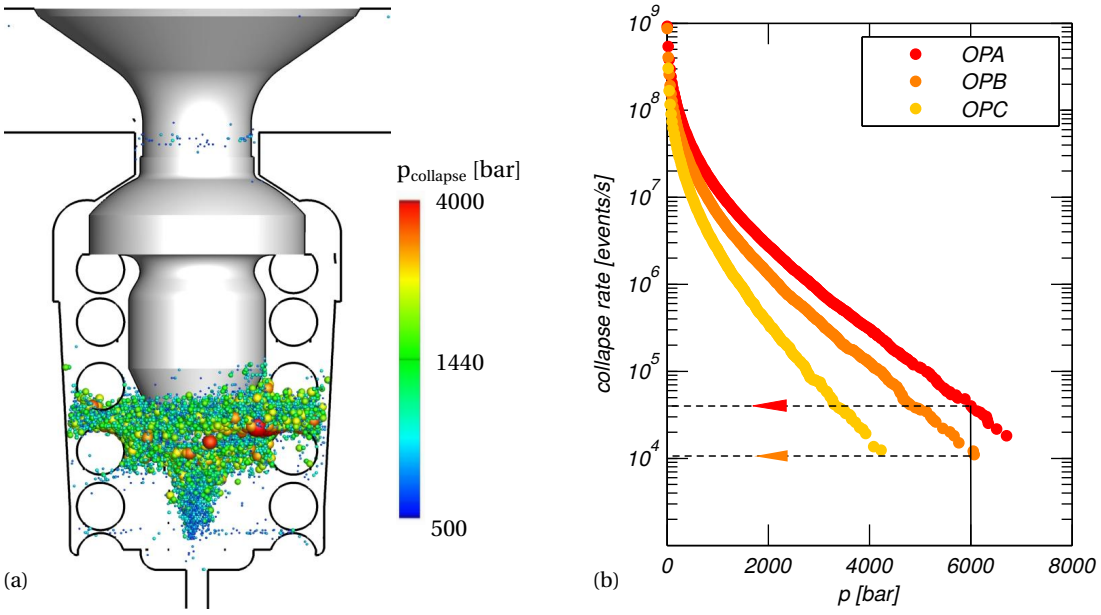

Figure 4.7: (a) Detected collapse events on the example of OPA. Each event is depicted by a sphere whose size and color scales with the collapse pressure. (b) Cumulative rate of collapse events in the computational domain for investigated operating points.

4.2 Generic Model

The complex geometry of the realistic valve chamber greatly increases the time needed for the generation of the block-structured grid topology and computational costs. Therefore, we develop a simplified model of the valve chamber and make a compromise between computational costs and geometric complexity. The generic model is depicted in Fig. 4.8. Its dimensions resemble those of the realistic valve chamber. However, our model includes only the inlet and outlet channels, valve chamber, discharge throttle and pilot valve. Similar geometries, found in the open literature [58, 10], are utilized for a study of the cavitating channel and throttle flows. Geometric properties of the throttles are given in Table 4.4. The distance between the throttle or step-hole exit and the pilot valve is 1 mm and is kept unchanged for all designs. The employed model enables a simplification of the complex flow field into more canonical cavitating flows, isolates different physical cavitation phenomena that arise in the valve chamber, and makes the numerical simulation computationally efficient. Furthermore, the utilization of different throttle geometries into the block-structured grid topology is straightforward. Figure 4.9 shows discharge throttle designs investigated in the scope of the thesis. Designs A, B and C are utilized for the investigation of the influence of throttle geometry on flow dynamics. Therefore, throttles are designed with a distinctive conicity factor which is defined as

$$K = 100 \times \frac{d_{in} - d_{out}}{l}, \tag{4.3}$$

where d_{in} and d_{out} are throttle inlet and outlet diameters, respectively, and l is the throttle length, which is the same for all designs. A positive K factor indicates a reduction of the cross section area towards the throttle exit and vice versa. In Chapter 5 we examine the influence of the throttle conicity on the cavitation development and flow dynamics.

Designs D and E feature a step-hole mounted on the sharp-edged cylindrical throttle. These designs enable an assessment of the step-hole diameter on cavity dynamics. The results of this simulations are presented in Chapter 6.

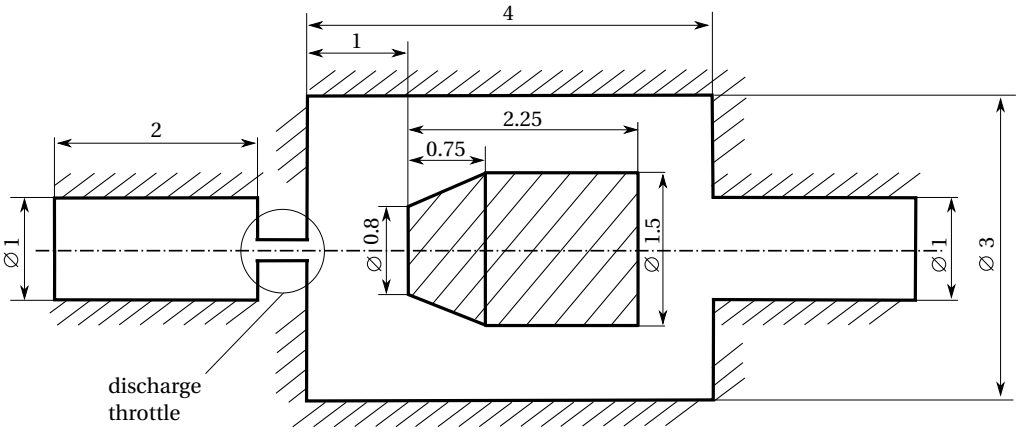

Figure 4.8: Sketch of the generic valve chamber model. All dimensions are given in millimeters.

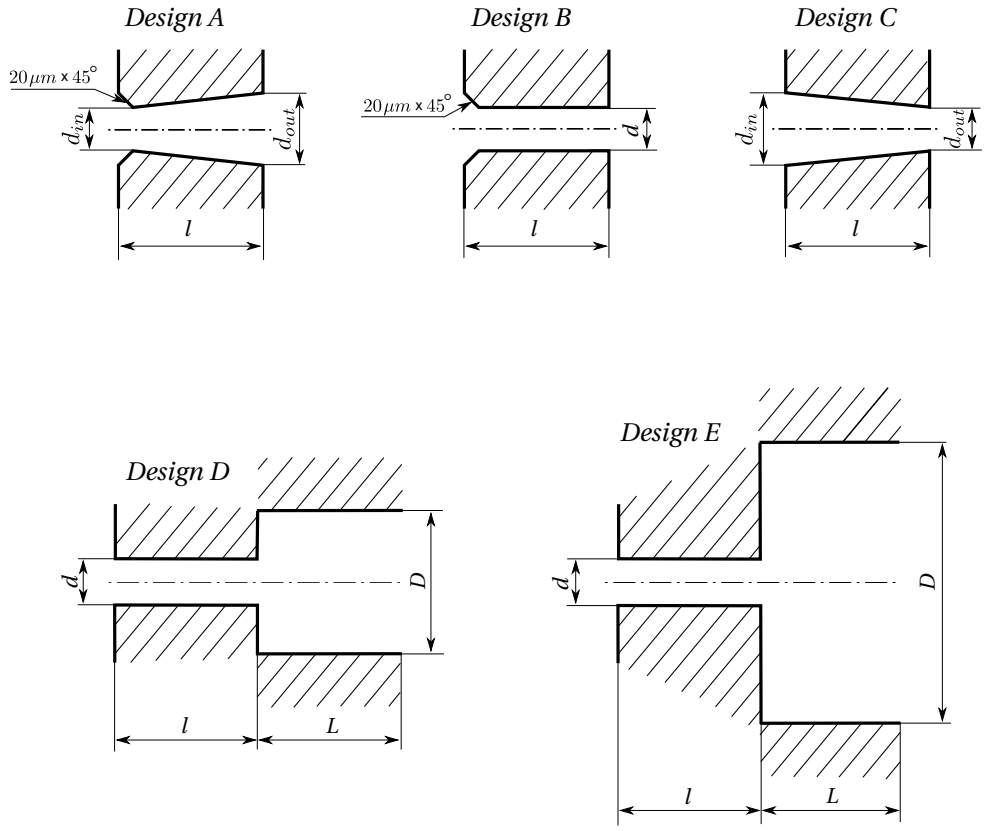

Figure 4.9: Sketches of generic throttle designs. Designs D and E feature a sharp-edged cylindrical throttle and a step-hole mounted on top of it.

Design	d_{in} [μm]	d_{out} [μm]	d [μm]	D [μm]	l [μm]	L [μm]	K
A	182	192	×	×	500	×	-2
B	×	×	182	×	500	×	0
C	200	190	×	×	500	×	+2
D	×	×	200	500	500	500	0
E	×	×	200	1000	500	500	0

Table 4.4: Geometric properties of investigated throttle designs.

4.3 Summary

The study in the present chapter demonstrates the effect of the increased rail pressure on flow in the realistic valve chamber. Three operating points with the increased inlet pressure are considered. A barotropic equation of state for Diesel test fuel is employed.

A steady supercavitating cavity is observed in the discharge throttle for all operating points. Furthermore, annular shaped vapor clouds form in the low pressure cores at the periphery of the high-speed liquid jet that discharges from the throttle. In addition to this, cavities form at the pilot valve flange and between the spring coils. Although the instantaneous cavitating structures look similar, the aggressiveness of flow in the valve chamber changes dramatically. Material surfaces prone to cavitation damage are assessed by recording maximum pressure in computational cells and by employing the collapse detection algorithm. The most aggressive flow field is found for the operating point with the highest inlet pressure.

Due to the high pre-processing and computational costs associated with the set-up and simulation of flow in the realistic valve chamber, a simplified chamber model is developed. The generic model enables investigation of canonical flow configurations at the reduced computational effort.

5 Influence of Throttle Geometry

In this chapter, we investigate a cavitating flow in the generic valve chamber of a common rail injector for three different designs of the discharge throttle. First, computational models and numerical setup are introduced. Next, a general overview of the flow topology in the valve chamber on the example of Design A is given and integral flow quantities are discussed. Additionally, we perform a grid resolution study for Design A. Finally, we carry out an assessment of the flow dynamics and erosion risk prediction for each design.

5.1 Computational Setup

Computational designs considered in this chapter have been described in detail in Chapter 4, Table 4.4. We investigate Designs A, B, and C, which differ in the geometric properties of the discharge throttle. Design A features a throttle with a negative K factor and chamfered intake section, Design B represents a cylindrical throttle with the intake chamfering, whereas Design C features a sharp-edged throttle with a positive K factor. Investigated discharge throttle geometries are adjusted to ensure that mass flow rates are approximately identical for the specific operating point.

We utilize Diesel test fuel (ISO 4113, Shell-V-Oil 1404) as a working fluid. Saturation properties are taken from Chorążewski et al. [27] for reference temperature $T = 323.15$ K. The barotropic equations of state for pure liquid and liquid-vapor mixture are defined in Chapter 3. As the main focus of this study is put on inertia-driven instabilities, we use a physically inviscid

formulation of the governing equations. Neither implicit nor explicit turbulence models are applied. At the inlet boundary, we prescribe static pressure p_{in} = 2000 bar and zero velocity gradient. At the outlet boundary, static pressure is set to p_{out} = 60 bar and zero velocity gradient boundary condition is applied as well. The applied boundary condition for pressure is weakly reflective and convergence to the prescribed inlet and outlet values is guaranteed asymptotically. Static pressure set at the outlet boundary corresponds to the chamber pressure obtained from the simulation of the realistic design. Solid boundaries are treated as adiabatic, inviscid walls. The whole domain is initialized with fluid at rest at the outlet pressure p_{out}. Additionally, we let the inlet pressure linearly increase during the start-up phase, from the outlet value to the target inlet pressure, in order to avoid numerical instabilities that can arise due to large pressure gradients across the throttle.

Figure 5.1 depicts the utilized computational model of the generic valve chamber together with the inlet and the outlet plane where boundary conditions are applied.

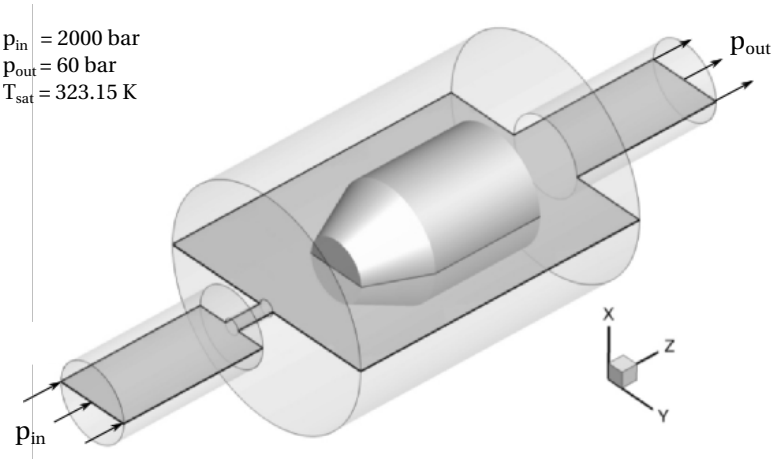

Figure 5.1: Computational model of the generic valve chamber.

5.2 Discharge Properties and Characterization of the Throttle Flow

Before giving a general overview of the flow topology in the generic valve chamber for the above specified operating point, we first describe difference in the discharge properties of the utilized throttle designs. Diagram 5.2 (top) depicts the dependency of the discharge coefficient C_d over cavitation number σ (as defined by Eq. 2.2) for the employed designs at different

operating points. We compute discharge coefficient C_d as

$$C_d = \frac{\dot{m}}{\dot{m}_{id}} = \frac{\dot{m}}{A_{th,out}\sqrt{2\rho_{in}(p_{in} - p_{out})}}, \tag{5.1}$$

where $\dot{m}$ is the mass flow rate obtained from simulation, $A_{th,out}$ is the nominal throttle outlet area, ρ_{in} and p_{in} are the density and the static pressure at the inlet plane and p_{out} is the static pressure at the outlet plane, respectively. Curve describing an integral mass flow rate at the throttle outlet can be divided into the Bernoulli and the choked segment. At the Beronoulli segment, the mass flow rate scales with the square root of the pressure difference across the throttle $\dot{m} \sim \sqrt{\Delta p}$, resulting in the nearly constant discharge coefficient. However, as the pressure difference increases, the first cavitation sites form at the throttle intake lip (cavitation inception). If the pressure in the outlet chamber is further reduced, the cavity in the throttle elongates and the integral mass flow rate soon becomes decoupled from the outlet pressure. The point between the Bernoulli and the choked segment is also known as the critical cavitation point (CCP) [60] and agrees with the OP2 for Design A. In the choked flow regime, the throttle discharge reduces, as the evaporation rate in the throttle increases and the cavitating sheet elongates. At low cavitation numbers, the cavitating sheet occupies the whole throttle in the longitudinal direction. This regime is also known as supercavitation. Figure 5.2 (bottom) depicts three operating points at different cavitation numbers on the example of Design A. At OP1, which corresponds approximately to cavitation inception, cavitation sites appear on the inlet edge, forming a ring-shaped cavity. At OP2, the cavity extends further downstream. In this transitional regime, the cavity sheet separates from the cavity at the inlet lip and is shed downstream. Furthermore, the integral mass flow rate stays approximately constant from now on. A supercavitating regime establishes at OP3 with the cavity sheet occupying the whole throttle length. Throughout this work, it is only the operating point at low cavitation numbers, i.e. in the supercavitating regime far below the CCP, which is a matter of interest.

The solid line in Fig. 5.2 depicts the analytical relation for the discharge coefficient of the sharp-edged, cylindrical orifice once cavitation appears: $C_d = C_c\sqrt{\sigma}$ [80]. Here, we assume contraction coefficient $C_c = 0.61$. Once cavitation develops, discharge characteristics of all investigated throttles remain above the solid line, which represents a lower theoretical

limit. Design B shows the highest C_d, due to the chamfered inlet section and the smallest cross-section area. The effect of the chamfered inlet is equivalent to the inlet rounding, which is known to increase the discharge [96]. Designs A and C show very similar discharge characteristics in the choked segments, as the outlet cross-section areas differ about 2 %.

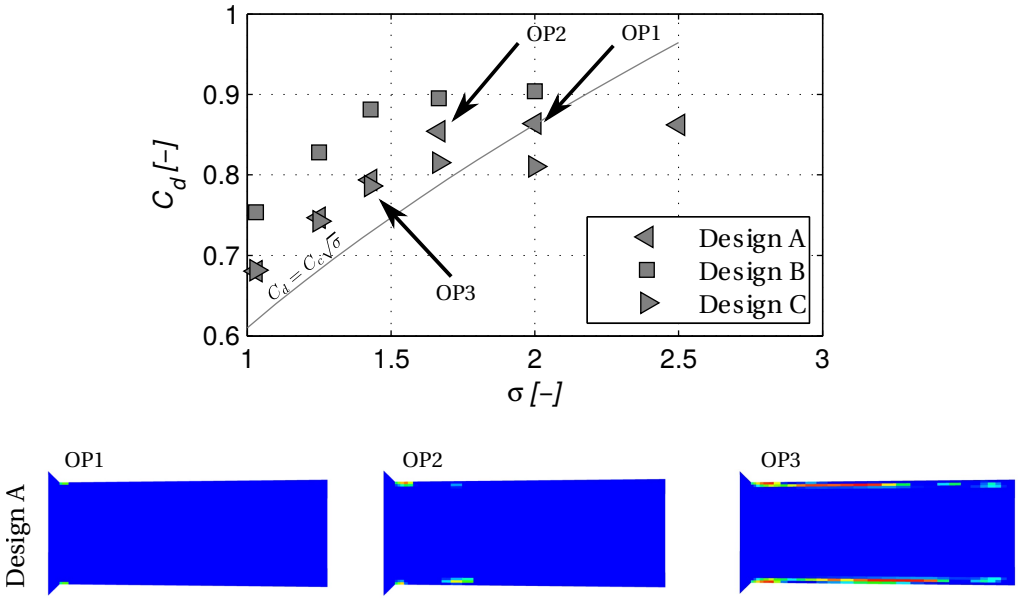

Figure 5.2: Top: Effect of the cavitation number on the discharge characteristics of the throttles. The solid line depicts theoretical behavior of the discharge for the sharp-edged throttle [80]. Bottom: OP1–cavitation inception, OP2–critical cavitation point (CCP), OP3–supercavitating regime, on the example of Design A.

5.3 Flow Field Topology

The visualization of the three-dimensional flow field topology for the operating point with p_{in} = 2000 bar and p_{out} = 60 bar is given in Fig. 5.3. Here, time-averaged streamlines in the whole domain on the example of Design A are shown, colored with the velocity magnitude. The time-averaged flow field topology is essentially the same for the designs investigated in this chapter. Between the throttle inlet and outlet, static pressure drops strongly, causing a substantial acceleration of the fluid. The liquid jet discharges from the throttle with the velocity reaching almost 700 m/s. In the chamber, the jet mixes with the ambient liquid, decelerates and meets the front side of the pilot valve where a stagnation point forms. After hitting the pilot valve, the fluid turns radially by 90° and flows towards the chamber walls.

This forms a large circulatory pattern along the circumferential direction and leads to the appearance of corner vortices (labeled with 1). In Fig. 5.3, we also observe an additional vortex that forms between the pilot valve flange and chamber walls (labeled with 2). Although the corner vortex marked with 1 is present in the realistic geometry as well, its effect is much less pronounced due to the obstruction introduced by the return spring. However, the formation of these vortices in the present design is inevitable.

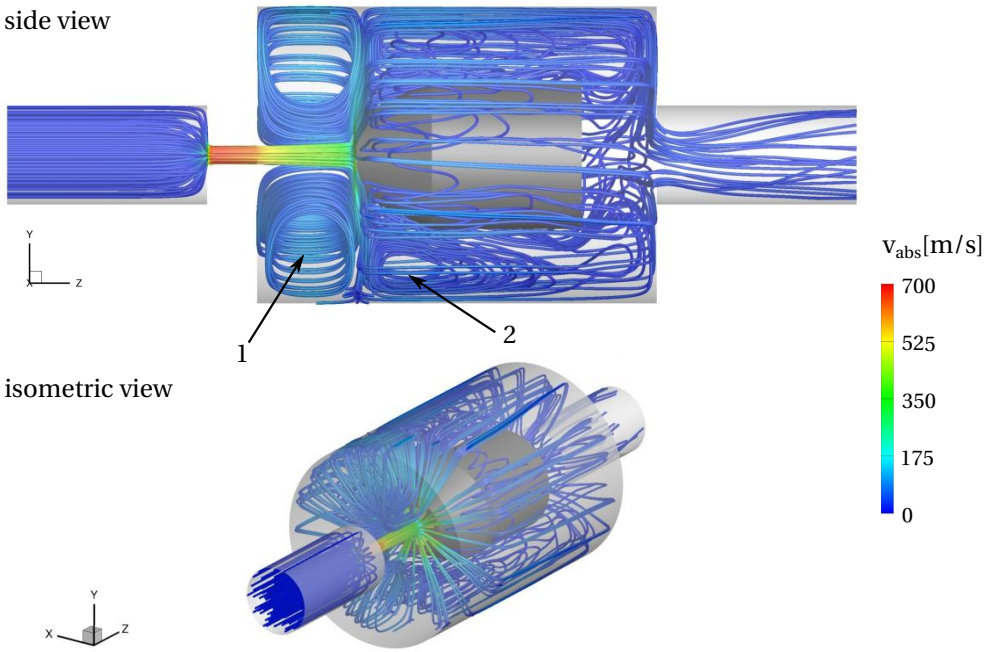

Figure 5.3: Time-averaged topology of the flow field on the example of Design A.

5.4 Grid Sensitivity Study

We assess the sensitivity of the spatial resolution on the valve chamber flow on the example of Design A. We create three grid stages with a successive refinement of the computational domain (*Level 1, Level 2* and *Level 3*). Table 5.1 lists grid sizes and parameters for the utilized throttle configurations. Special attention is given to the satisfactory resolution of the discharge throttle, as the inherent shedding instabilities originating from the throttle are expected. Therefore, the number of cells in the throttle is systematically increased along both the longitudinal and circumferential direction. At *Level 2* and *Level 3*, near-wall mesh resolution is additionally refined, resulting in the height of the first near-wall cell smaller than 1 μm. The

	grid	total cell count [$\times 10^6$]	$N_{cells,l}$	$N_{cells,d}$	Δ_{wall}[$\times 10^{-6}$ m]
Design A	*Level 1*	0.66	30	40	4.3
	Level 2	4.016	96	76	0.850
	Level 3	8.098	120	115	0.365
Design B	*Level 1*	0.66	30	40	4.3
	Level 2	4.016	96	76	0.93
Design C	*Level 1*	0.65	32	40	4.7
	Level 2	4.089	96	84	0.96

Table 5.1: Grid parameters for investigated throttle configurations. $N_{cells,l}$-number of the cells along the throttle length, $N_{cells,d}$-number of cells across the throttle diameter, Δ_{wall}-height of the first near-wall cell.

block-structure topology of the numerical domain is given in Fig. 5.4 together with *Level 3* resolution in the domain mid-plane. Figure 5.5 depicts a close-up view of the throttle at the relevant grid level.

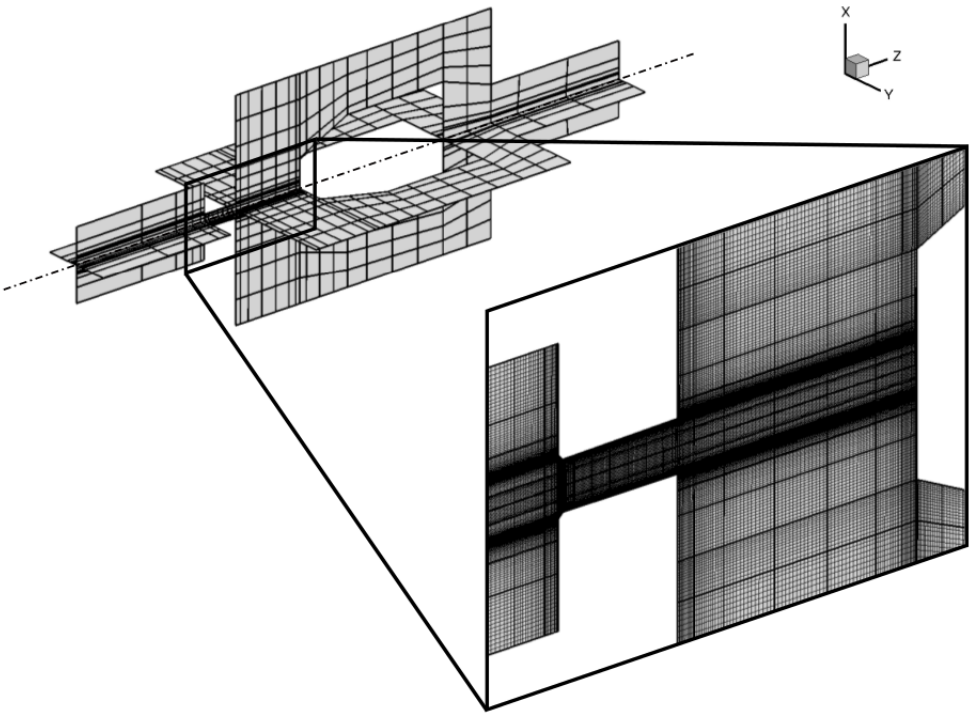

Figure 5.4: Topology of the block-structured grid and resolution at the *Level 3* grid.

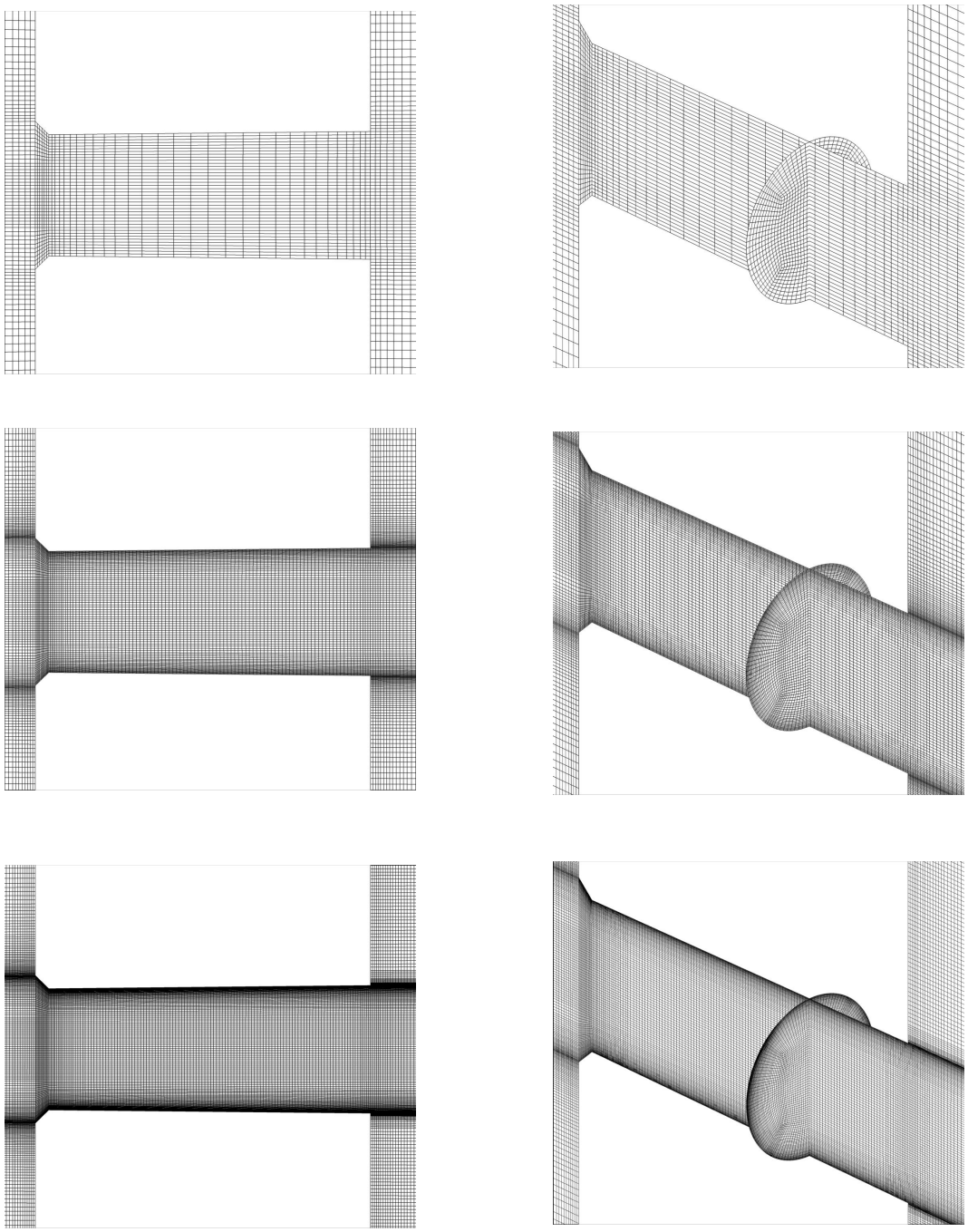

Figure 5.5: Resolution of the throttle at different grid levels. Top: *Level* 1, Middle: *Level* 2, Bottom: *Level* 3.

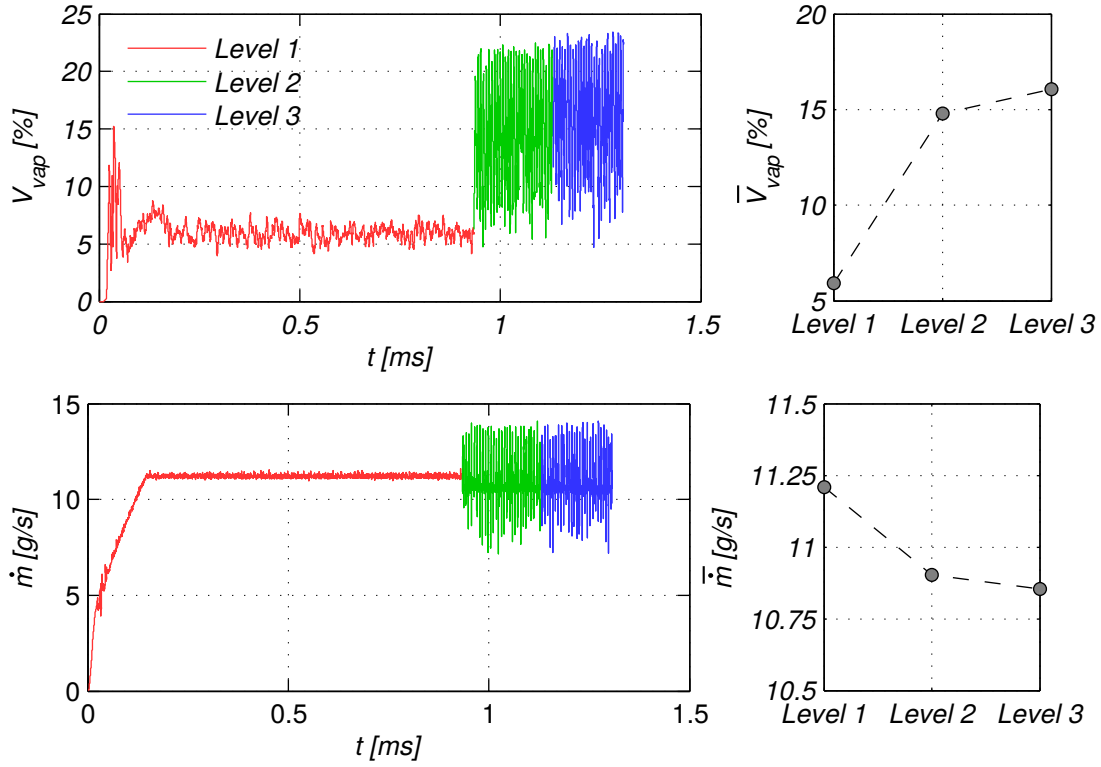

Figure 5.6: Temporal evolution of the vapor volume in the throttle (normalized with the throttle volume) and mass flow rate at the throttle exit at different grid resolutions. Diagrams on the right hand side show the time-averaged values of the relevant quantities.

Further, we employ a grid sequencing technique and interpolate the numerical solution on the subsequent grid level in order to minimize computational costs. At each grid level, we let the flow field develop until a statistically stationary behavior is observed. A temporal evolution of the relevant integral flow quantities – mass flow rate at the throttle exit and vapor volume in the throttle – is presented in Fig.5.6. Significant oscillations of integral flow quantities are visible at grid *Level* 2 and *Level* 3. Grid refinement increases the evaporation rate in the throttle and in the chamber, as the cavitating sheet and vapor structures are better resolved. In contrast, the mass flow rate measured at the throttle outlet drops between the subsequent grids. Figure 5.7 shows the resolution of the cavitating sheet (shown as the contours of the vapor volume fraction α) in the vicinity of the throttle intake for different grid resolutions. At *Level 1*, just two cells cover the extent of the sheet in the wall-normal direction, resulting in an under-resolved cavity. As the resolution increases, cavity thickens, resulting in the more pronounced blockage of the core flow, i.e. in the reduction of the cross-section area and

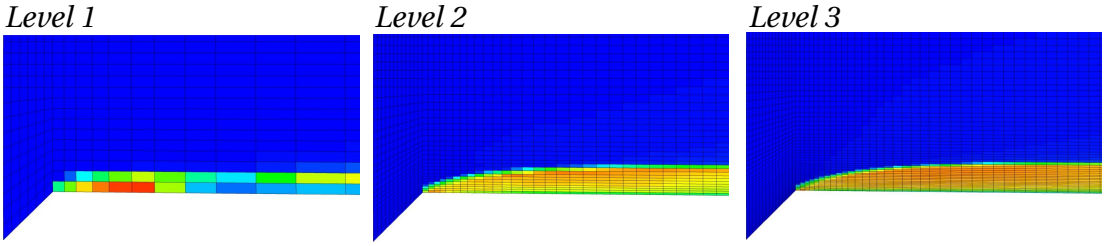

Figure 5.7: Resolution of the cavitating sheet in the vicinity of the throttle intake at different grid levels.

thereby associated decrease of the mass flow rate.

In the following paragraph, we discuss the representation of the shedding frequency with respect to the grid refinement level. By visual inspection of flow snapshots and computation of the power spectral density, we associate the oscillations shown in Fig. 5.6 to the shedding instabilities developing in the throttle. Figure 5.8 depicts the pre-multiplied power spectral density of the vapor volume and the mass flow rate for different grid levels. Spectra are computed using the *pwelch* algorithm provided in the MATLAB software package. We apply the Hanning window to four segments of input data with an overlap of 50 %. Data are sampled every fifth time step. Shedding frequency f_s and its harmonics (f_{s1}, f_{s2}) are represented satisfactorily at grids $Level$ 2 and $Level$ 3 in both quantities ($f_s \approx 150$ kHz, $f_{s1} \approx 290$ kHz). One peak is also observed in the frequency range from 105-125 kHz at $Level$ 1 grid. However, by visual inspection of the flow field on that grid level, we do not observe a consistent shedding cycle.

We demonstrated that physical phenomena governing the unsteady behavior of the cavity sheet are adequately reproduced already at *Level 2*. Considering the high computational costs associated with the *Level 3* (see Table 5.2), the choice of *Level 2* grid seems to be a reasonable one for a comparative study of different designs at a still affordable computational effort.

	grid	$\Delta t[\times 10^{-10}\ s]$	CPU	CPUh
Design A	*Level 1*	6	56	1500
	Level 2	1.3	560	47000
	Level 3	0.56	616	260000

Table 5.2: Computational costs associated with different grid resolutions required for computation of 1 ms physical time.

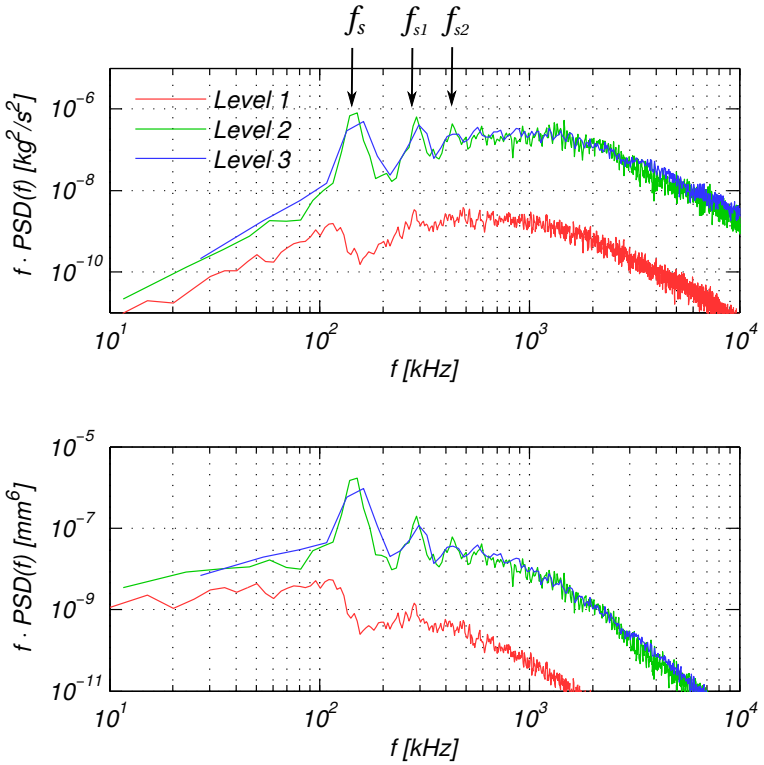

Figure 5.8: Pre-multiplied power spectral density of the mass flow rate at the throttle outlet (top) and vapor volume in the throttle (bottom) for three different grid resolutions.

5.5 Analysis of Cavity Dynamics

In this section, we discuss the instationary cavity motion observed in the discharge throttle. Figure 5.9a shows the temporal evolution of the mass flow rate at the throttle exit and the vapor volume within the throttle during the time period $T = 0.05\ ms$ on the example of Design A. A periodic pattern can be observed in both plotted quantities, indicating the existence of a shedding mechanism in the throttle. For the purpose of the present analysis, the shedding cycle can be divided into two segments – the growth phase of the cavity sheet and the sheet collapse, which is accompanied by a re-entrant motion. For the considered throttle configurations, we observe two types of re-entrant motion that develop simultaneously: re-entrant jet and bubbly shock. Six representative instants in time, marked with (a)-(f), are shown in Fig. 5.10. In the snapshot (a), the velocity along the throttle walls is negative and points in the opposite direction to the core flow. On the phase boundaries between the core flow and the cavitating sheet, re-entrant motion induces vorticity, thus creating many vapor fragments.

Furthermore, the vapor volume shows here a local minimum. Advection of vapor fragments towards the exit of the throttle causes severe oscillations in the mass flow rate due to the density reduction of the vapor phase. After this time instant, the velocity near the wall changes its sign and the re-entrant motion disappears. Time instant (b) depicts the development of a new cavity in the throttle. There is also a vapor cloud visible at the throttle exit, which causes oscillations of the mass flow rate. Just shortly before the cavity sheet reaches the throttle exit (c), the mass flow rate experiences a local maximum, followed by a rapid drop (d), as the annular vapor sheet reduces the nominal area at the throttle outlet. In the time instant when the cavitating sheet reaches the throttle exit (c), an annular vapor cloud forms and is advected towards the pilot valve front. Re-entrant motion, beginning at (d), causes a decay of the vapor volume in the throttle and stabilizes the mass flow rate. Snapshots (e) and (f) show a propagation of the re-entrant motion in the throttle. Once the throttle intake lip is reached, the shedding cycle starts anew. The indicator that the cavity sheet covers the whole throttle along the longitudinal direction is the rapid drop of the mass flow rate, not the local maximum in the vapor volume (see Fig. 5.9a, 5.9b). However, maxima in the vapor volume indicate the onset of the re-entrant flow and the beginning of the sheet cavity collapse. The temporal offset between these two maxima arises as the cavity slightly exceeds the throttle length and the re-entrant flow doesn't get established immediately. This is generally observed for all three designs, but is most distinct for Designs A and B. For six shedding cycles shown in Fig. 5.9a, we observe nearly the same growth and decay rate of the cavity in the throttle and a strong regularity of the dynamics. Although the re-entrant jet and the bubbly shock are observed simultaneously, the latter mechanism is more distinct in Design A. At most shedding cycles, the front of the bubbly shock is clearly visible and consistent in the circumferential direction. However, at some time instants it is less recognizable, since the flow varies in the circumferential direction as well. High-speed imaging of cavitation in the large-scaled nozzle in the submerged environment demonstrated cavity dynamics that adhered to the presented inviscid solution [24]. Authors reported pulsating behavior of the cavity which was qualitatively the same. Further, a scale-independent performance of the nozzle was addressed.

The flow dynamics in Designs B and C resembles that of Design A, but there are differences as well. The peaks in the mass flow rate are less pronounced, i.e the amplitude of the oscillations

decreases compared to Design A. We also observe fewer shedding cycles during the same time interval and a decrease in the vapor volume. In the case of Design C, the differences are even more pronounced. Generally speaking, the flow seems to be more of a random nature. During the growth of the cavity in Designs B and C, rather small vapor fragments coalesce and merge

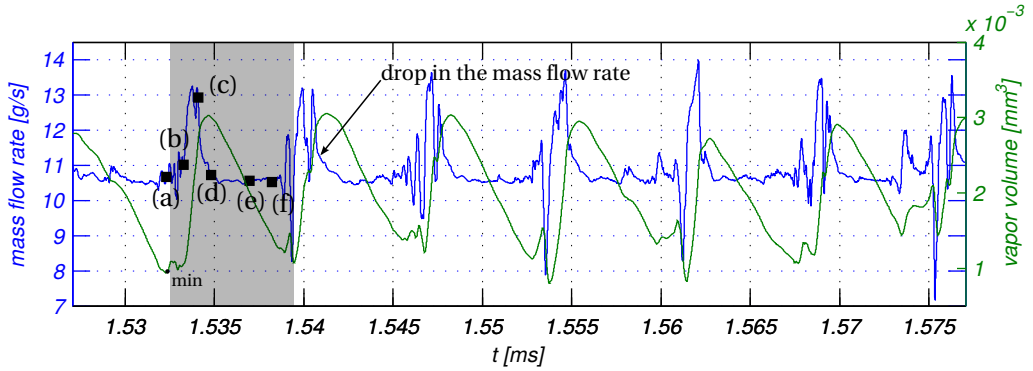

(a) Design A

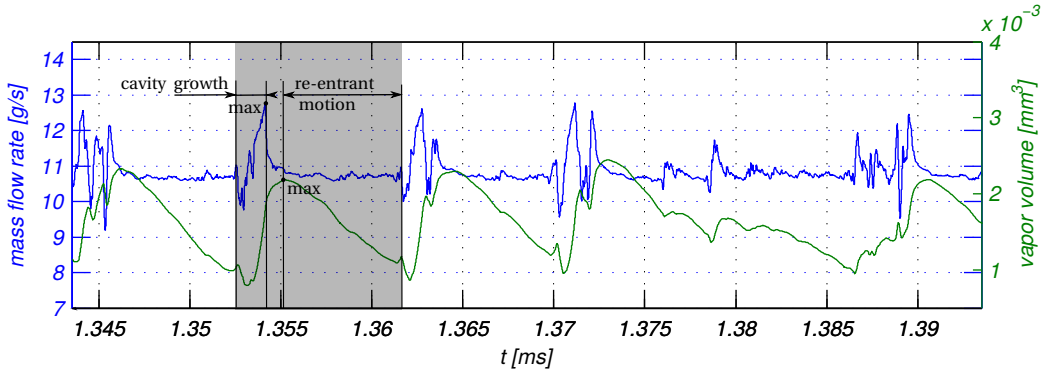

(b) Design B

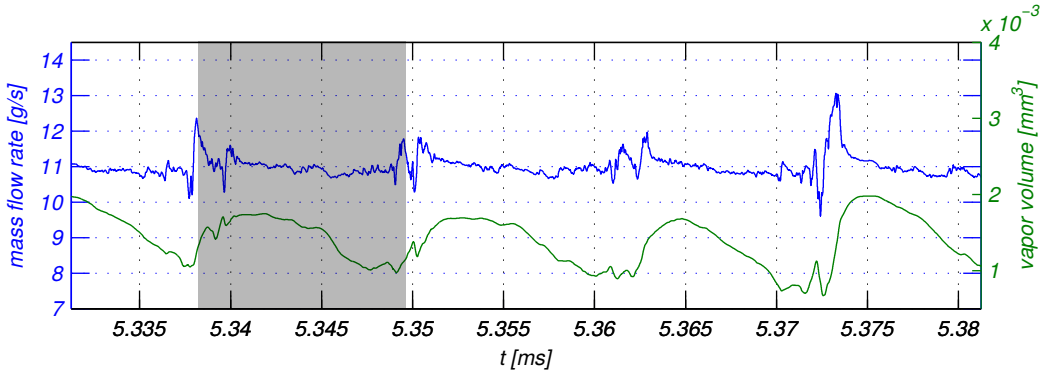

(c) Design C

Figure 5.9: Temporal evolution of mass flow rate (blue curve) and vapor volume (green curve) during the time period $T = 0.05$ ms. Gray areas mark the cavity oscillation period.

together, thus forming one enclosed vapor sheet that spans through the throttle. In case of Design B, this happens at some shedding cycles (e.g. 1.378 ms - 1.385 ms in Fig. 5.9b), whereas at Design C this occurs almost during every observed shedding cycle. This behavior differs from the Design A configuration, where a clear front evolves through the throttle. A similar phenomenon was also observed by Callenaere et al. [25] for very thin cavities, i.e. where thickness of the cavity sheet is small compared to that of the re-entrant motion.

5.5.1 Frequency Spectra

An accurate estimate of the shedding frequency is obtained by applying the Fast Fourier Transform to the signals of the mass flow rate and vapor content in the throttle. The spectra are computed using Welch's method provided within MATLAB software package and are shown in Fig. 5.11. Power spectral densities are estimated by applying the Hanning window to 4 overlapping segments of input data. The entire signal consists of 2^{19} data points with temporal distance $\Delta t \approx 6.7 \times 10^{-10}$ s between two successive points. The spectra of the mass flow rate and vapor content in the throttle show the same trend. Design A features one dominant frequency at approximately 140–150 kHz and at least two additional harmonic frequencies are observed. The dominant frequency corresponds to the shedding frequency of the cavity in the throttle. The shedding frequencies of Design B and Design C are estimated to 110 kHz and 85 – 95 kHz, respectively. In the investigated designs, the interaction of the re-entrant flow with the cavity interface is very complex, as the re-entrant flow breaks the cavity interface at many positions. The distinction between the bubbly shock and the re-entrant jet is thus not always straightforward.

5.5.2 Strouhal Numbers and Estimation of the Re-entrant Velocity

The unsteadiness of the flow can be quantified by the Strouhal number. In this context, the Strouhal number can be understood as the ratio of the time needed for the re-entrant motion to reach the throttle intake and the time period of the cavity shedding. We utilize the following definition:

$$St = \frac{f_s \times l_{max}}{v_c}\,, \tag{5.2}$$

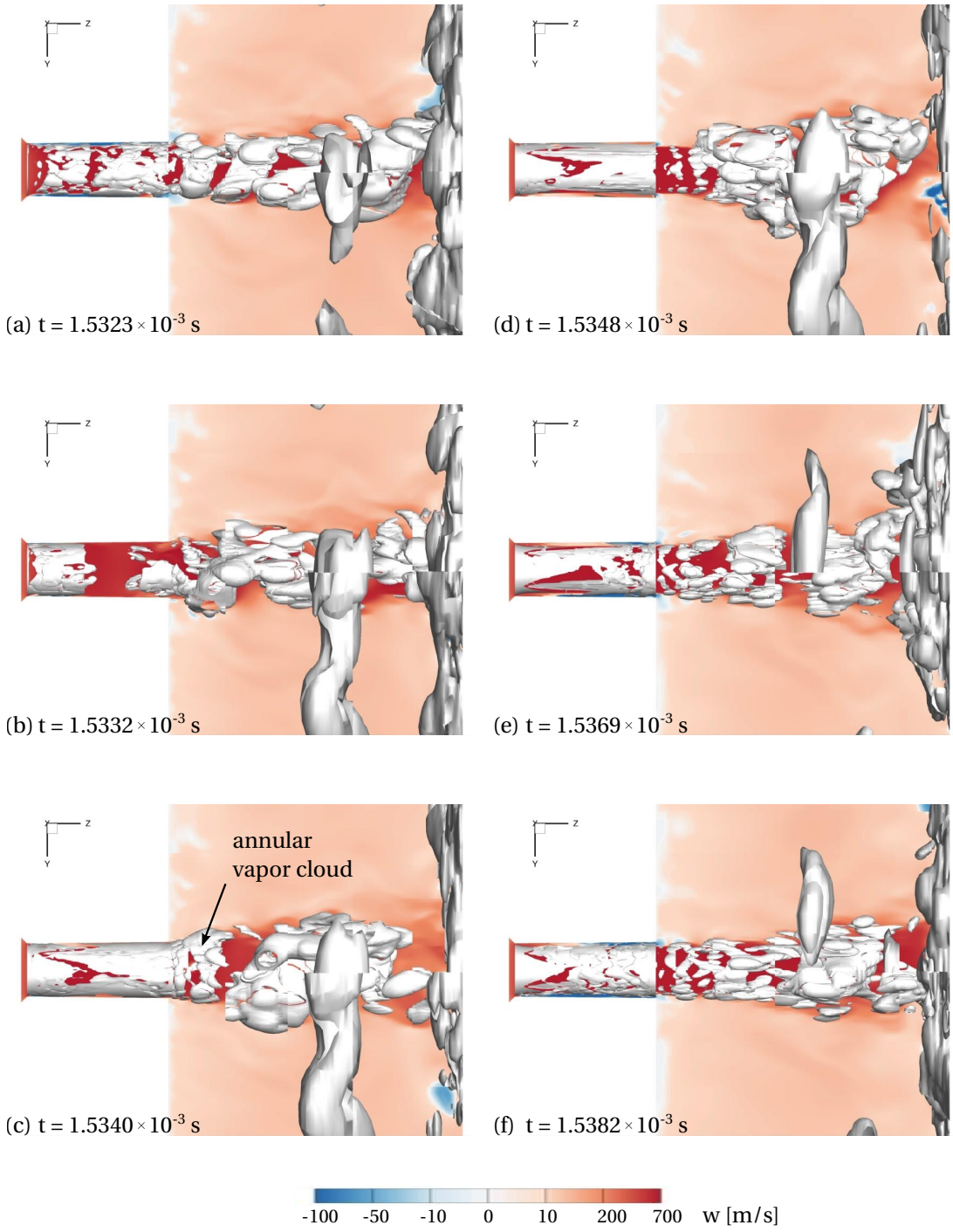

Figure 5.10: Representative snapshots during one shedding cycle in Design A. Time instants (a)-(f) are marked in Fig. 5.9a. Instantaneous velocity w shown at mid-plane together with iso-surfaces of vapor volume fraction $\alpha = 10\%$.

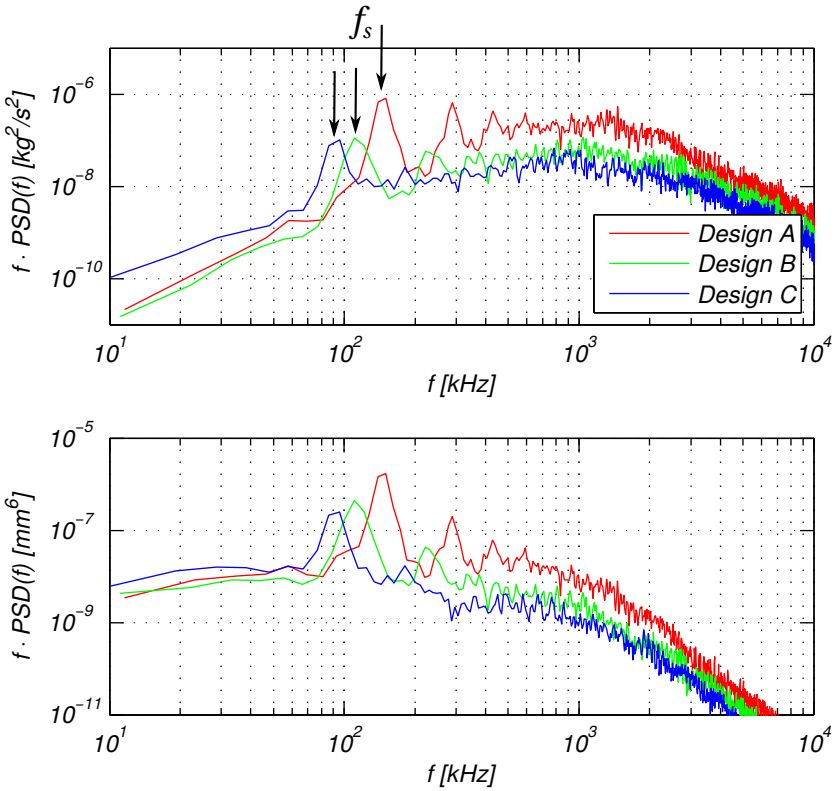

Figure 5.11: Pre-multiplied power spectral density of the mass flow rate at the throttle outlet (top) and vapor volume in the throttle(bottom).

where f_s is the shedding frequency, l_{max} is the maximal cavity length, which corresponds approximately to the discharge throttle length and v_c is the characteristic cavity velocity. For the characteristic cavity velocity, we choose the velocity of the re-entrant motion. Dular and Bachert [37] demonstrated the importance of choosing physically relevant values for the characteristic quantities when computing the Strouhal number in cavitating flows. An estimation of the re-entrant velocity is given by the space-time plot of the vapor volume fraction in Fig. 5.12. We extract the vapor volume fraction at the first near-wall cell for every finite volume along the throttle length and average it in the circumferential direction subsequently. Thus, a contour plot showing the temporal development of the spatially averaged vapor volume fraction in the vicinity of the throttle wall is generated. The plot enables straightforward assessment of the cavity restoration and decay rates. It confirms a periodic behavior of the flow. An increase in the cavity oscillation period from Designs A–C is visible as well. The plot demonstrates that the velocity of the re-entrant flow can be considered as nearly constant during the upstream propagation. Predicted St numbers based on the estimated re-entrant

velocity are reported in Table 5.3. Whereas the prediction of the shedding frequency and the cavity length is straightforward, uncertainty is introduced by estimation of the re-entrant flow velocity when the cavity cycle is more random, which is the case for Design C. In the open literature, St is commonly found in the range 0.22-0.4 for the periodic cavitation cloud shedding (Le et al. [68], Ganesh et al. [45]). However, physical phenomena observed here are distinct from the classic cloud shedding, commonly observed at hydrofoils, where the flow oscillations are governed by the re-entrant jet, whose thickness is typically an order of magnitude smaller than the cavity sheet. Moreover, large-scale clouds, which are periodically shed are not present in the investigated designs. Callenaere et al. [25] carried out a series of experiments of the cavity behind the backward-facing step in the divergent channel. The authors reported a different behavior between the thick cavities, which exhibit a classic cloud shedding and long, thin cavities. In the latter case, they observed a substantial interaction between the cavity interface and the re-entrant jet throughout its upstream movement. Furthermore, although the global oscillation period remained unaltered, a reduction of the re-entrant jet velocity and an increase in the jet development times, which occupied up to 2/3 of the complete cavity cycle, were reported. Similar cavity oscillations have been observed in the experimental and numerical study of a micro-sized submerged nozzle configuration by Duke et al. [36] as well. In the supercavitating flow regime at cavitation number very close to unity, the authors didn't observe a classic cloud shedding and a formation of the re-entrant jet, but some variation of this phenomenon which occurred over longer time scales. This trend in experimental observations suggests different mechanisms governing flow oscillations for thin cavities in the submerged environment and is in line with the results of the current study.

	Design A	Design B	Design C
f_s [kHz]	140-150	110	85-95
v_c [m/s]	120	80	70
St [-]	0.56-0.62	0.68	0.6-0.67

Table 5.3: Strouhal numbers St based on the estimated shedding frequency f_s, re-entrant flow velocity v_c and discharge throttle length.

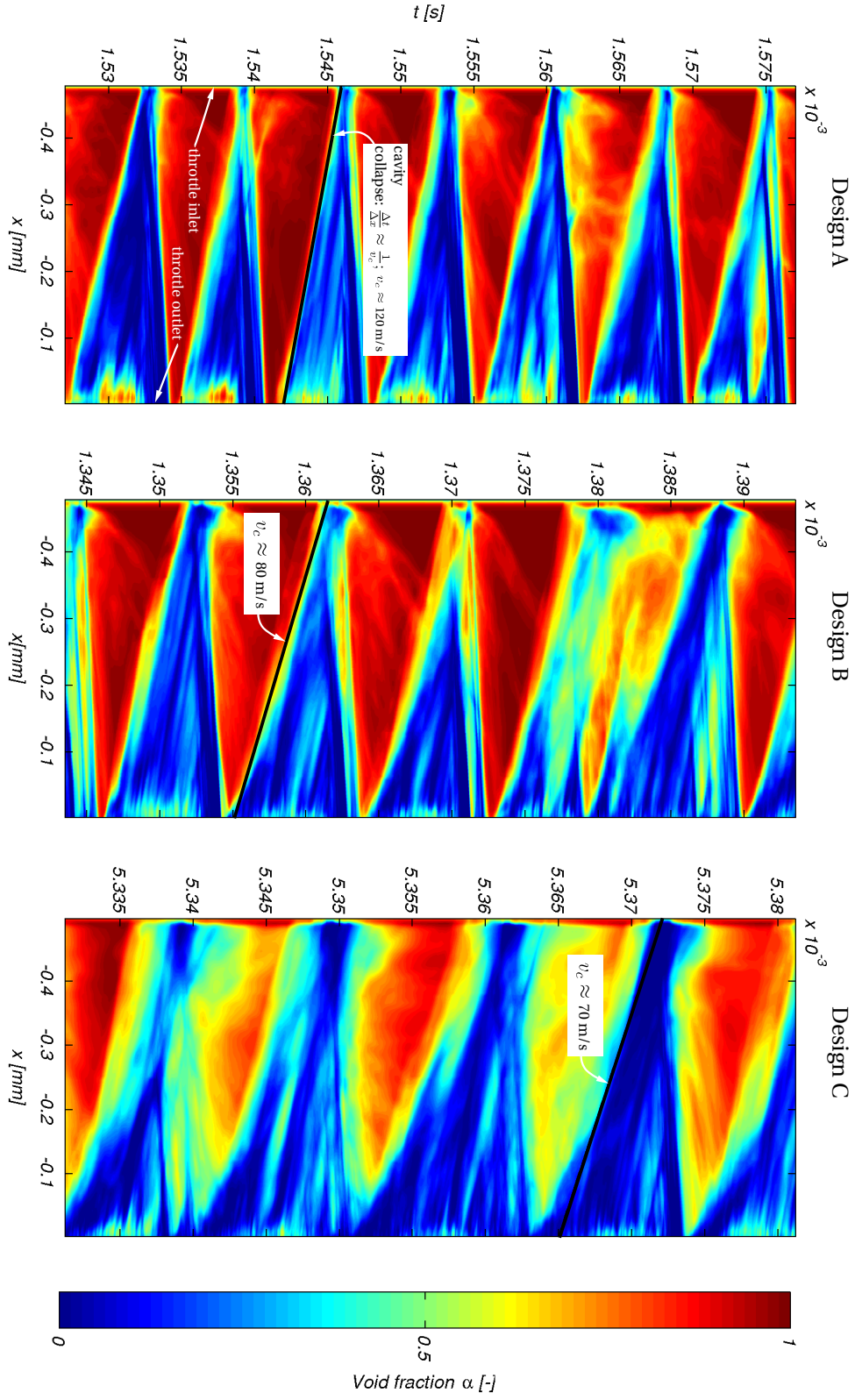

Figure 5.12: Space-time plot of the void fraction α in the vicinity of the throttle wall. The estimated velocities of the re-entrant motion are shown as well.

5.6 Erosion Assessment

The advection of vapor clouds into regions of increased pressure, as well as the re-entrant motion of the cavity inside the throttle, lead to the collapse of vapor structures and to the formation of shock waves. Our numerical scheme captures those shock fronts and thus enables an erosion assessment without additional modeling assumptions.

5.6.1 Wall Loads

Relating event strength to the integral quantity, such as temporal evolution of the vapor volume in the throttle, can provide information about the flow topology and time instants which can produce potentially violent wall loads. Figures 5.13a-5.13c show the integral vapor volume in the throttle together with the collapse pressure peaks during a time interval of 0.05 ms. In Design A, the most violent collapses (on the order of 1 GPa) are found during the final stages of the sheet collapse in the throttle, when the vapor volume reaches a local minimum. Pressure peaks are nearly periodically distributed and densely clustered around the time instants when the condensation of the cavity sheet takes place. This is not the case for Designs B and C. Here, generally speaking, events are more broadly distributed during the observed shedding cycles and the magnitude of pressure peaks is reduced as well. However, violent collapse pressures are recorded here as well (e.g. Fig. 5.13b, $t \approx 1.345$ ms.) A visual inspection of the collapse detector dataset on the example of Design A reveals that the highest pressure peaks are located not near the throttle intake, but in the second half of the throttle. During the sheet condensation, vorticity creates vapor fragments at the boundary between the core flow and the re-entrant flow. These vapor fragments either collapse near throttle walls, producing high surface loads, or are being washed out as a new cavity in the throttle develops. Figure 5.14 depicts a detailed sequence of the possible erosion mechanisms in the second half of the throttle. Disintegration of a small vapor fragment (labeled with *I*) in the vicinity of the throttle wall may leave footprints equal or higher than 0.2 GPa. The corresponding time scale of the collapse is ≈ 0.12 μs, which is approximately 2% of one complete shedding cycle ($T \approx 6.6$ μs). Condensation of a larger vapor cloud (labeled with *II*) occurs over the larger time scale ≈ 0.3 μs, and the associated wall loads are higher as well, reaching up to 0.7 GPa at this

time instant, which is five times higher than the imposed inlet pressure. Pressure peaks found in the vicinity of the throttle reach up to 0.2 GPa at the respective time instants. Koukouvinis et al. [66] reported a similar erosion mechanism acting on the nozzle walls in the submerged environment.

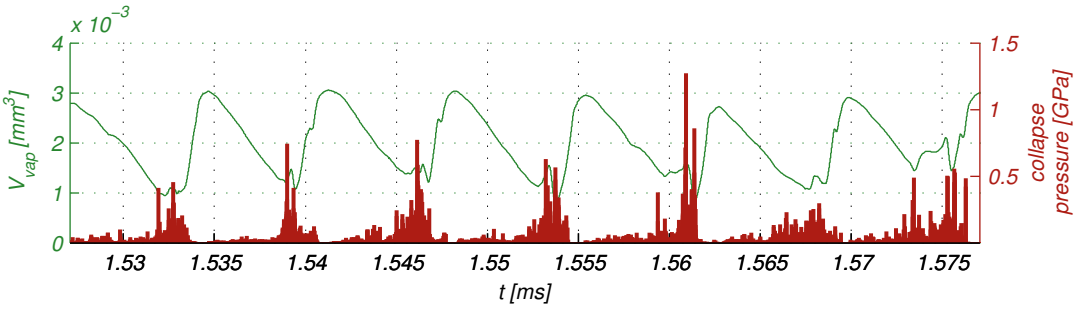

(a) Design A

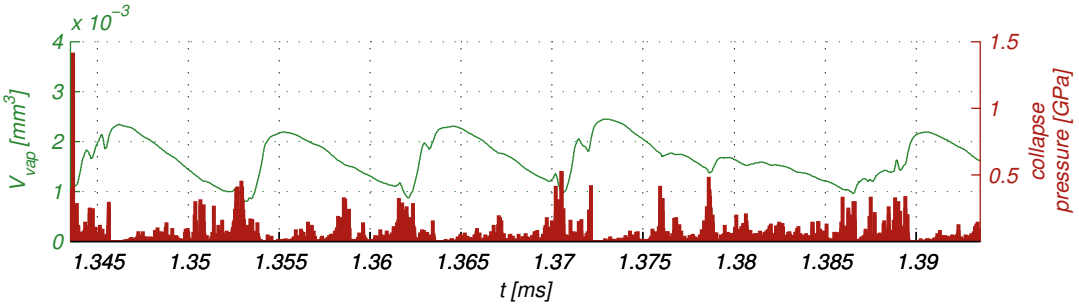

(b) Design B

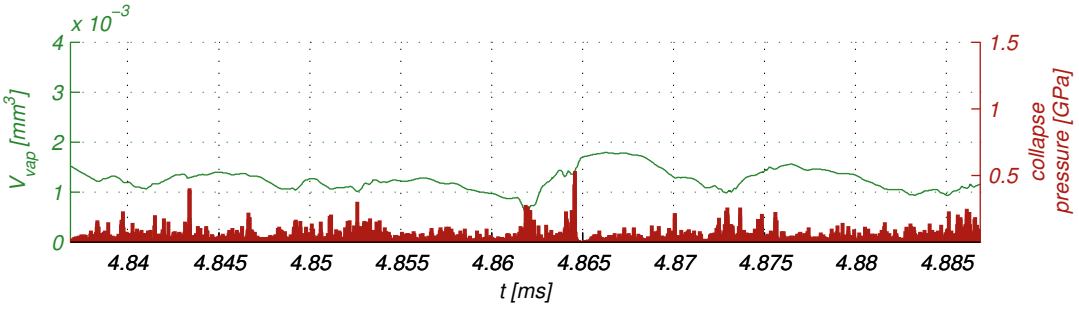

(c) Design C

Figure 5.13: Temporal evolution of the integrated vapor volume in the throttle (green curve) shown together with the recorded collapse pressure (red bars).

The observed wall loads during the analysis interval $\Delta t = 0.2$ ms are shown in Fig. 5.15. For visualization purposes, transformation of Cartesian to cylindrical coordinate system is performed. The horizontal axis represents the throttle circumference, computed as the arc

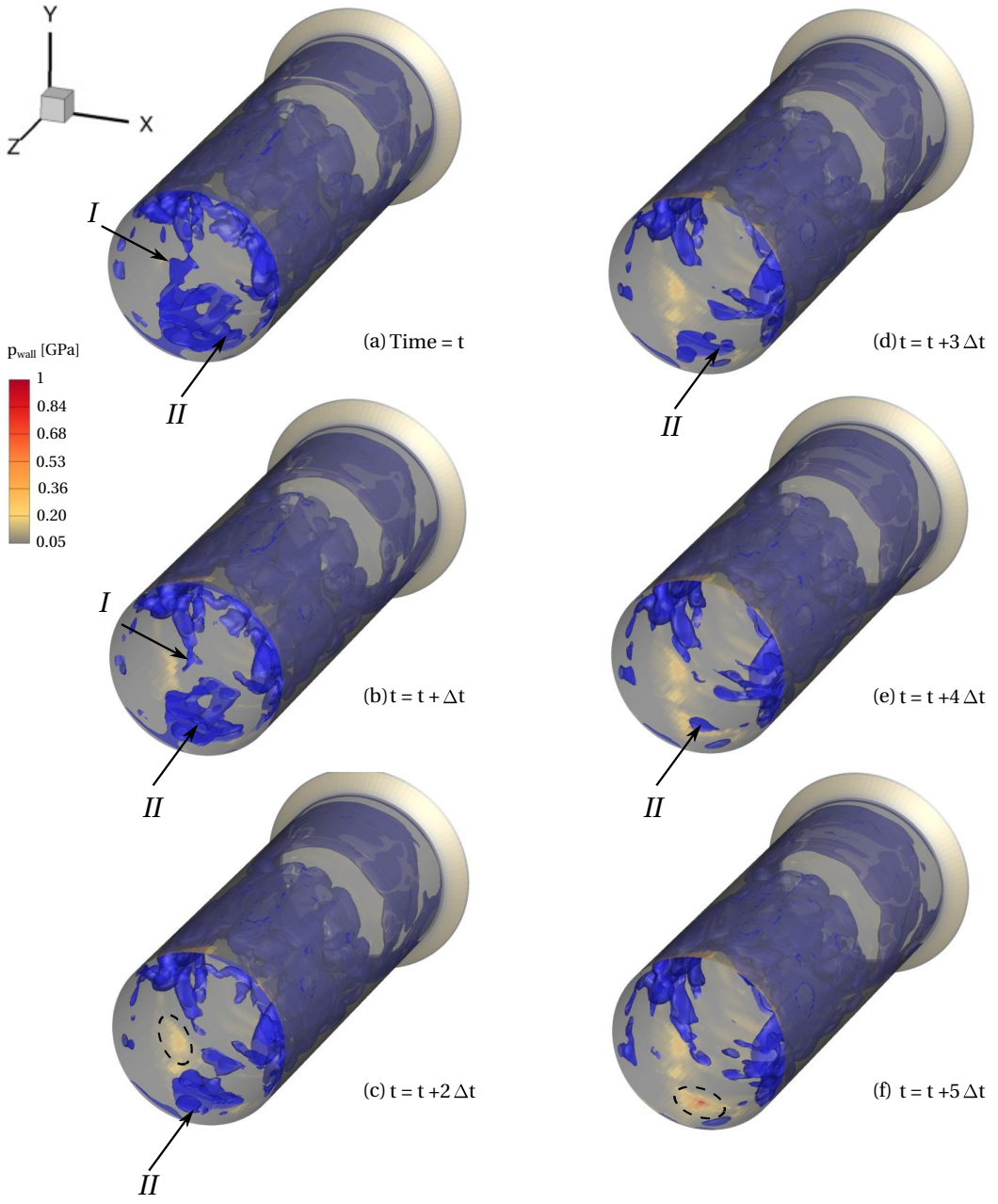

Figure 5.14: Instantaneous snapshots of vapor cloud collapse in the discharge throttle of Design A. Disintegration of two vapor fragments (labeled with *I* and *II*) at different positions in the throttle is depicted. Footprints of the maximal wall loads are shown together with iso-contours of $\alpha = 10\%$. Start time $t = 1.5389$ ms, $\Delta t \approx 66 \cdot 10^{-9}$ s.

length $s = \int_0^{2\pi} r d\phi$, and the vertical axis follows the longitudinal direction. This enables an unobstructed view of the throttle surface in each design. A significant difference between the investigated designs can be observed. The most aggressive flow with pressure peaks of 1 GPa

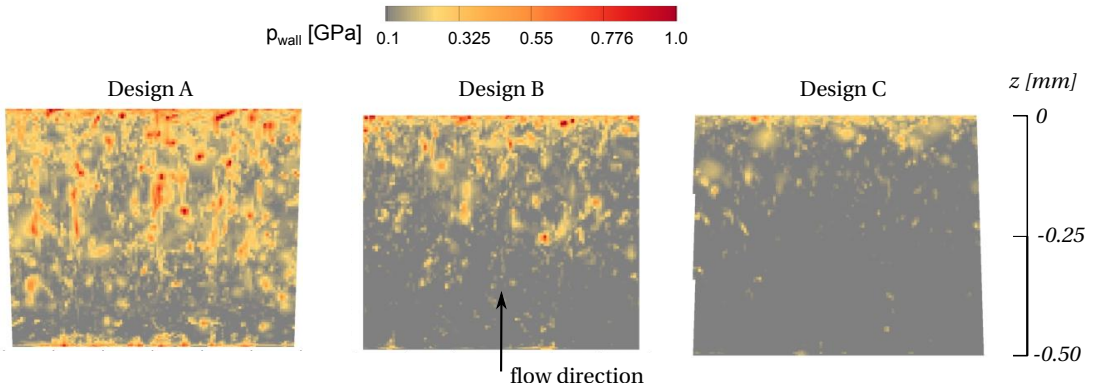

Figure 5.15: Distribution of the wall loads during the time interval $\Delta t = 0.2$ ms.

or higher is observed for Design A. Designs B and C show reduced maximal surface pressures. In the case of Design C, no pressure maxima higher than 0.2 GPa are found near the throttle intake. Here, erosion-prone sites may be found only in the vicinity of the throttle exit and a few peaks are observed in the second half of the throttle as well. If one compares the magnitude of the wall loads with the yield strength of the steel St 52 DI ($Re = 0.72$ GPa), which is commonly used for manufacturing common rail components such as a fuel delivery line [7], it is evident that cyclic implosions near material surfaces may cause stresses that can lead to the material strength reduction and fatigue.

5.6.2 Collapse Spectra

We further analyze the aggressiveness of the flow field by employing the collapse detection algorithm and generating statistical information about the magnitude and rate of collapse events. Mihatsch et al. [76] demonstrated the dependency of the collapse pressure on the spatial resolution applied. Therefore, we adopt the proposed scaling laws for the collapse pressure p_c and the rate of the collapse events N to compensate for the grid resolution effects as follows:

$$p_{scaled} = p_c \frac{V_\Omega^{1/3}}{l_{ref}}, \tag{5.3}$$

$$N_{scaled} = N\left(\frac{V_\Omega^{1/3}}{l_{ref}}\right)^\kappa . \tag{5.4}$$

Reference length l_{ref} is separately computed for each design by taking into account cell volumes V_Ω where condensation occurs, $l_{ref} = \langle V_\Omega^{1/3} \rangle$. We apply a calibrated value of $\kappa = 3/2$ as reported by Mihatsch et al. [76].

For a valid comparative analysis of different designs, assessment of the temporal convergence of the collapse spectra on the example of Design A is utilized. This assures that the computed collapse spectra are converged in respect to time, and minimizes computational effort needed for the statistical analysis of the flow. Figure 5.17 shows cumulative collapse rates in the whole domain and in the throttle at four different analysis intervals. We do not include collapse events occurring less than 5 times into the statistics. The analysis time of 0.05 ms corresponds to approximately 7 shedding cycles in Design A. We recognize that the slope of the curve in the semi-logarithmic diagram is already well represented after 0.05 ms and that a longer computation time solely captures violent events that occur less frequently. The same conclusion holds for the collapse spectra within the throttle. Therefore, we believe that 0.2 ms of physical time is sufficient for the quantitative comparison of different designs. This analysis interval covers approximately 28 cavity cycles in Design A, 22 cycles in Design B and 17 cycles in Design C, respectively. The cumulative collapse spectra in the whole domain and in the throttle, as given in Fig. 5.17, confirm a higher erosion risk for Designs A and B when compared to Design C. In Design C, the rate of collapse events is reduced not only in the throttle, but in the whole domain as well. On the other hand, Design B resembles Design A in the whole domain, but features a reduced flow aggressiveness in the throttle.

5.7 Summary

The present study applies a homogeneous mixture model for the simulation of the cavitating flow in the generic valve chamber of the Diesel common rail injection system. Thermodynamic closure is obtained by utilizing a barotropic equation of state for ISO 4113 test fuel. The utilized generic model resembles the flow features of the realistic valve chamber, but at the

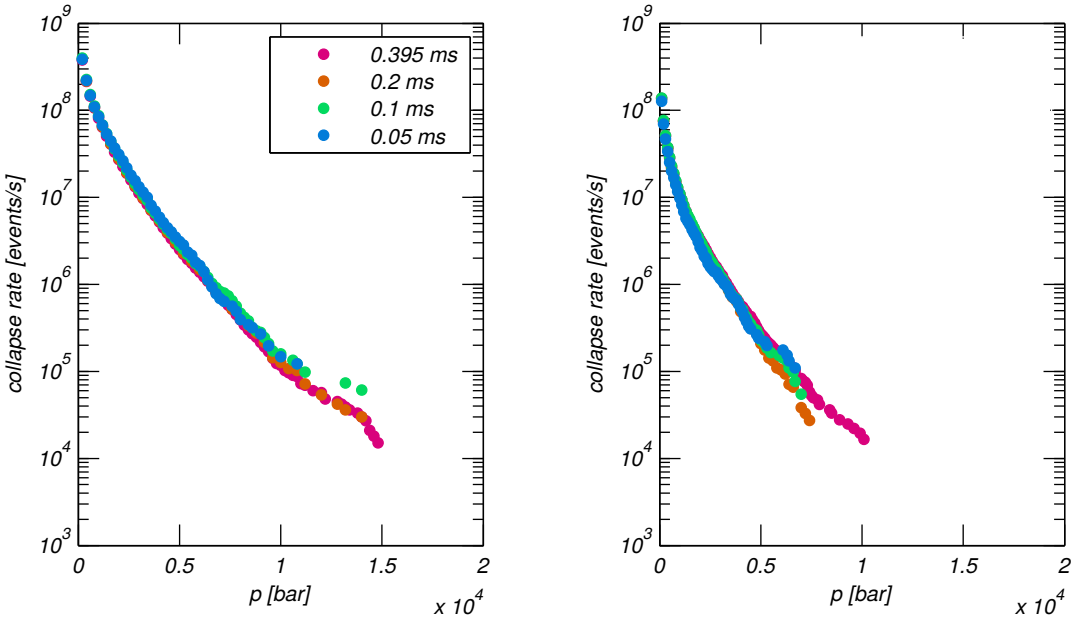

Figure 5.16: Convergence of cumulative collapse rates. Left: whole domain, Right: throttle

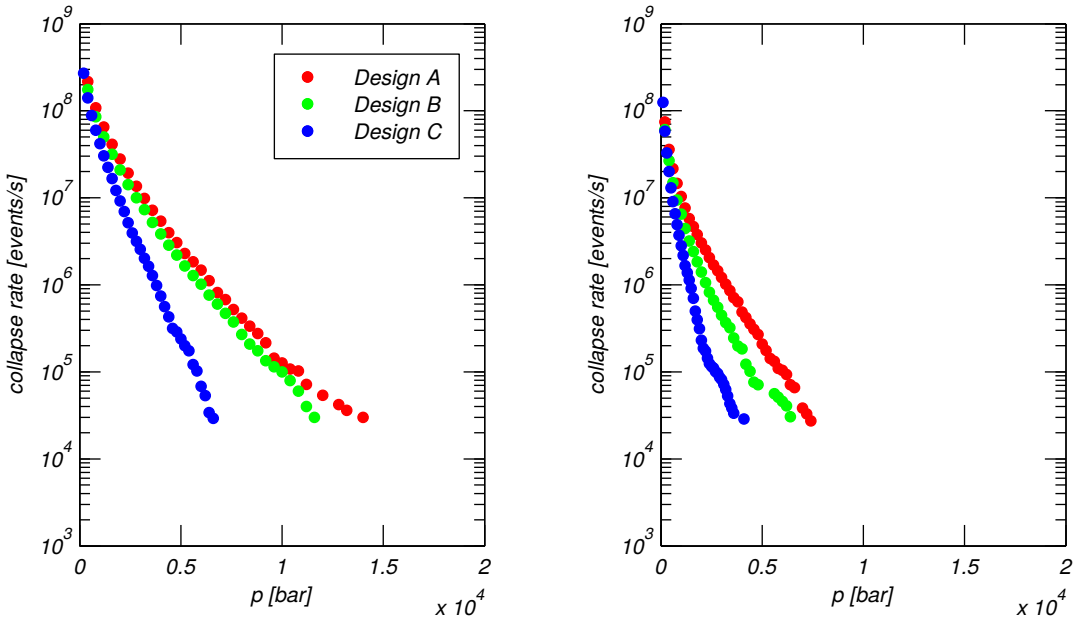

Figure 5.17: Cumulative collapse rates. Left: whole domain, Right: throttle

reduced computational effort instead. Although the chosen configuration is simplified, it demonstrates the complexity of the flow. We examine the instationary flow dynamics in three throttles with distinct geometric characteristics. For each design investigated, the flow in the throttle exhibits nearly periodic behavior. The highest shedding frequency is observed for

Design A, which features the negative conicity factor. A reduction of the shedding frequency is observed for Designs B and C. Strouhal numbers based on the estimated re-entrant flow velocity suggest that shedding behavior differs from the classic cloud shedding, which is usually observed at hydrofoils. We perform the erosion risk assessment by monitoring the instantaneous pressure peaks at the throttle walls together with iso-surfaces of vapor volume fraction. Erosion mechanisms responsible for the spots with high wall loads in the second half of the throttle are identified. The most aggressive flow is observed for Design A, with the wall loads reaching up to 1 GPa or higher in the vicinity of the throttle intake and along the throttle walls. Designs B and C show reduced aggressiveness, although the spots with high wall loads are observed as well.

6 Influence of the Step-hole Diameter on the Cavity Dynamics

In the following chapter, we investigate the flow in two valve chamber configurations that feature a step-hole mounted on the discharge throttle.

This section has been published in Beban et al. [15]. Reprinted with permission by Begell House.

6.1 Computational Setup

The geometry of the investigated designs is given in Chapter 4. The only difference between Design D and Design E is the diameter of the step-hole. The step-hole diameters are $D_D = 0.5$ mm (Design D) and $D_E = 1$ mm (Design E), respectively. The length of the step-hole is $L = 0.5$ mm and the distance from the step-hole outlet to the pilot valve front is 1 mm. The dimensions of the throttle are $l = 0.5$ mm and $d = 0.2$ mm, respectively.

On the *Level 1* grid, the numerical domain is discretized with $0.8 \cdot 10^6$ hexahedral cells. The *Level 2* grid comprises approximately $4.6 \cdot 10^6$ cells (Design D) and $5.0 \cdot 10^6$ cells (Design E), respectively. The applied computational grids at the *Level 2* grid are shown in Fig. 6.1. In order to achieve sufficient resolution of the cavitating sheet inside the throttle, computational cells are refined in wall normal direction, leading to a minimum cell height of approximately 1 μm in the vicinity of the throttle wall. On the fine grid level, the flow domain within the discharge throttle is resolved by 84 cells along its length and by 76 cells across the diameter. The small cell sizes coupled with the speed of sound of approximately 2000 m/s lead to a time-step size

of $\tau \approx 1.5 \cdot 10^{-10}$ s .

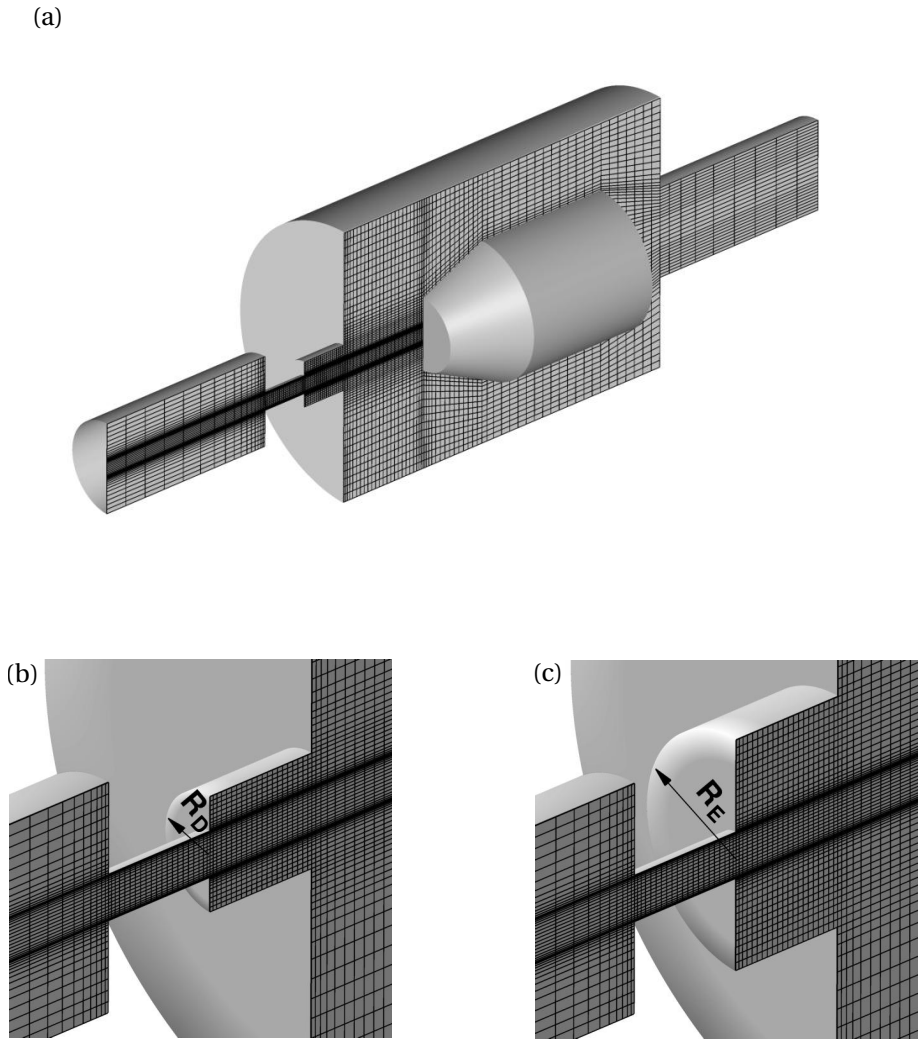

Figure 6.1: Computational grid: (a) isometric view of the entire domain on the example of Design D (b) and (c) details of the fine grid in the throttle and step-hole region of Design D and Design E. Every fourth grid line is shown.

We examine the same operating point for both designs. At the inlet, we prescribe a static pressure p_{in} of 2000 bar. The static pressure p_{out} at the outlet is fixed to 60 bar. This corresponds to the cavitation number $\sigma = (p_{in} - p_{vap})/(p_{in} - p_{out}) = 1.03$. All remaining quantities at inlet and outlet surfaces are extrapolated from the domain interior. Solid boundaries are treated as inviscid adiabatic walls. The whole domain is initialized with a liquid at rest at pressure $p = p_{out}$.

6.2 Results

In the following, we present computational results obtained on the *Level 2* grid. First, we give a general description of the flow field and compare discharge coefficients with the theoretically predicted value. Then, a detailed assessment of the flow dynamics for designs D and E is given.

We focus on the shedding mechanism in the throttle and its influence on the unsteady production of vapor clouds in the step-hole, which can be directly related to the occurence of high pressure peaks. In both designs cavitation is generated at the sharp throttle intake. We observe a sheet cavity attached to the throttle wall that extends to the throttle exit. This regime is also known as supercavitation. Most of the fluid acceleration occurs at the inlet section, generating a high-speed liquid jet in the throttle that is separated by the vapor film from the walls. As the liquid jet exits from the throttle, mixing with the ambient fluid in the chamber occurs. This generates low pressure vortex cores on the jet periphery which can act as cavitation sites. Cavities that form in the shear layer are advected towards the pilot valve front, where they finally collapse. The advection of the cavities undergoes complex processes of vortex interaction, resulting in vapor clouds of various shapes. We compute the discharge coefficient using Eq. 5.1 and compare it with the theoretical value. Both designs have the same numerically predicted discharge coefficient $C_d = 0.6$, due to identical geometric properties of the throttle. For circular, sharp-edged orifices, Nurick [80] computes $C_d = C_c\sqrt{\sigma}$. In the available literature, the contraction coefficient C_c is estimated to $C_c \approx 0.61 - 0.62$ [71, 80]. A more accurate empirical estimation of the contraction coefficient, which considers the ratio of the throttle cross-section to the inlet channel cross-section, reads [29]: $C_c = 0.62 + 0.38(A_{th}/A_{in})^3$. The contribution of the second term can be neglected for large area ratios, which is the case for investigated designs. Using $C_c = 0.62$ and $\sigma = 1.03$, the discharge coefficient predicted by Nurick's relation gives an approximately 4.8% larger value than the one obtained from our simulations. The theoretical estimate of the contraction coefficient assumes a non-cavitating flow in the nozzle [54], which does not hold for the investigated operating point. Therefore, we do not expect that a complex, three-dimensional flow field perfectly follows a one-dimensional model, which rather offers a simple and fast estimate in the absence of experimental data.

6.2.1 Instantaneous Flow Field

Design D

Figure 6.2 shows the mass flow rate at the throttle exit and the integrated vapor volume in the throttle during a time period of $3 \cdot 10^{-5}$ s, as observed for Design D. The quasi-periodic increase and decay of the vapor volume is guided by significant oscillations of the mass flow rate of up to ±30%, indicating the shedding mechanism in the throttle.

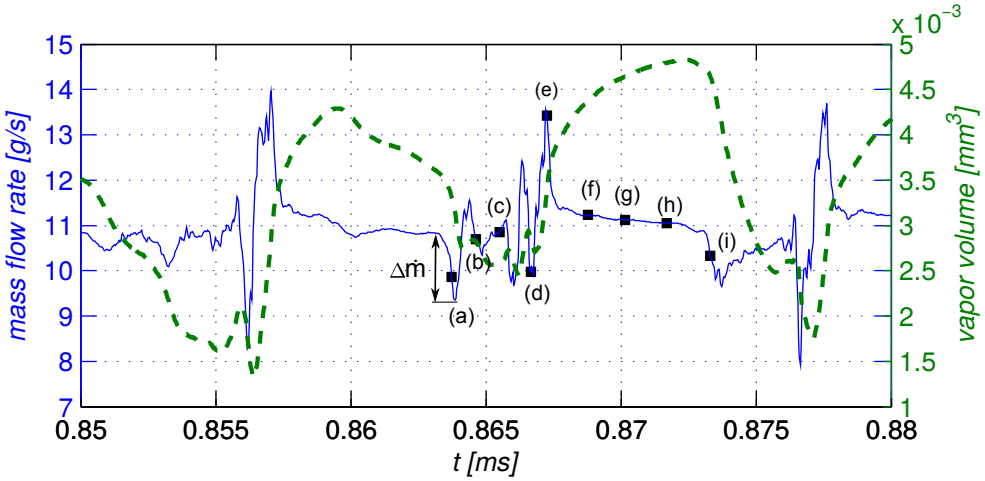

Figure 6.2: Temporal evolution of the mass flow rate at the throttle exit (solid blue curve) and vapor volume in the throttle (dashed green curve) for Design D.

In Fig. 6.2 we analyze the flow field at nine representative instants in time, which are marked in Fig. 6.3 with letters (a)-(i). Snapshots are selected in order to illustrate the typical development of vapor structures during one shedding cycle and time intervals between time instants are not necessarily equidistant. All pictures show iso-surfaces of the vapor volume fraction $\alpha = 10\%$ (grey structures) together with the contours of the axial velocity component plotted at the mid-plane of the domain. The maximum velocity of the discharging liquid jet reaches approximately 680 m/s. At the front side of the pilot valve, the jet decelerates and a high pressure stagnation region develops.

At (a), a reverse flow close to the throttle wall leads to the onset of the collapse of the cavitating sheet (CS). We observe two types of reverse flow: a re-entrant jet and a bubbly shock (see Fig. 6.4). The structure of the upstream propagating re-entrant jet differs from those observed

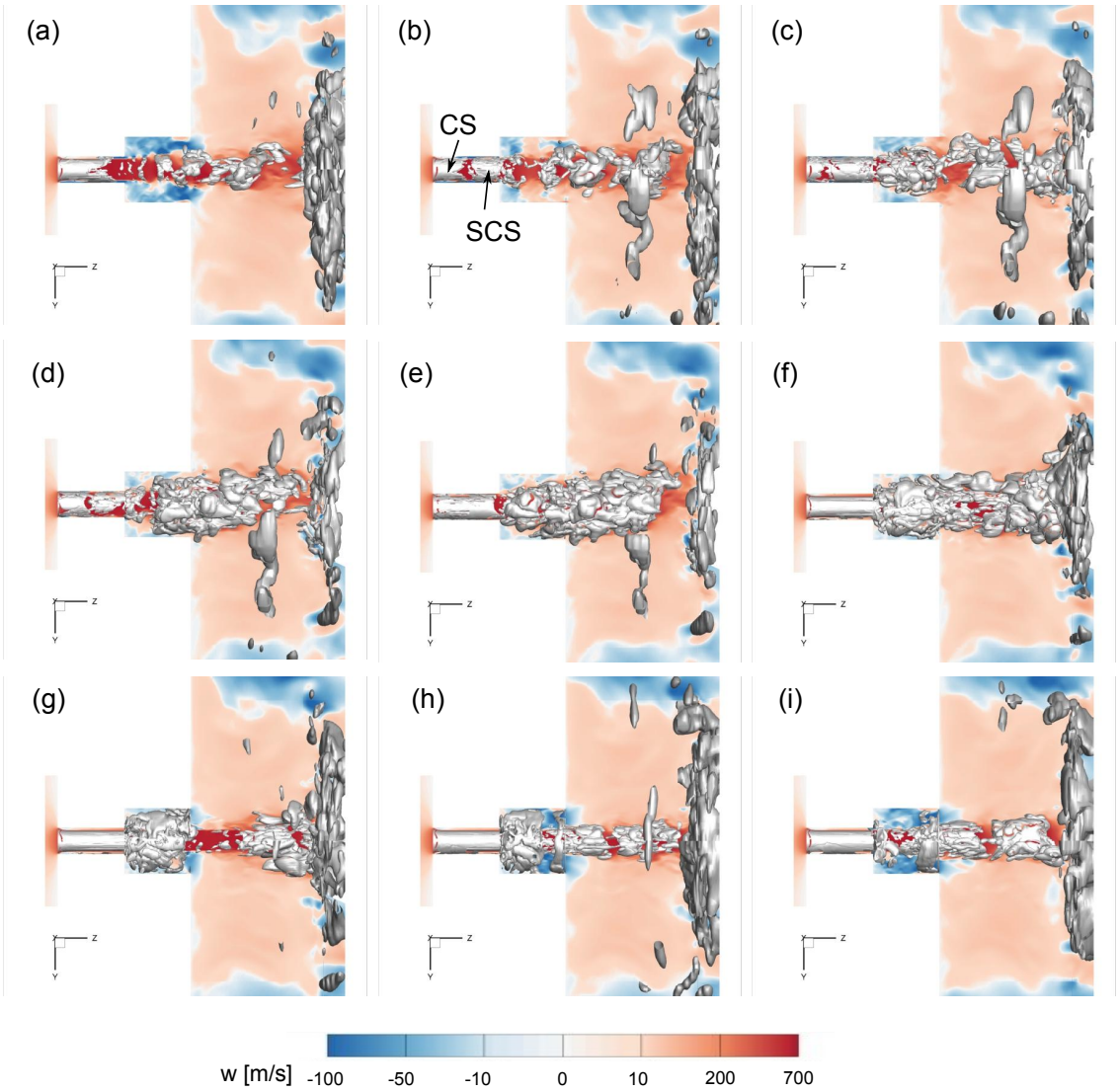

Figure 6.3: Representative snapshots during one shedding cycle of Design D. Time instants (a)-(i) are marked in Fig. 6.2. Instantaneous streamwise velocity shown at mid-plane together with iso-surfaces of vapor volume fraction $\alpha = 10\%$, $\Delta t_{(a)-(i)} = 9.6 \cdot 10^{-6}$ s.

at, e.g. large-scale hydrofoils, where the re-entrant jet thickness is significantly smaller than the thickness of the cavity [68]. In this particular case, the thickness of the re-entrant jet covers at some time instants nearly a half of the normal extent of the cavity. Moreover, the re-entrant jet is multimodal in circumferential direction, leading to multiple break-up positions of the sheet. Callenaere et al. [25] observed similar phenomena for very thin cavities. Additionally, the formation of a bubbly shock forces the cavity sheet to completely collapse. The propagation velocity of its front reaches approximately 200 m/s (see Fig. 6.5), which is

by orders in magnitude larger than the local sound of speed within the cavity. However, at some shedding cycles the re-entrant jet is completely absent, and the cavity sheet is affected by the bubbly shock only. There is a significant amount of shear between the liquid core and the reverse flow, causing a formation of vortices due to Kelvin-Helmholtz instability. The pressure in these vortex cores drops below the saturation pressure and new cavity pockets form downstream of the sheet. These pockets coalesce and form a secondary cavitating sheet (SCS) in the throttle (b). At (c), the bubbly shock almost reaches the throttle inlet while vapor clouds in the step-hole grow further. Between snapshots (c) and (d) the integral vapor volume in the throttle reaches its minimum value. However, vapor is continuously present in the throttle – it either originates from the development of a new cavitating sheet or from vortex cavitation during the upstream propagation of the reverse flow. Between time instants (d) and (e) the mass flow oscillates severely as the vapor pockets leave the throttle and the new cavity restores. The growth of the new sheet is accompanied by the change of the velocity sign in the proximity of the throttle wall and by a significant increase in the vapor volume in the throttle as well (e). We also observe that cavity restoration time occupies approximately one sixth of the whole shedding cycle. After the cavity restores, the mass flow rate stabilizes (f). At the same time, we observe a vapor pattern that occupies almost the entire step-hole volume. Since the imposed pressure in the valve chamber exerts a force on the vapor cloud in the step-hole, it starts to condense. The onset of the cloud collapse is depicted in (g). The axial velocity changes its sign at the step-hole exit, as the fluid originating from the chamber starts to fill it. A vapor ring is generated at the sharp step-hole exit (h) as well. At (i), the last fragments of the vapor pattern within the step-hole are shown just before their final collapse. The inertia of the liquid due to vapor collapse initiates a reverse flow in the throttle and the shedding cycle starts anew. Although the previously described dynamics can be rated as being quasi-periodic, a stochastic behavior is observed as well. Intermittently, the cycle does not lead to a filling of the entire step-hole volume with vapor and thus, irregular shedding processes occur.

Another mechanism that affects the mass flow and the cavity dynamics is presented in Fig. 6.6 (a)-(c). The collective collapse of the vapor pattern in the step-hole results in a compression wave which travels upstream into the throttle. Thereby, the axial velocity as well as the mass flow at the exit of the throttle are decreased. In contrast to the reverse flow, which is localized

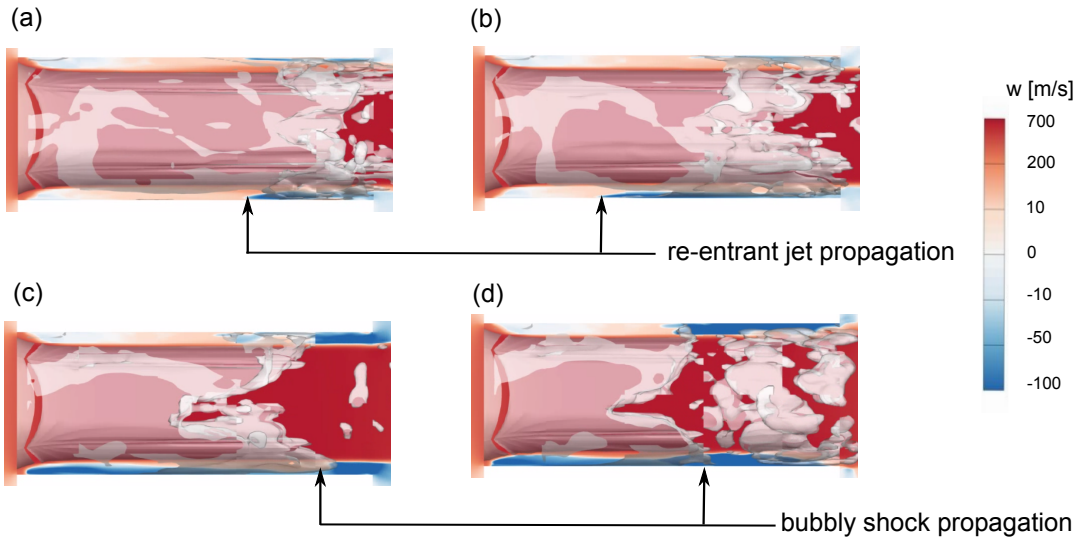

Figure 6.4: Representative snapshots depicting simultaneous development of the re-entrant jet and the bubbly shock in the throttle of Design D. (a)-(b) Propagation of the re-entrant jet on the lower throttle side, followed by the consecutive development of the bubbly shock (c)-(d). Instantaneous streamwise velocity shown at mid-plane together with iso-surfaces of vapor volume fraction $\alpha = 10\%$.

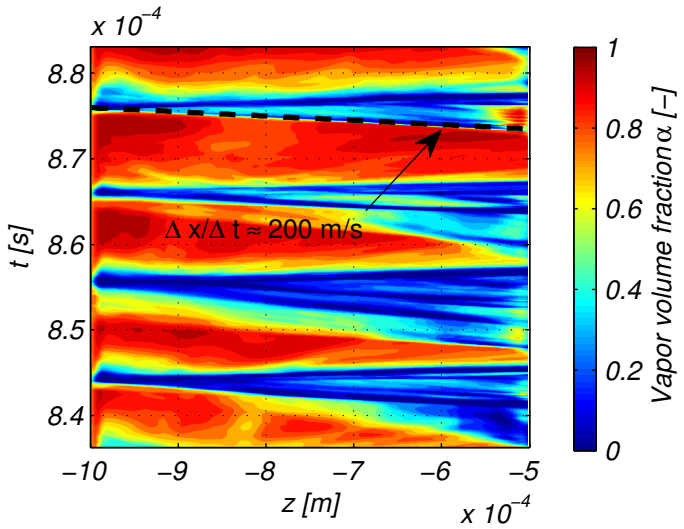

Figure 6.5: Estimation of the propagation velocity of the bubbly shock based on the vapor volume fraction contour plot. For each cell along the throttle wall, vapor volume fraction is averaged in the circumferential direction. The horizontal axis represents position and the vertical axis time. A dashed line on the diagram depicts a coherent collapse of the cavity sheet in the throttle for the case where reverse flow is dominated by the bubbly shock only. Velocity of the front is estimated to approximately 200 m/s.

close to the walls of the throttle, the pressure wave affects the flow over the entire cross-section.

The resulting decrease of discharge is indicated in Fig. 6.2 at approximately $t = 0.863$ ms. In the following, we apply linear wave theory to relate pressure and velocity jumps across the compression wave and provide further analysis of the interaction of the wave with the surrounding flow field. The pressure upstream of the wave is close to saturation pressure, while it reaches about 550 bar directly downstream of the wave. The resulting jump in axial velocity can be estimated as

$$\Delta u = \frac{\Delta p}{\rho c} \tag{6.1}$$

where ρc denotes the pre-shock acoustic impedance of the fluid. By using a value of $c = 1140$ m/s for the speed of sound to and $\rho \approx 800$ kg/m^3 for the density of the liquid, we predict a deceleration of the liquid jet velocity of $\Delta u \approx -60$ m/s.

By accounting for an increase of the density, the estimated reduction of the mass flow rate due to the compression wave is approximately $\Delta \dot{m} \approx -1$ g/s. However, as visible in Fig. 6.2, the actual drop in mass flow is even higher. This is probably due to the additional compression and acceleration of the pre-existing reverse flow. As the pressure wave reaches the cavity interface, it mainly reflects as a rarefaction wave while the velocity at the throttle outlet starts to recover.

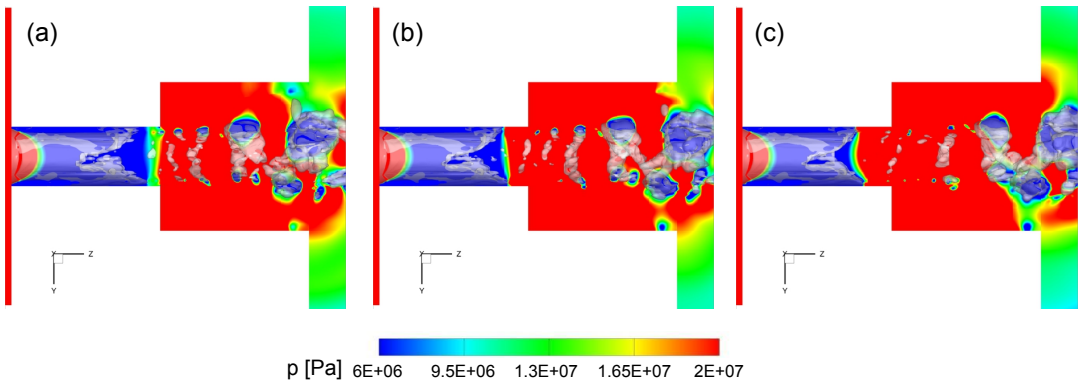

Figure 6.6: Propagation of the pressure wave front in the throttle of Design D. Instantaneous pressure at the mid-plane, two-phase regions identified by the iso-surfaces of vapor volume fraction $\alpha = 10\%$, $\Delta t_{frame} = 2.2 \cdot 10^{-7}$ s.

Design E

In the following, the cavity dynamics as observed for Design E are discussed. The only difference between Designs D and E is the diameter of the step-hole, being twice as large for Design E. The cavity dynamics within the throttle and downstream of the step-hole closely resemble those observed for Design D. However, a significantly altered behavior is found in the step-hole. Analyzing the flow in Design E we never observed the formation of a large vapor pocket in the step-hole. Therefore, coherent and violent collapses of such a vapor structure, as discussed above, do not occur. A representative flow sequence is shown in Fig. 6.7, depicting iso-surfaces of the vapor volume fraction $\alpha = 10$ % together with the static pressure at mid-plane. Note also that two slices through the vapor cloud are depicted, showing the cavitation-free liquid core of the high-speed jet. At (a), we observe a ring-shaped vapor cloud in the jet periphery that is about to collapse. At (b), isolated vapor patterns collapse, accompanied with the formation of shock waves. These waves propagate through the step (c), are reflected from walls and finally reach the throttle exit (d). Although this collapse-induced shock development leads to an analogous situation as found for Design D, its effect on the flow field within the throttle is found to be weaker than in the previous case. By visual examination of 1500 consecutive time frames ($\Delta t_{frame} \approx 3.14 \cdot 10^{-8}$ s), we observe that the collapse of the ring-shaped vapor cloud usually takes place at the second half of the step-hole. However, intermittently, there are almost no, or very weak shock fronts that reach the throttle, leading to a more random behavior of the jet.

In both simulated cases, the discharging of the liquid jet into the valve chamber occurs in a pulsating fashion. We identify two separate mechanisms that govern the flow oscillations: the development of the cavitating sheet in the throttle with the subsequent reverse flow formation and the collapse of the toroidal-shaped vapor clouds near the step-hole exit.

Frequency Spectra

In the following, we examine the frequency spectra of characteristic flow quantities. The spectra are estimated using the *pwelch* algorithm implemented in the MATLAB software package. Power spectral densities are computed by applying the Hanning window to six

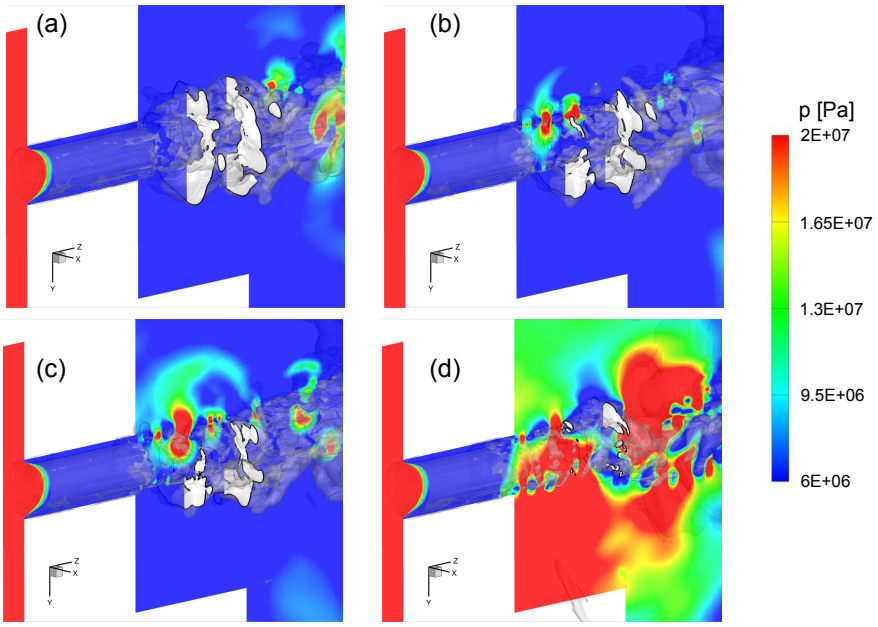

Figure 6.7: Representative snapshots depicting the collapse of the toroidal vapor cloud in the step-hole of Design E. Instantaneous pressure at mid-plane together with iso-surfaces of vapor volume fraction $\alpha = 10\%$, $\Delta t_{(a)-(d)} = 2 \cdot 10^{-6}$ s. Two slices at xy-plane depict the cavitation-free liquid core of the high-speed jet.

segments of input data with an overlap of 50%. The full signal covers a time interval of 0.41 ms. Figure 6.8 shows the spectra of the mass flow rate at the throttle outlet and the integrated vapor volume in the throttle. For both designs we identify the first dominant mode as the shedding frequency by visual inspection of the 1500 consecutive snapshots, which is $f_{1D} \approx 97$ kHz (Design D) and $f_{1E} \approx 107$ kHz (Design E). Higher harmonics of the shedding frequency and broadband noise due to collapses of vapor clouds are observed in the spectra as well. In the spectra obtained for Design E, we observe an excitation at approximately $f_{2E} \approx 150$ kHz. This excitation is related to collapse-induced pressure waves of vapor clouds in the step-hole, since f_{2E} is also found as the dominant frequency in the spectrum of a pressure probe located at the throttle exit along the axial direction.

6.2.2 Erosion Assessment

The violent nature of propagating shock waves is shown in Fig. 6.9, using the example of Design D. The collapse sequence of a vapor cloud within the step-hole has previously been shown in Fig. 6.3. The time interval between consecutive snapshots in Fig. 6.9 is $\Delta t_{frame} = 6.3 \cdot 10^{-8}$ s ,

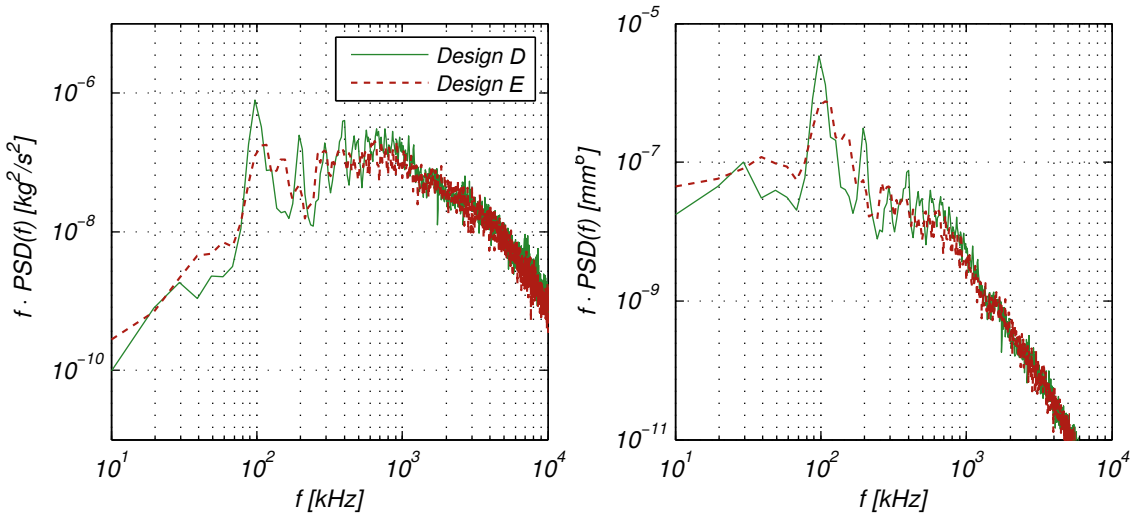

Figure 6.8: Premultiplied power spectral density of the mass flow rate (left) and vapor volume (right).

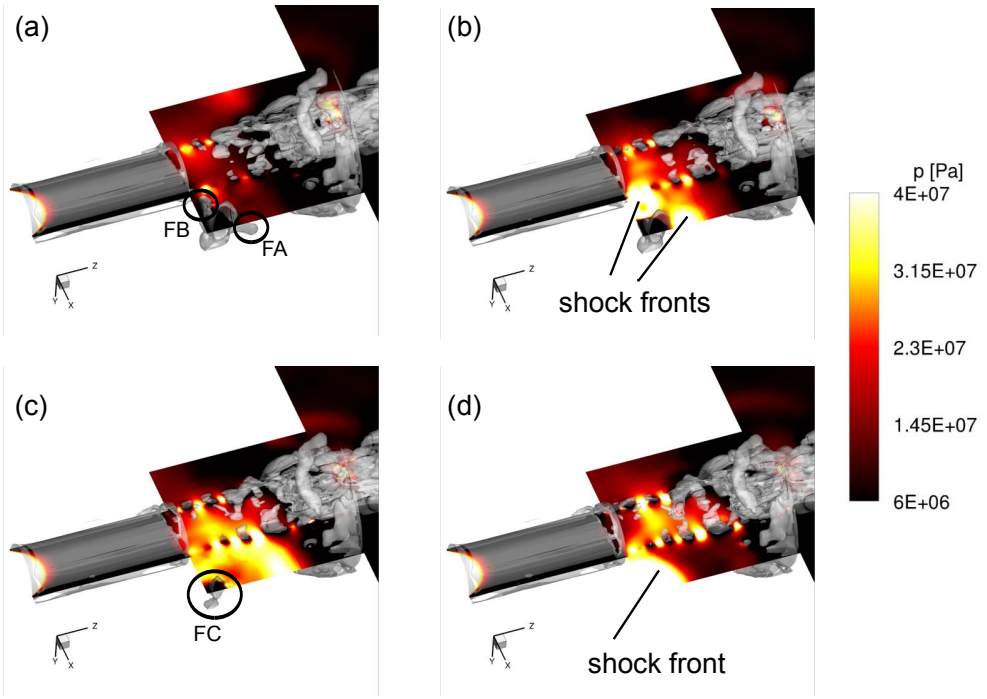

Figure 6.9: Visualization of the cloud fragmentation and propagation of the shock fronts in the step-hole. Instantaneous static pressure at mid-plane and iso-surfaces of vapor volume fraction $\alpha = 10\%$, $\Delta t_{frame} = 6.3 \cdot 10^{-8}$ s.

which emphasizes the small time scale of shock propagation. During the shrinking of the vapor cloud inside the step-hole, a series of implosions of smaller vapor fragments with different intensities are observed instead of a single, focused collapse. The fragments are marked with

FA, *FB*, and *FC* and visualized by iso-surfaces of the vapor volume fraction $\alpha = 10\%$. Snapshot (a) illustrates the fragmentation of the vapor cloud into pockets *FA* and *FB*. Snapshot (b) depicts a simultaneous development of shock fronts. At the very last stage (c), there is only one vapor fragment left. The propagation of shock following its collapse is depicted in (d). In the corner of the step-hole collapse focusing takes place, leading to maximum peak values of up to 5000 bar, which is approximately 80 times higher than the imposed outlet pressure. Such violent collapse events can create sites of cavitation erosion.

However, for a detailed erosion assessment, more quantitative information about the collapses, including their location, strength and number density is essential. For this purpose, we employ the collapse detection algorithm [76]. Figure 6.10 shows collapse events detected during a physical time interval of 0.044 ms (approximately 4 shedding cycles) for Design D and Design E, respectively. Each event is represented by a sphere whose size and color is proportional to the strength of the event. The majority of collapse events, including the strongest ones, take place in the step-hole and in the proximity of the pilot valve front. In Design D, we observe high-intensity events near the walls of the step-hole. For both designs weaker events are found in the throttle and in the chamber between the step-hole outlet and the pilot valve front. However, the most violent peaks are detected close to the walls of the step-hole in Design D.

Relating event strength and its temporal occurrence to integral quantities, such as vapor volume over time, provides information about the flow topology which can produce potentially aggressive vapor clouds. The integrated vapor volume within the throttle and the step-hole, together with the collapse pressure during a time interval of 0.04 ms is shown in Fig. 6.11. In Design D, the most violent collapses, higher than 1 GPa, occur during the final stages of the cloud collapse in the step-hole, when the vapor volume reaches a local minimum. One indicative time instant can be found in the diagram at approximately $t = 0.875$ ms. Visual inspection of the corresponding flow field reveals that those time instants correlate with an upstream traveling shock wave in the throttle and reductions in the mass flow rate. In Design E, weaker events are detected, and the frequency of the most violent events seems to be reduced, at least during the analyzed time span. The integrated vapor volume depicts essentially evaporation and condensation of vapor clouds in the case of Design D, as clouds collapse mostly in the step-hole. However, for Design E, the reduction of the integrated vapor volume

corresponds predominantly to the advection of clouds away from the step-hole. Therefore, the integrated vapor volume curve and the pressure peaks are not directly related for this design.

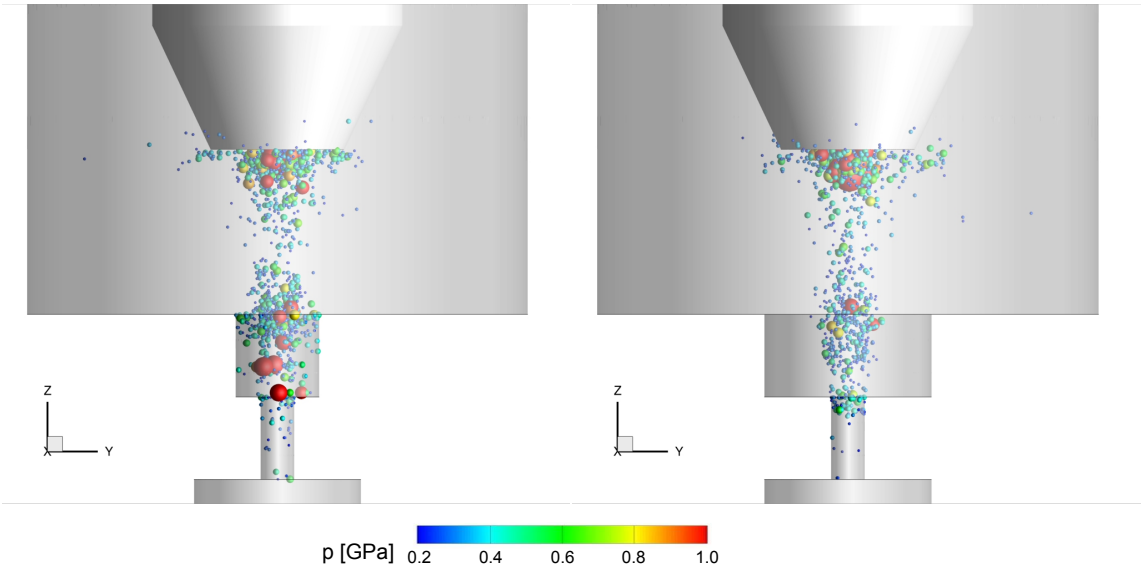

Figure 6.10: Detected collapse events in Design D (left) and Design E (right). Each event is depicted by the sphere whose size and color scales with the collapse pressure. Collapses with intensity less than 0.2 GPa are not shown.

In addition, we assess the flow aggressiveness by recording the maximum wall pressure for each computational cell during the simulation. Figure 6.13 shows “footprints” of the accumulated maximum pressure criterion during 0.2 ms, which corresponds to approximately 20 cavity cycles. For both designs, an increase in the wall pressure is observed within the second half of the throttle. At the walls of the step-hole of Design D, spots with particularly high wall pressures are detected. They correspond to the locations where a focused cavity collapse appeared. The highest observed peak with an intensity up to 3.7 GPa is found at the back plane of the step-hole. In contrast, step-hole walls of Design E remain almost unaffected. The fractions of the throttle and step-hole area, covered by pressure maxima of a certain strength are shown in Fig. 6.13. Within the throttle, areas of intense loads are basically identical for both designs.

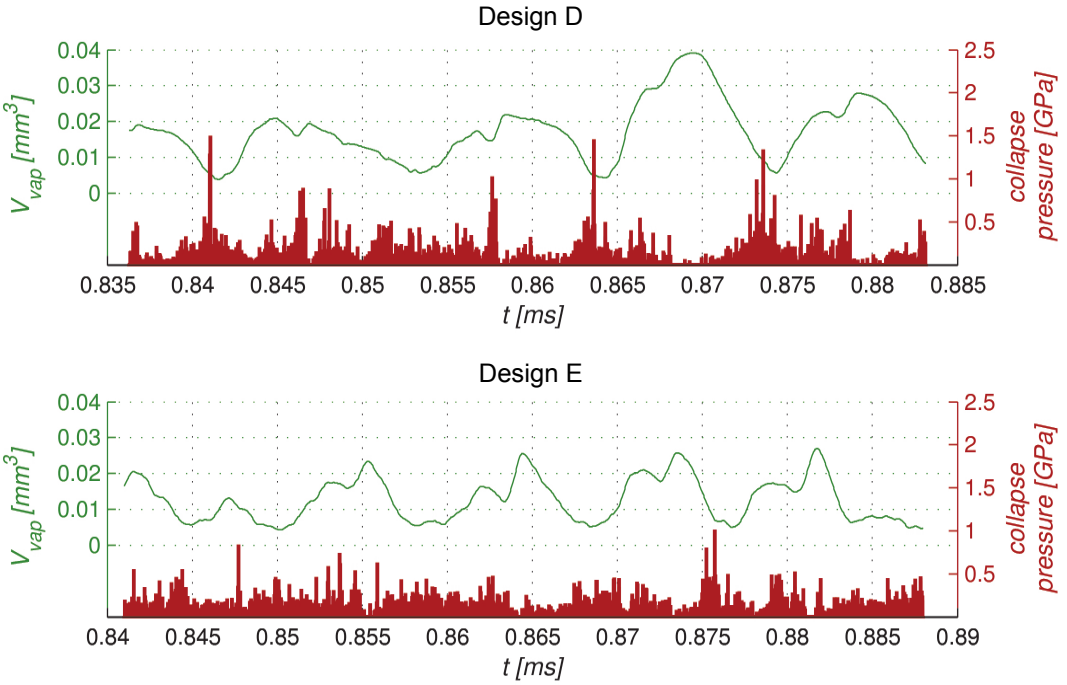

Figure 6.11: Temporal evolution of the integrated vapor volume in the throttle and step-hole V_{vap} (green curve) shown together with the recorded collapse pressure (red bars) for Design D and Design E.

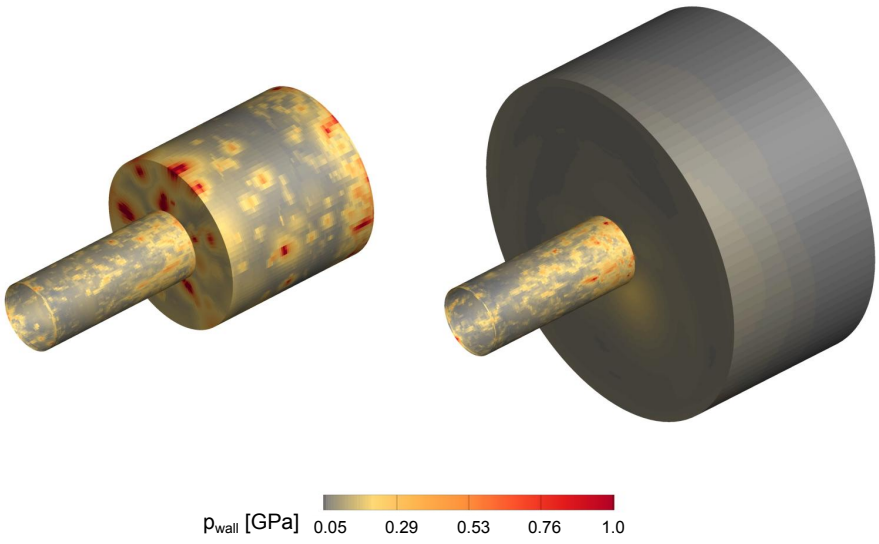

Figure 6.12: Recorded surface loads in Design D (left) and Design E (right) during 0.2 ms.

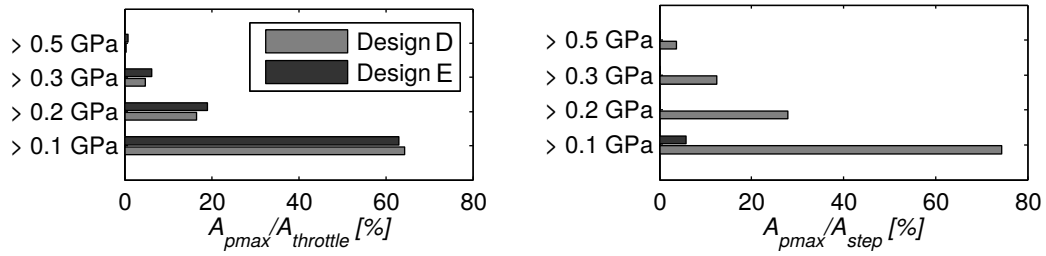

Figure 6.13: Coverage of the throttle and step-hole surfaces with the recorded wall pressure exceeding a certain threshold.

6.3 Summary

We perform a CFD analysis of the cavitating throttle flow in a submerged environment under realistic operating conditions by employing a fully compressible flow solver and a homogeneous equilibrium cavitation model. A barotropic description of the ISO 4113 test fuel under cavitating and non-cavitating condition is utilized. Comparison of the discharge coefficients against theoretical values shows good agreement. Numerical simulations reveal a highly unsteady cavitating flow in both considered designs with the dominant frequency of the inherent shedding instability on the order of 100 kHz. Two simultaneous mechanisms causing a pulsating excitation of the high-speed liquid jet are identified: quasi-periodic growth and decay of the cavity in the throttle and upstream propagation of pressure waves after the collapse of toroidal vapor clouds in the step-hole. In Design D, the coupling between both is stronger, causing a more regular oscillation of the monitored flow field quantities. The observed phenomenon reflects in the computed power spectra as well. The collapse of vapor structures in the step-hole affects the flow to a greater extent, since shock wave propagation emanating from the collapse of vapor clouds is bounded to a smaller volume. Moreover, the coupling is enhanced by the intermittent filling of the entire step-hole with vapor, which is followed by a violent inertia-driven collapse of the entire vapor structure. Although the collapse of vapor clouds in the step-hole of Design E affects the throttle flow as well, its effect is weaker, since shock propagation is not restricted to a small volume.

Cavities on the jet periphery are found to collapse with pressures up to several GPa, generating surface loads of more than 0.5 GPa in the step-hole of Design D. The observed wall pressure

peaks exceed the yield strength of common ductile materials, and may create sites with plastic deformation. In contrast, the walls of the step-hole of Design E are not subjected to high surface loads.

7 Effects of Non-condensable Gas and Turbulence on the Throttle Flow

In this chapter we examine separately the influence of non-condensable gas and turbulence on the cavitating throttle flow. Non-condensable gas effects are assessed for three operating points with different amounts of gas added to the fluid.

7.1 Non-condensable Gas Effects

7.1.1 Estimation of the Non-condensable Gas Content

Gases are always present to a certain extent in liquids. If a free surface of a sub-saturated liquid is exposed to the atmospheric conditions, there will exist a diffusive flux of air into the liquid until equilibrium is reached, i.e. until the liquid surface is saturated with air. Time scales of such a diffusive process are very long, on the order of hours. Complete dissolution of gases into a liquid is not possible, even in laboratory conditions. Gases are therefore either dissolved in the surrounding liquid or free, in the form of cavitation nuclei. According to Henry's law, the amount of dissolved gas is proportional to the partial pressure of the gas phase. Several studies have addressed the importance of dissolved gas on the nuclei content [57, 81, 85]. Non-condensable (free) gases change the compressibility of the medium and alter other properties consequently. An exact amount of gas (either dissolved or free) is usually not known in engineering applications. It depends not only on the temperature and pressure, but also on the utilized storage system or configuration of the technical device (flow through high pressure pumps, valves, orifices etc.). The gas model introduced in Chapter 3 allows us to prescribe

an effective amount of non-condensable gas to the working fluid. Since the developed gas model doesn't include degassing or gas absorption effects, the prescribed gas content remains constant during the whole simulation. Gas solubility can either be determined from Henry's law, or alternatively by Ostwald solubility [88]. Knowing the Ostwald coefficient L_v, which is defined as the volume of solvent V_l needed to dissolve a volume of gas V_g

$$L_v = \frac{V_g}{V_l}\,, \tag{7.1}$$

and applying the ideal gas law, we express the mass fraction of dissolved gas ε_g as

$$\varepsilon_g = \left[1 + \frac{\rho_l R T_g}{L_v p_g}\right]^{-1}\,, \tag{7.2}$$

where subscripts l and g represent the liquid and gas state, respectively. Using the reported value of Ostwald coefficient $L_v = 0.12\%$, at atmospheric conditions ($T = 25°$ C, $p = 1.01325$ bar) for the solubility of air in Diesel calibration fuel ISO 4113 [60], we estimate the amount of the initially dissolved gas to $\varepsilon_g = 1.73854 \times 10^{-4}$. This amount of gas represents the saturation capacity of the liquid and therefore the upper theoretical limit. In order to numerically asses the influence of the fixed amount of non-condensable gas on the cavity dynamics, we define three operating points, as listed in Table 7.1. For the *Saturated Diesel* case we fix the amount of free gas to the saturation concentration. However, for the *Standard Diesel* case, we expect the amount of free gas to be considerably smaller. *Degassed Diesel* includes a very small amount of free gas, which is two orders in magnitude smaller than for the *Standard Diesel* case.

operating point	ε
Saturated Diesel	1.73854×10^{-4}
Standard Diesel	1.73854×10^{-5}
Degassed Diesel	1×10^{-7}

Table 7.1: Prescribed free gas contents.

The effect of adding a fixed amount of non-condensable gas to the liquid is given in Fig. 7.1. For the amount of gas equal to zero ($\varepsilon = 0$), the equation of state for the pure liquid becomes very stiff for the whole applicable range and there exists a very sharp bend at the saturation conditions. However, for small values of gas mass fractions ($\varepsilon \ll 1$), this behavior becomes softened at low pressures, as changes in the pressure Δp are accompanied by larger variations

in the density $\Delta\rho$.This allows for the expansion of the liquid-gas mixture due to the included gas and postpones the development of cavitation.

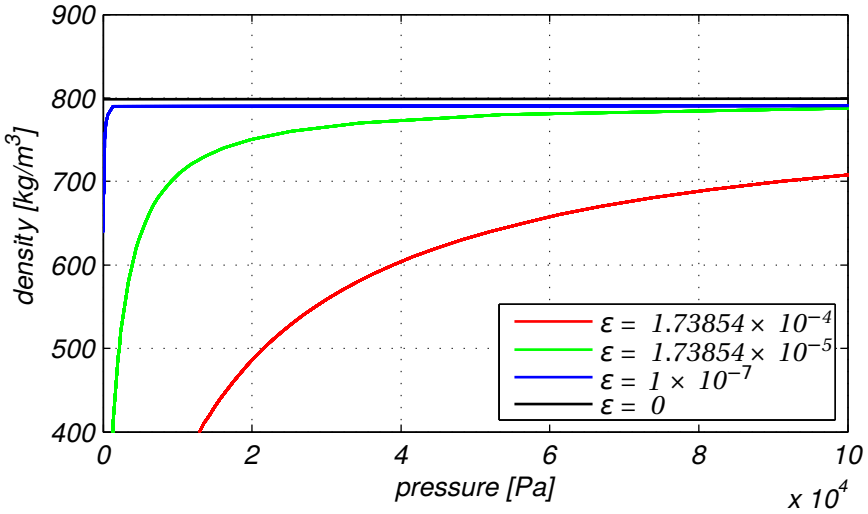

Figure 7.1: Effect of the prescribed fixed amount of non-condensible gas on the mixture density.

7.1.2 Computational Setup

We utilize Design A geometry for the investigation of the non-condensible gas influence on the throttle flow. The prescribed static pressures at the domain inlet and outlet are p_{in} = 2000 bar and p_{out} = 60 bar, respectively. Velocity is extrapolated from the domain interior. The numerical domain is initially filled with the ISO 4113 calibration fuel at rest and initialized with pressure $p = p_{out}$. Solid boundaries are treated as adiabatic and inviscid. In addition to this, a fixed amount of non-condensable gas is prescribed, as reported in Table 7.1. Numerical grids utilized for this computations are *Level 1* and *Level 2* as already depicted in Fig. 5.1. *Level 1* grid is used primarily for the flow field development, whereas flow field analysis is carried out at *Level 2* grid.

7.1.3 Results

Figure 7.2 shows the mean mixture density at the throttle mid-plane. The density scale is adjusted to the range below the saturation density of the pure liquid ($\rho_{l,sat}$ = 798.72 kg/m^3). An indicative expansion below the liquid saturation density is observed for the *Saturated*

Diesel case. This is a direct consequence of the high gas content added to the liquid. As there is no scalar transport of the gas mass fraction through the computational domain, we see the net effect of the gas expansion. At the throttle exit, compression is visible as the pressure recovers to the prescribed outlet value. For the *Standard Diesel* case, a minor decrease below

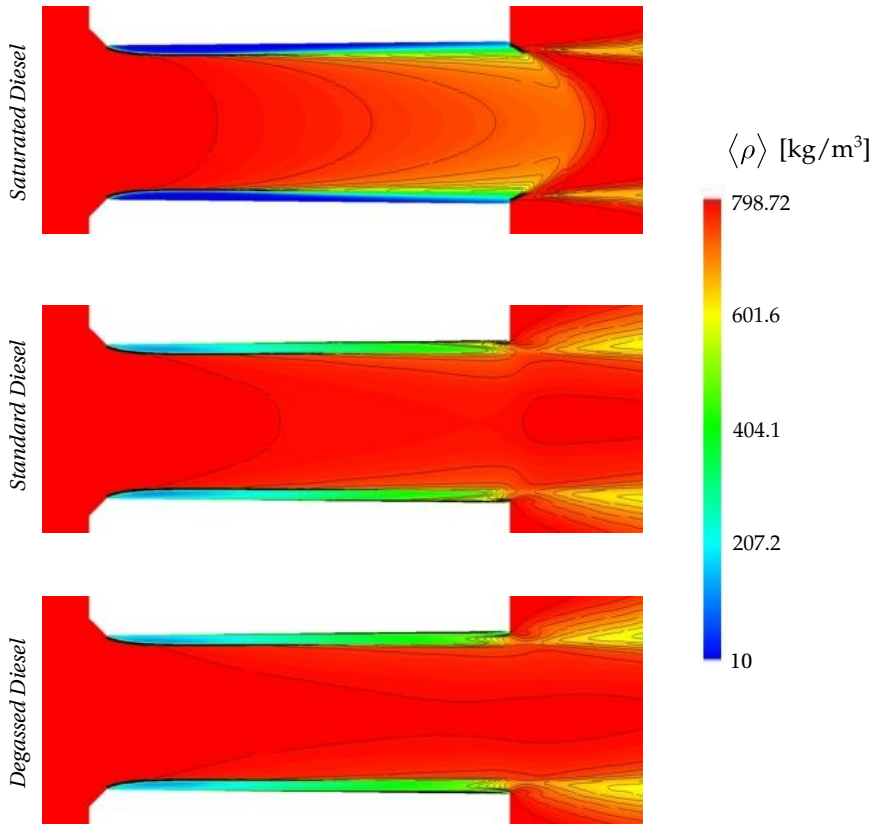

Figure 7.2: Time-averaged mixture density $\langle\rho\rangle$ at the mid-plane of the throttle.

$\rho_{l,sat}$ value from the approximately first third of the throttle is visible. If a further decrease in the gas content is utilized, no liquid-gas mixture along the throttle centerline is present, as in the *Degassed Diesel* case. Here, a slight decrease in the mixture density of the liquid core towards throttle walls is observed, which is a consequence of temporal averaging, as the vapor pockets develop in the vicinity of the walls during the cavity shedding. The flow along the throttle centerline remains liquid throughout the computation. The flow field in the *Degassed Diesel* case is essentially the same as in Design A (see Chapter 5). Large fluctuations of the mass flow rate and vapor volume are recorded in the throttle. The mean level and amplitude of oscillations reduce with the inclusion of non-condensable gas, as shown in Fig. 7.3. Less cavitation is produced in the throttle and in the whole numerical domain and

the oscillations in the flow field are damped. For the *Saturated Diesel* case we observe a steady flow field. Vapor production is limited to the throttle wall, where a stationary cavity develops. Duke et al. [33] reported a significant difference in the cavitation appearance in polycarbonate nozzles between degassed and untreated calibration fuels. For degassed fuels, a cavity attached to the nozzle walls. In contrast to this, untreated fuels showed a void formation along the nozzle centerline, where cavitation was not initially expected. Authors suggested that pseudo cavitation was a possible cause of such a significant discrepancy. This observation is in line with the current study, which demonstrates the possibility of non-condensable gas expansion in the liquid core if a certain threshold of the gas mass fraction is exceeded.

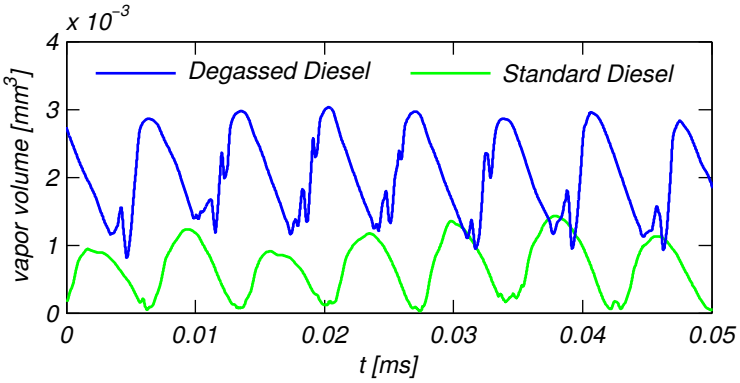

Figure 7.3: Temporal evolution of the vapor volume in the throttle.

Figure 7.4 shows characteristic shedding frequencies for the *Standard Diesel* and the *Degassed Diesel* case. A minor increase in the cavity shedding cycle is observed for the *Standard Diesel* case. Visual observation of 1000 consecutive snapshots ($\Delta t_{frame} \approx 2.6 \times 10^{-8}$ s) demonstrates qualitatively the same behavior of the cavity in the throttle: the development of the distinctive cavity sheet and the formation of re-entrant motion. Representative snapshots of one cavity period in the *Standard Diesel* case are given in Appendix A.2.

We assess the erosive potential of the specific operating point by employing the collapse detection algorithm and by comparing the cumulative rate of collapse events. Figure 7.5 depicts recorded events in the throttle and in the whole domain. Collapse events shown in gray color correspond to those found in Design A and serve here as a reference. There is essentially no difference in the collapse magnitude and rate when including a small amount of non-condensible gas (*Degassed Diesel*) or excluding it completely (Design A). However, the

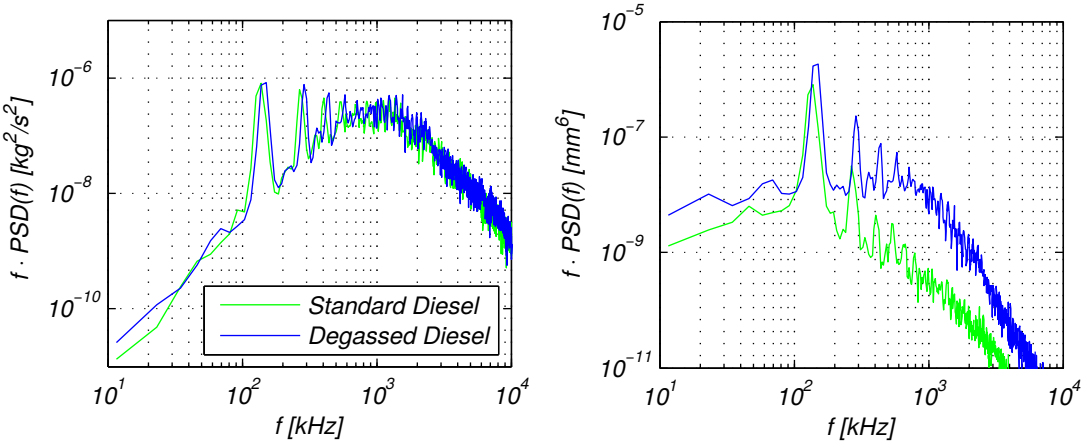

Figure 7.4: Pre-multiplied power spectral density of the mass flow rate at the throttle outlet (left) and the vapor volume in the throttle (right).

difference increases as a higher amount of non-condensable gas is added to the liquid. The diagram suggests a decreased erosive potential for the *Standard Diesel* case. For the *Saturated Diesel* case, no collapse events are found at all.

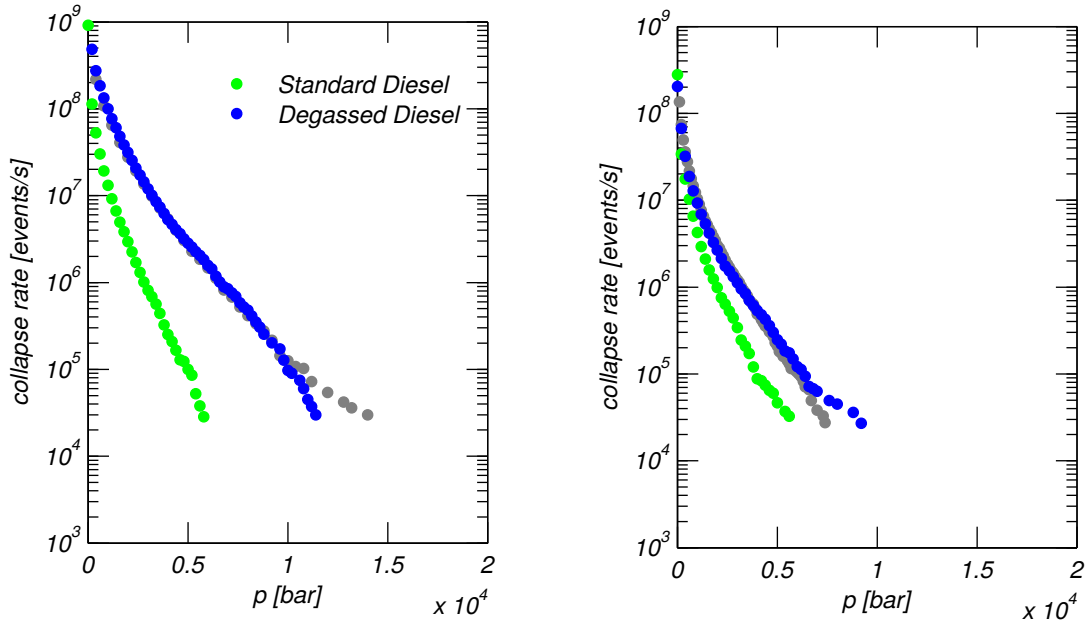

Figure 7.5: Cumulative collapse rates. Left: whole domain, Right: throttle

7.2 Turbulence Effects

The aim of the present study is to qualitatively examine the influence of turbulence on cavity dynamics on the example of Design A. This geometry is extensively investigated by means of inviscid simulations in Chapter 5. Recent implementation of an implicit subgrid-scale model by Egerer et al. [40] has enabled efficient computation of cavitating flows by the large-eddy simulation (LES) approach within our compressible framework. Although early studies utilized primarily RANS methodology for cavitating flow simulation [51, 109, 3, 46], LES approach has been rapidly gaining in popularity [65, 83, 39, 38], mainly due to the increase in the available processing power. Still, LES computation of micro channel flows at high Reynolds numbers is challenging.

7.2.1 Computational Setup

The flow is governed by the compressible Navier-Stokes equations. We employ barotropic equations of state for single and two-phase descriptions of the ISO 4113 calibration fuel. Subgrid scale modeling is utilized implicitly by the truncation error of discretization. We switch from central to upwind-biased reconstruction scheme based on the flow sensor functional [40]. The explicit, four-stage Runge-Kutta method is used for time advancement. At the domain inlet and outlet, asymptotic pressure boundary conditions are applied (p_{in} = 2000 bar, p_{out} = 60 bar). All other quantities at the inlet and outlet surfaces are extrapolated from the domain interior.

	Level 1	*Level 2*
Total cell count [$\times 10^6$]	4.2	8.8
Cell size: throttle core [$\times 10^{-6}$ m]	5	4
Cell height: throttle wall [$\times 10^{-6}$ m]	0.4	0.26
Time step [$\times 10^{-10}$ s]	1.1	0.5

Table 7.2: Parameters of the utilized grids.

No-slip boundary condition is imposed at the solid walls and no wall model is employed. We utilize two different grid levels, as shown in Fig. 7.6. *Level 1* grid comprises approximately 4.2×10^6 cells, whereas *Level 2* grid containts 8.8×10^6 cells. Block-structured topology of the numerical grid is adjusted around the throttle inlet in order to avoid high aspect-ratio cells

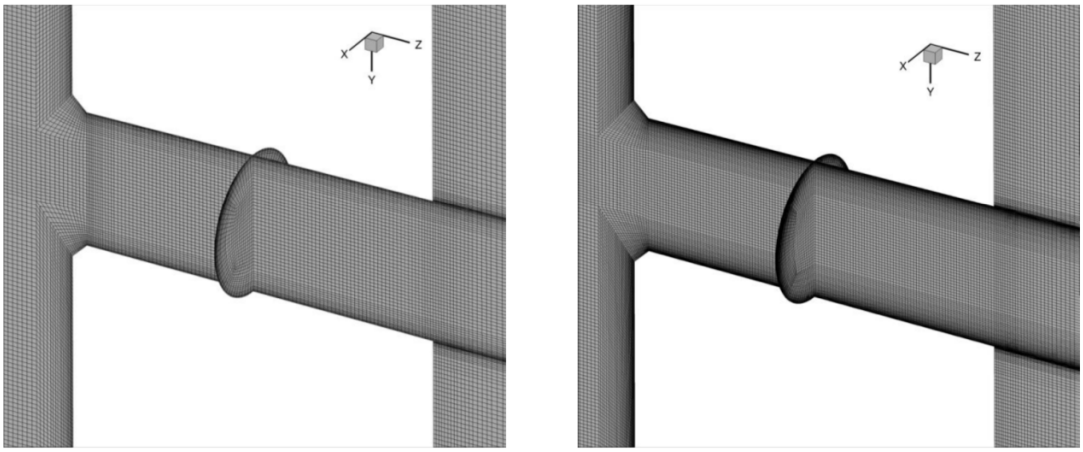

Figure 7.6: Computational grid at two refinement levels. Left: *Level 1* grid , right: *Level 2* grid.

throughout the domain and to reduce the total number of cells. Cell sizes along the throttle centerline are approximately 4-5 μm. Distances from the first near-wall cell centers to the throttle walls lie in the range 0.13-0.4 μm, depending on the grid level. Grid parameters are summarized in Table 7.2. We initialize the flow field from the inviscid solution by interpolating flow quantities on the *Level 1* grid. CFL number at both grid levels is fixed to 1.4.

Reynolds number in the throttle, based on the bulk velocity estimated by the Bernoulli equation $U_B = \sqrt{2\Delta p/\rho_{in}} \approx 670$ m/s, mean throttle diameter $d_m = 187$ μm and kinematic viscosity of the liquid phase $\nu \approx 2.5 \times 10^{-6}$ m^2/s at the reference temperature $T_{ref} = 323.15$ K is approximately 50000. Figure 7.7 shows wall resolution in terms of non-dimensional wall distance $y^+ = \frac{u_\tau y}{\nu}$ at the respected grid level. At both grid levels, the first cell layer lies within the viscous sublayer $y^+ < 5$, and thus favors the computational approach without the utilization of the wall model.

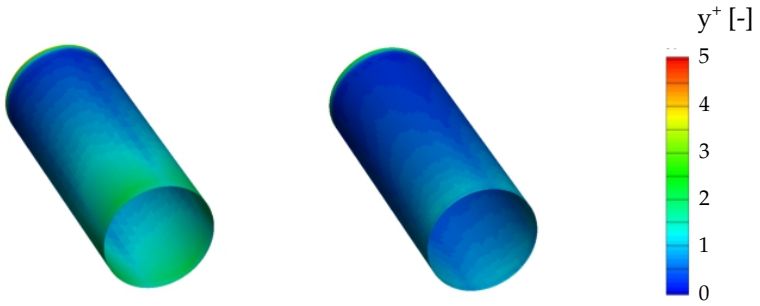

Figure 7.7: Wall-normal resolution in the throttle. Left: *Level 1* grid, right: *Level 2* grid.

7.2.2 Results

We examine the grid convergence on the profiles of time-averaged flow quantities as shown in Fig. 7.8. Time-averaged pressure $\langle p \rangle$, vapor volume fraction $\langle \alpha \rangle$ and axial velocity $\langle w \rangle$ are extracted along the line in the cavitating sheet. Additionally, exit velocity profile at the throttle mid-plane is shown. A difference between the employed grids is only observed in the vapor volume fraction profile, showing an increased vapor volume level at the *Level 2* grid. The cavity sheet at the *Level 1* grid is resolved with 11 cells in the wall-normal direction, whereas approximately 25 cells resolve it on the *Level 2* grid. At the throttle exit, a flat velocity profile is formed with the magnitude close to the Bernoulli value.

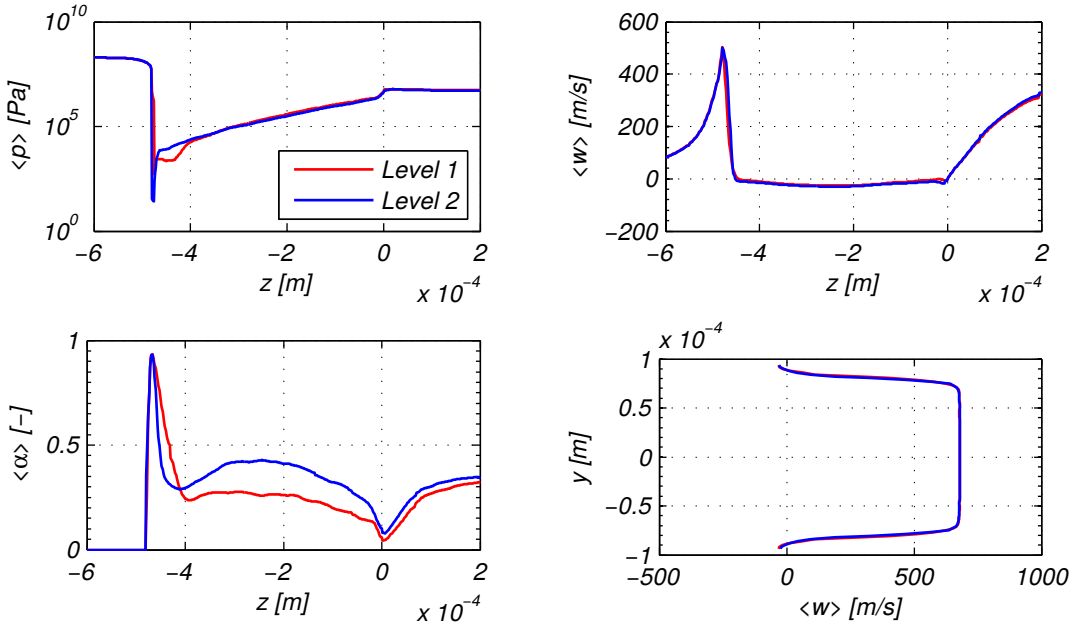

Figure 7.8: Grid convergence of time-averaged quantities near throttle wall. Time-averaged velocity component $\langle w \rangle$ is plotted at the throttle exit as well.

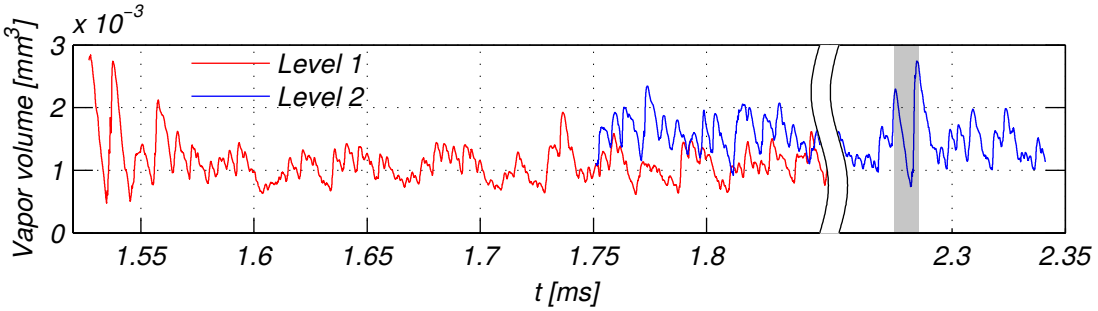

Figure 7.9: Temporal evolution of the vapor volume in the throttle at both grid levels.

After the initial transients due to the inviscid initialization decay, a turbulent flow field in the throttle establishes. Figure 7.9 shows a time history of the vapor volume in the throttle. We observe fluctuations at both grid levels. The gray rectangular area marks one cavity cycle at the *Level 2* grid. Representative flow snapshots during the considered cavity period are shown in Fig. 7.10. The flow field qualitatively resembles the one obtained by the inviscid simulation – a supercavity attaches to the throttle walls and is followed by the successive development of the re-entrant flow. Optical examination of approximately 5000 consecutive snapshots ($\Delta t_{frame} \approx 1 \times 10^{-9}$ s) confirms more stochastic cavity dynamics, which may vary from cycle to cycle. The duration of the marked cavity period is approximately 8.8×10^{-3} ms, which correlates to the shedding frequency of 115 kHz. During the cavity growth, no distinctive

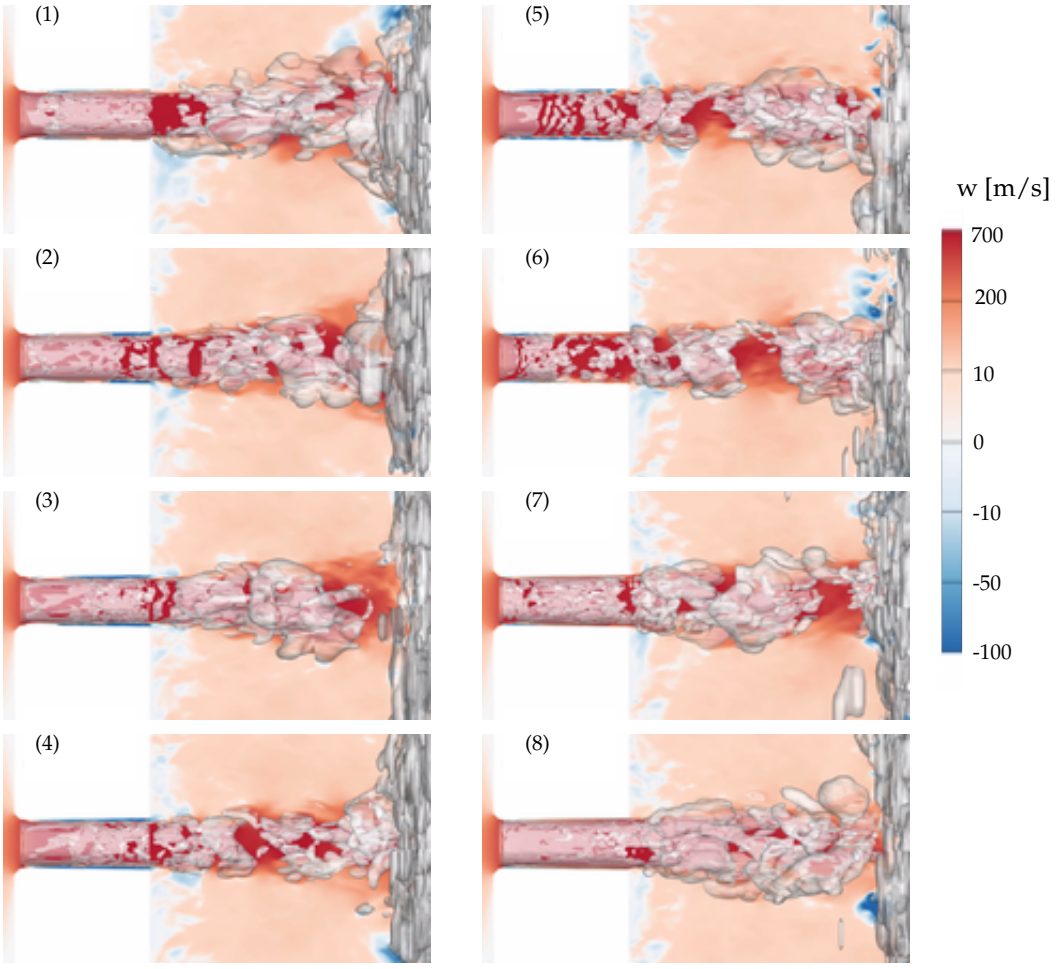

Figure 7.10: Snapshots of the flow field during one cavity cycle. Instantaneous velocity w shown at mid-plane together with iso-surfaces of vapor volume fraction $\alpha = 10\%$.

development of the sheet front is observed and the cavity restores from small vapor pockets during the propagation of the re-entrant flow. This is in contrast to the inviscid solution, where fluctuations are nearly periodic and a growing cavity sheet is clearly visible.

One possible explanation for this discrepancy could be the application of the no-slip boundary condition at solid walls. Whereas the utilization of the no-slip boundaries is justified when modeling near-wall effects on the velocity profile of the high-density liquid, we reconsider the adequacy of this boundary condition if the walls of the micro device are immersed into the low-density cavitating mixture. The cavitating mixture is considered as a continuum if the mean free path λ (the average distance one molecule travels between collisions), is small compared to the characteristic length, L. Knudsen number Kn is thus defined as [18]

$$Kn = \frac{\lambda}{L}. \tag{7.3}$$

The continuum assumption implies a very small Knudsen number, $Kn < 0.01$. Following an analysis given by Oosthuizen and Carscallen [82], the order of magnitude of the mean free path can be estimated by computing the ratio of the dynamic viscosity μ and acoustic impedance ρc

$$\lambda \sim \frac{\mu}{\rho c}. \tag{7.4}$$

First, we provide an estimation of the mean free path for the water vapor, whose thermodynamic properties have been extensively documented. The properties of the liquid water are taken at the reference temperature $T = 293.15$ K. The expression for the the equilibrium speed of sound c is given in Appendix A.1, together with other thermodynamic properties of water at the reference temperature. The mixture viscosity is modeled with the Beattie-Whalley model (Eq. 3.23). Figure 7.11 depicts the mean free path for different values of the vapor volume fraction. We observe that $\lambda \approx \mathcal{O}(10^{-5}$ m) for the volume fractions up to 0.8. After applying this analysis to the thermodynamic model of Diesel calibration fuel utilized in this study, we obtain the same order of magnitude for λ in the cavitating mixture. Considering the cavity thickness $\delta \approx 1.5 \times 10^{-5}$ m as the characteristic length, the Knudsen number in the cavitating mixtures is on the order of 1. This suggests that infrequent molecular collisions occur across

the cavitating sheet and that molecules are more likely to meet solid surfaces with full velocity, i.e. there would not exist velocity gradient across the cavity. Therefore, allowing for a slip in velocity near solid walls could be probably more suitable when computing flows where a cavity attaches to the surfaces of micro devices.

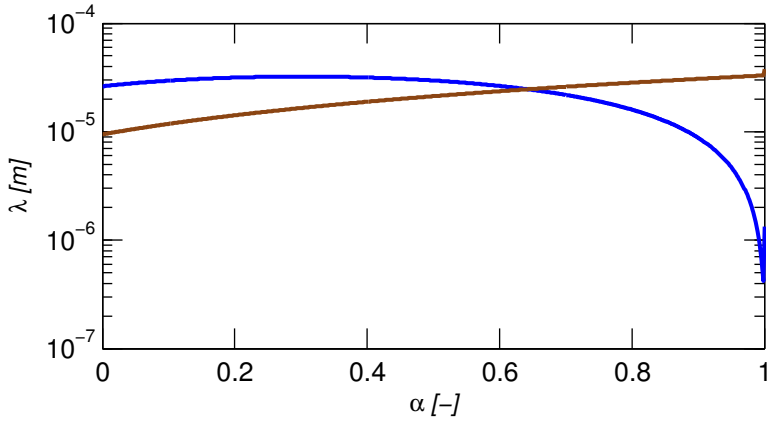

Figure 7.11: Variation of the mean free path for different values of the vapor volume fraction α on the example of water vapor (blue curve) and Diesel calibration fuel (brown curve).

7.3 Summary

The first part of the present chapter demonstrates the influence of non-condensable gas on cavitation in the throttle. A net effect of a constant gas amount added to the fluid is numerically assessed for three operating points. The *Saturated Diesel* case demonstrates a possibility of pseudo cavitation in the throttle core when the amount of the included gas is sufficiently high. The effect of pseudo cavitation is significantly reduced in the *Standard Diesel* case. The cavity dynamics in this operating point is comparable to that observed in the *Degassed Diesel*, but oscillations are damped due to gas presence. Although regulation of the exact amount of gas in hydraulic systems is difficult in practice, the obtained results indicate that the overall system performance can be affected to a large extent.

In the second part, a wall resolved LES computation at two grid levels is performed. The flow field looks qualitatively very similar to that obtained by the inviscid approach, but differences in cavity dynamics are discovered. Cavity shedding is more irregular and a small vapor pockets seem to coalesce and merge and in this way build a supercavity in the throttle. We hypothesize

that the discrepancy in the cavity dynamics between the inviscid and viscous solution may be attributed to the imposition of the no-slip boundary condition. Based on the estimation of the Knudsen number in the cavity, which is on the order of 1, rare molecular collisions are more likely to occur. Therefore, an absence of the velocity gradient in the wall-normal direction suggests the utilization of the slip boundary condition for the cavitating mixture.

8 Summary and Conclusion

Cavitation occurs in different components of Diesel injection system, with both beneficial and detrimental effects. Understanding cavitation phenomena has become an imperative in designing efficient and durable injector components. Pressure drops on the order of thousand bars across throttles and nozzles cause a substantial acceleration of the bulk liquid and evaporation near device walls. The main feature of these phenomena is a high-frequency unsteadiness, accompanied by a shedding of vapor cavities. Once advected to the increased pressure regions, violent cavity collapses take place.

In this work, we have employed a fully compressible flow solver in order to investigate geometric and physical modeling aspects on the cavitation development in micro-size throttles. First, a thermodynamic model for a Diesel calibration fuel has been developed and extended with a non-condensable gas component. A CFD investigation of the flow in the realistic valve chamber has been carried out, and based on the gained knowledge, five generic designs have been proposed for more elaborate investigations.

For the investigation of geometric influences, an inviscid approach has been utilized, as cavitation development is driven by the inertia effect at the choked operating regime. The first part of investigations included three distinct throttle designs. Nearly periodic, high-frequency cavity pulsation has been detected, with the simultaneous development of the classic re-entrant jet and bubbly shock. The estimation of Strouhal numbers suggested that the observed phenomena differ from the shedding instabilities observed at large-scale hydrofoils.

Although experimental investigations in the submerged environment at these scales and operating points are not documented in the open literature, large-scale observations reported similar cavity dynamics [24, 25]. Further, by carrying out the erosion risk assessment, we have revealed mechanisms responsible for high pressure spots on the throttle walls. The second part of investigations encompassed simulations of the generic valve chamber setup with an additional step-hole mounted on the discharge throttle. These simulations have shown that the upstream propagation of pressure waves, which develop after cavity collapse in the step-hole, act as an additional mechanism responsible for the high-frequency cavity pulsation. Depending on the step-hole diameter, the coupling between intrinsic shedding instability emanating from the throttle and collapse-driven pressure wave development from the step-hole, becomes stronger or weaker. We have confirmed that integral flow quantities, such as time-dependent evolution of the vapor volume, can not be directly linked to cavitation erosion, without obtaining information about the spatial and temporal collapse occurrence.

Physical modeling aspects included separate investigations of non-condensable gas and turbulence effects. A fixed amount of non-condensable gas has been added to the fluid and numerically assessed for three operating points. The operating point with the highest gas content has shown a possibility of pseudo-cavitation in the throttle core. The impact of the non-condensable gas on the cavity dynamics and collapse spectra has been demonstrated as well: whereas a sufficiently high gas content leads to a steady throttle flow without evidence of collapse events, degassing a fuel restores cavity and collapse behaviors to those observed when the thermodynamic model without gas is utilized. For the intermediate case, cavity dynamics alters slightly compared to the degassed case and collapse events are damped. Investigations with the novel ILES approach have shown qualitatively the same flow topology as inviscid simulations: developing supercavity followed by re-entrant motion. However, the cavity dynamics alters. One possible explanation for the changed behavior gives the estimation of the Knudsen number in the attached cavity, which is on the order of 1. This suggests that allowing for the velocity slip in the mixture phase would be probably more suitable at these geometric scales.

The investigations in this thesis provide a deeper insight and enhance the understanding of flow dynamics in cavitating micro throttles, whose experimental assessment is for the time

being not possible at industry-relevant spatial scales and operating conditions.

A Appendix

A.1 Equilibrium Speed of Sound in Cavitating Flow

The definition of the speed of sound in two-phase flows with the infinitely fast phase change is given by Franc and Michel [43]. The thermodynamic equilibrium is assumed and the surface tension is neglected. The phase change is initiated by changing the pressure for δp, which therefore transfers the mass of the liquid δm into vapor. The equilibrium speed of sound thus becomes

$$\frac{1}{\rho c^2} \cong \frac{\alpha}{\rho_{vap,sat} c_{vap}^2} + \frac{1-\alpha}{\rho_{l,sat} c_l^2} + \frac{(1-\alpha)\rho_{l,sat} c_{p,l} T}{\rho_{vap,sat} L_{vap}}, \tag{A.1}$$

where ρ is the mixture density, c the mixture speed of sound, L_{vap} the latent heat of vaporization and $c_{p,l}$ is the liquid heat capacity at constant pressure. Figure A.1 plots the equilibrium speed of sound in the cavitating mixture of the water-vapor (Eq. A.1). The speed of sound in the cavitating mixture drops up to three orders of magnitude compared to the speed of sound in the pure liquid. Additionally, the Beattie-Whalley mixture viscosity model (Eq. 3.23) for different values of the vapor volume fraction at the temperature $T = 293.15$ K is shown. Thermodynamic properties of the water at the reference temperature are summarized in Table A.1.

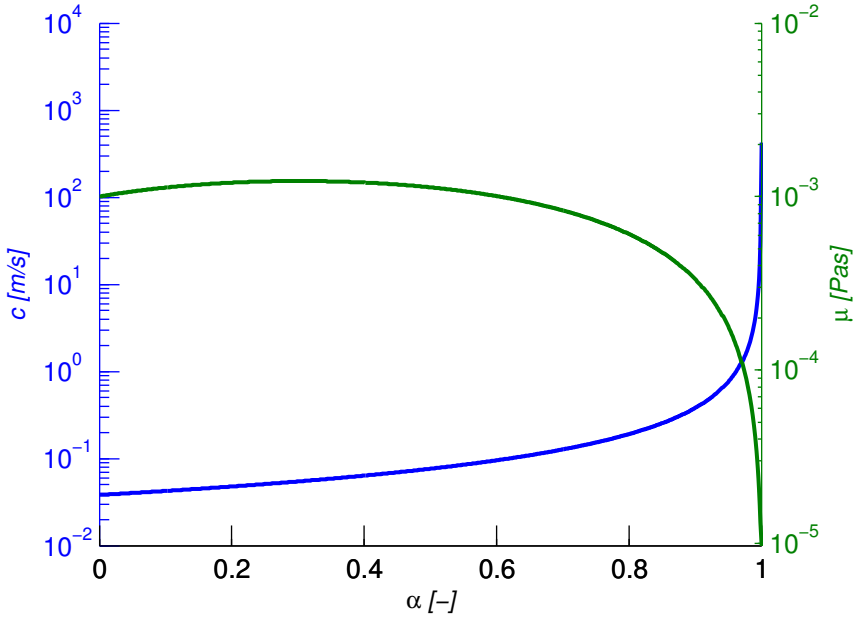

Figure A.1: Equilibrium speed of sound for two-phase flow (blue curve) and the mixture viscosity (green curve) for different values of vapor volume fration α.

Property	Value
p_{sat} [Pa]	2339.3
$\rho_{l,sat}$ [kg/m^3]	998.16
$\rho_{vap,sat}$ [kg/m^3]	0.0172
c_l [m/s]	1482.2
c_{vap} [m/s]	423.18
μ_{liq} [$\times 10^{-6}$ Pas]	1001.4
μ_{vap} [$\times 10^{-6}$ Pas]	9.7275
L_{vap} [$\times 10^3$ J/kgK]	2453.48
$c_{p,l}$ [J/kgK]	4184.4

Table A.1: Thermodynamic properties of water at $T = 293.15$ K.

A.2 Cavity Dynamics in *Standard Diesel* Case

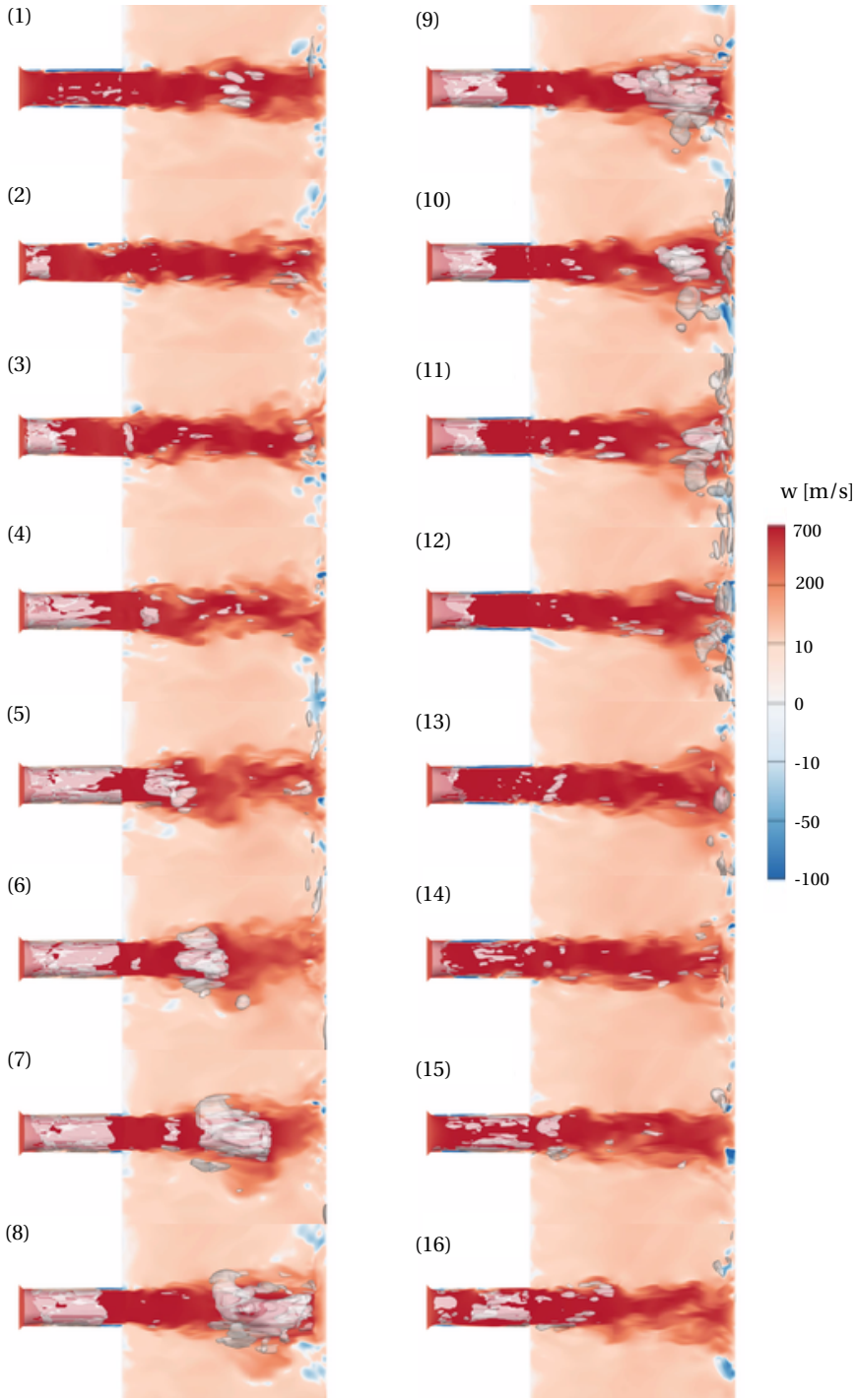

Figure A.2: Representative snapshots during one shedding cycle in *Standard Diesel* case. Instantaneous velocity shown at mid-plane together with iso-surfaces of vapor volume fraction $\alpha = 10\%$.

Bibliography

[1] Commission Regulation (EU) No 459/2012. *Official Journal of the European Union*.

[2] U.S., Japan and Germany Join Australian Stealth Research. https://www.maritime-executive.com/article/us-japan-and-germany-join-australian-stealth-research. [Online; accessed 16-May-2018].

[3] Andriotis, A., M. Gavaises, and C. Arcoumanis (2008). Vortex flow and cavitation in diesel injector nozzles. *Journal of Fluid Mechanics 610*, 195–215.

[4] Arcoumanis, C., H. Flora, M. Gavaises, and M. Badami (2000). Cavitation in real-size multi-hole diesel injector nozzles. Technical report, SAE Technical Paper.

[5] Badock, C., R. Wirth, A. Fath, and A. Leipertz (1999). Investigation of cavitation in real size diesel injection nozzles. *International journal of heat and fluid flow 20*(5), 538–544.

[6] Bartsch, C. (2006). *Piezo-Diesel-Direkteinspritzung: historische Entwicklung und Stand der Technik bei Common-Rail und Pumpedüse*. Verlag Moderne Industrie.

[7] Basara, A. (2007). Evaluation of High Pressure Components of Fuel Injection Systems Using Speckle Interferometry.

[8] Battistoni, M., D. J. Duke, A. B. Swantek, F. Z. Tilocco, C. F. Powell, and S. Som (2015). Effects of noncondensable gas on cavitating nozzles. *Atomization and Sprays 25*(6).

[9] Bauer, D., H. Chaves, and C. Arcoumanis (2012). Measurements of void fraction distribution in cavitating pipe flow using x-ray CT. *Measurement Science and Technology 23*(5), 055302.

[10] Bauer, W., U. Iben, and M. Voss (2004). Berechnung kavitierender Strömungen in Einspritzsystemen. *VDI Berichte* (1846), 1029–1042.

[11] Bazile, J.-P., D. Nasri, C. Boned, J. L. Daridon, and others (2012). High pressure thermophysical characterization of fuel used for testing and calibrating diesel injection systems. *Fuel 98*, 288–294.

[12] Beattie, D. R. H. and P. B. Whalley (1982). A simple two-phase frictional pressure drop calculation method. *International Journal of Multiphase Flow 8*(1), 83–87.

[13] Beban, B., S. Legat, S. J. Schmidt, and N. A. Adams (2015). On instationary mechanisms in cavitating micro throttles. In *Journal of Physics: Conference Series*, Volume 656, pp. 012079. IOP Publishing.

[14] Beban, B., S. J. Schmidt, and N. A. Adams (2016). Numerical investigation of flow dynamics in cavitating micro throttles and connection to cavitation erosion. In *International Conference for Liquid Atomization and Spray Systems (ILASS), Brighton, UK*.

[15] Beban, B., S. J. Schmidt, and N. A. Adams (2017). Numerical study of submerged cavitating throttle flows. *Atomization and Sprays 27*(8).

[16] Benjamin, T. B. and A. T. Ellis (1966). The collapse of cavitation bubbles and the pressures thereby produced against solid boundaries. *Philosophical Transactions of the Royal Society of London A: Mathematical, Physical and Engineering Sciences 260*(1110), 221–240.

[17] Bergwerk, W. (1959). Flow pattern in diesel nozzle spray holes. *Proceedings of the Institution of Mechanical Engineers 173*(1), 655–660.

[18] Bird, G. A. (1994). *Molecular gas dynamics and the direct simulation gas flows*. Oxford Engineering Science.

[19] Birgel, A., N. Ladommatos, P. Aleiferis, N. Milovanovic, P. Lacey, and P. Richards (2011). Investigations on deposit formation in the holes of diesel injector nozzles. *SAE International Journal of Fuels and Lubricants 5*(2011-01-1924), 123–131.

[20] Blessing, M., G. Konig, C. Kruger, U. Michels, and V. Schwarz (2003). Analysis of flow and cavitation phenomena in diesel injection nozzles and its effects on spray and mixture formation. In *Fuel Injection Systems 2003: IMechE Conference Transactions 2003*, Volume 2, pp. 21.

[21] Brennen, C. E. (2013). *Cavitation and bubble dynamics*. Cambridge University Press.

[22] Briggs, L. J. (1950). Limiting negative pressure of water. *Journal of Applied Physics 21*(7), 721–722.

[23] Busch, R. (2001). *Untersuchung von Kavitationsphä anomenen in Dieseleinspritzdü usen*. Ph. D. thesis, Universität Hannover, Hannover.

[24] Bush, D., C. Soteriou, M. Winterbourn, and C. Daveau (2015). Dynamic cavitation inside a high performance diesel injector-an experimental and CFD investigation. In *Journal of Physics: Conference Series*, Volume 656, pp. 012080. IOP Publishing.

[25] Callenaere, M., J.-P. Franc, J.-M. Michel, and M. Riondet (2001). The cavitation instability induced by the development of a re-entrant jet. *Journal of Fluid Mechanics 444*, 223–256.

[26] Chaves, H., M. Knapp, A. Kubitzek, F. Obermeier, and T. Schneider (1995). Experimental study of cavitation in the nozzle hole of diesel injectors using transparent nozzles. Technical report, SAE technical paper.

[27] Chorążewski, M., F. Dergal, T. Sawaya, I. Mokbel, J.-P. E. Grolier, and J. Jose (2013). Thermophysical properties of Normafluid (ISO 4113) over wide pressure and temperature ranges. *Fuel 105*, 440–450.

[28] Coleman, A. J., J. E. Saunders, L. A. Crum, and M. Dyson (1987). Acoustic cavitation generated by an extracorporeal shockwave lithotripter. *Ultrasound in medicine & biology 13*(2), 69–76.

[29] Daily, J. W. and D. R. F. Harleman (1966). *Fluid Dynamics, 454 pp.* Addison-Wesley Publ. Co., Inc.

[30] Delannoy, Y. (1990). Two phase flow approach in unsteady cavitation modelling. In *Proc. of Cavitation and Multiphase Flow Forum, 1990*.

[31] Ducros, F., V. Ferrand, F. Nicoud, C. Weber, D. Darracq, C. Gacherieu, and T. Poinsot (1999). Large-eddy simulation of the shock/turbulence interaction. *Journal of Computational Physics 152*(2), 517–549.

[32] Duke, D. J., A. L. Kastengren, A. B. Swantek, K. E. Matusik, and C. F. Powell (2016). X-ray fluorescence measurements of dissolved gas and cavitation. *Experiments in Fluids 57*(10), 162.

[33] Duke, D. J., A. L. Kastengren, F. Z. Tilocco, A. B. Swantek, and C. F. Powell (2013). X-ray radiography measurements of cavitating nozzle flow. *Atomization and Sprays 23*(9).

[34] Duke, D. J., K. E. Matusik, A. L. Kastengren, A. B. Swantek, N. Sovis, R. Payri, J. P. Viera, and C. F. Powell (2017). X-ray radiography of cavitation in a beryllium alloy nozzle. *International Journal of Engine Research*, 1468087416685965.

[35] Duke, D. J., D. P. Schmidt, K. Neroorkar, A. L. Kastengren, and C. F. Powell (2013). High-resolution large eddy simulations of cavitating gasoline–ethanol blends. *International Journal of Engine Research 14*(6), 578–589.

[36] Duke, D. J., A. B. Swantek, K. E. Matusik, C. F. Powell, A. L. Kastengren, J. P. Viera, R. Payri, and D. P. Schmidt (2016). X-ray radiography measurements and numerical simulations of cavitation in a metal nozzle. Dearborn, MI.

[37] Dular, M. and R. Bachert (2009). The issue of Strouhal number definition in cavitating flow. *Journal of Mechanical Engineering 55*(11), 666–674.

[38] Edelbauer, W., J. Strucl, and A. Morozov (2016). Large Eddy Simulation of cavitating throttle flow. In *Advances in Hydroinformatics*, pp. 501–517. Springer.

[39] Egerer, C. P., S. Hickel, S. J. Schmidt, and N. A. Adams (2014). Large-eddy simulation of turbulent cavitating flow in a micro channel. *Physics of Fluids (1994-present) 26*(8), 085102.

[40] Egerer, C. P., S. J. Schmidt, S. Hickel, and N. A. Adams (2016). Efficient implicit LES method for the simulation of turbulent cavitating flows. *Journal of Computational Physics 316*, 453–469.

[41] Ellis, A. T. and J. W. Starrett (1979). Observations of bubble dynamics in jet flows and at high ambient pressures. In *Proc. 5th Int. Conf. on Erosion by Solid and Liquid Impact, Cambridge*, pp. 57.

[42] Franc, J.-P. and J.-M. Michel (1985). Attached cavitation and the boundary layer: experimental investigation and numerical treatment. *Journal of Fluid Mechanics 154*, 63–90.

[43] Franc, J.-P. and J.-M. Michel (2006). *Fundamentals of cavitation*, Volume 76. Springer Science & Business Media.

[44] Freudigmann, H.-A., A. Dörr, U. Iben, and P. F. Pelz (2017). Modeling of Cavitation-Induced Air Release Phenomena in Micro-Orifice Flows. *Journal of Fluids Engineering 139*(11), 111301.

[45] Ganesh, H., S. A. Mäkiharju, and S. L. Ceccio (2016). Bubbly shock propagation as a mechanism for sheet-to-cloud transition of partial cavities. *Journal of Fluid Mechanics 802*, 37–78.

[46] Gavaises, M. (2008). Flow in valve covered orifice nozzles with cylindrical and tapered holes and link to cavitation erosion and engine exhaust emissions. *International Journal of Engine Research 9*(6), 435–447.

[47] Gavaises, M., A. Andriotis, D. Papoulias, N. Mitroglou, and A. Theodorakakos (2009). Characterization of string cavitation in large-scale Diesel nozzles with tapered holes. *Physics of Fluids (1994-present) 21*(5), 052107.

[48] Gavaises, M., D. Papoulias, A. Andriotis, E. Giannadakis, and A. Theodorakakos (2007). Link between cavitation development and erosion damage in diesel injector nozzles. Technical report, SAE Technical Paper.

[49] Giannadakis, E., M. Gavaises, and C. Arcoumanis (2008). Modelling of cavitation in diesel injector nozzles. *Journal of Fluid Mechanics 616*, 153–193.

[50] Giannadakis, E., M. Gavaises, and A. Theodorakakos (2009). The influence of variable fuel properties in high-pressure diesel injectors. Technical report, SAE Technical Paper.

[51] Goncalves, E. and R. F. Patella (2009). Numerical simulation of cavitating flows with homogeneous models. *Computers & Fluids 38*(9), 1682–1696.

[52] Hall, G. W. (1963). Analytical determination of the discharge characteristics of cylindrical-tube orifices. *Journal of mechanical engineering science 5*(1), 91–97.

[53] Harris, R. M., K. A. Edge, and D. G. Tilley (1994). The suction dynamics of positive displacement axial piston pumps. *Journal of dynamic systems, measurement, and control 116*(2), 281–287.

[54] He, L. and F. Ruiz (1995). Effect of cavitation on flow and turbulence in plain orifices for high-speed atomization. *Atomization and Sprays 5*(6).

[55] Hickel, S., N. A. Adams, and J. A. Domaradzki (2006). An adaptive local deconvolution method for implicit LES. *Journal of Computational Physics 213*(1), 413–436.

[56] Hickel, S., C. P. Egerer, and J. Larsson (2014). Subgrid-scale modeling for implicit large eddy simulation of compressible flows and shock-turbulence interaction. *Physics of Fluids 26*(10), 106101.

[57] Holl, J. W. (1970). Nuclei and cavitation. ASME.

[58] Iben, U., A. Morozov, E. Winklhofer, and R. Skoda (2011). Optical investigations of cavitating flow phenomena in micro channels using a nano second resolution. In *WIMRC 3rd International Cavitation Forum 2011, University of Warwick*.

[59] Iben, U., A. Morozov, E. Winklhofer, and F. Wolf (2011). Laser-pulse interferometry applied to high-pressure fluid flow in micro channels. *Experiments in fluids 50*(3), 597–611.

[60] Iben, U., F. Wolf, H.-A. Freudigmann, J. Fröhlich, and W. Heller (2015). Optical measurements of gas bubbles in oil behind a cavitating micro-orifice flow. *Experiments in Fluids 56*(6), 114.

[61] Kastengren, A. L., C. F. Powell, T. Riedel, S.-K. Cheong, K.-S. Im, X. Liu, Y. J. Wang, and J. Wang (2008). Nozzle geometry and injection duration effects on diesel sprays measured by X-ray radiography. *Journal of Fluids Engineering 130*(4), 041301.

[62] Kastengren, A. L., F. Z. Tilocco, C. F. Powell, J. Manin, L. M. Pickett, R. Payri, T. Bazyn, and others (2012). Engine combustion network (ECN): measurements of nozzle geometry and hydraulic behavior. *Atom. Sprays 22*(12), 1011–1052.

[63] Kjeldsen, M., R. E. Arndt, and M. Effertz (2000). Spectral characteristics of sheet/cloud cavitation. *Journal of Fluids Engineering 122*(3), 481–487.

[64] Koren, B. (1993). *A robust upwind discretization method for advection, diffusion and source terms*. Centrum voor Wiskunde en Informatica Amsterdam.

[65] Koukouvinis, P., M. Gavaises, J. Li, and L. Wang (2016). Large Eddy Simulation of Diesel injector including cavitation effects and correlation to erosion damage. *Fuel 175*, 26–39.

[66] Koukouvinis, P., N. Mitroglou, M. Gavaises, M. Lorenzi, and M. Santini (2017). Quantitative predictions of cavitation presence and erosion-prone locations in a high-pressure cavitation test rig. *Journal of Fluid Mechanics 819*, 21–57.

[67] Lauterborn, W. and H. Bolle (1975). Experimental investigations of cavitation-bubble collapse in the neighbourhood of a solid boundary. *Journal of Fluid Mechanics 72*(2), 391–399.

[68] Le, Q., J.-P. Franc, and J. M. Michel (1993). Partial cavities: global behavior and mean pressure distribution. *TRANSACTIONS-AMERICAN SOCIETY OF MECHANICAL ENGINEERS JOURNAL OF FLUIDS ENGINEERING 115*, 243–243.

[69] Lemmon, E. W., M. L. Huber, and M. O. McLinden (2013). NIST Reference Fluid Thermodynamic and Transport Properties-REFPROP, version 9.1, National Institute of Standards and Technology, Gaithersburg, MD. *www. ni st. gov/srd/nist23. cfm*.

[70] Lichtarowicz, A. (1972). Use of a simple cavitating nozzle for cavitation erosion testing and cutting. *Nature 239*(91), 63–64.

[71] Lichtarowicz, A., R. K. Duggins, and E. Markland (1965). Discharge coefficients for incompressible non-cavitating flow through long orifices. *Journal of Mechanical Engineering Science 7*(2), 210–219.

[72] Martynov, S. B., D. J. Mason, and M. R. Heikal (2006). Numerical simulation of cavitation flows based on their hydrodynamic similarity. *International Journal of Engine Research 7*(3), 283–296.

[73] Mauger, C., L. Méès, M. Michard, A. Azouzi, and S. Valette (2012). Shadowgraph, Schlieren and interferometry in a 2d cavitating channel flow. *Experiments in fluids 53*(6), 1895–1913.

[74] Mewis, F. and H. Klug (2004). The challenge of very large container ships: a hydrodynamic view. In *9th Symposium on practical design of ships and other floating structures*, pp. 173–181.

[75] Mihatsch, M. S. (2016). *Numerical prediction of erosion and degassing effects in cavitating flows*. Ph. D. thesis, Technische Universität München.

[76] Mihatsch, M. S., S. J. Schmidt, and N. A. Adams (2015). Cavitation erosion prediction based on analysis of flow dynamics and impact load spectra. *Physics of Fluids (1994-present) 27*(10), 103302.

[77] Mitroglou, N., M. Gavaises, J. M. Nouri, and C. Arcoumanis (2011). Cavitation inside enlarged and real-size fully transparent injector nozzles and its effect on near nozzle spray formation. In *DIPSI Workshop 2011. Droplet Impact Phenomena & Spray Investigations*, pp. 33–45. Università degli studi di Bergamo.

[78] Mitroglou, N., M. Lorenzi, M. Santini, and M. Gavaises (2016). Application of X-ray micro-computed tomography on high-speed cavitating diesel fuel flows. *Experiments in Fluids 57*(11), 175.

[79] Momma, T. and A. Lichtarowicz (1995). A study of pressures and erosion produced by collapsing cavitation. *Wear 186*, 425–436.

[80] Nurick, W. H. (1976). Orifice cavitation and its effect on spray mixing. *Journal of fluids engineering 98*(4), 681–687.

[81] Ooi, K. K. (1985). Scale effects on cavitation inception in submerged water jets: a new look. *Journal of Fluid Mechanics 151*, 367–390.

[82] Oosthuizen, P. H. and W. E. Carscallen (1997). *Compressible fluid flow*. McGraw-Hill,.

[83] Örley, F., S. Hickel, S. J. Schmidt, and N. A. Adams (2016). Large-Eddy Simulation of turbulent, cavitating fuel flow inside a 9-hole Diesel injector including needle movement. *International Journal of Engine Research*, 195–211.

[84] Örley, F., T. Trummler, S. Hickel, M. S. Mihatsch, S. J. Schmidt, and N. A. Adams (2015). Large-eddy simulation of cavitating nozzle flow and primary jet break-up. *Physics of Fluids 27*(8), 086101.

[85] Pauchet, J., A. Retailleau, and J. Woillez (1992). The prediction of cavitation inception in turbulent water jets. In *Cavitation and Multiphase Flow Forum, SED*, Volume 135, pp. 149–158.

[86] Philipp, A. and W. Lauterborn (1998). Cavitation erosion by single laser-produced bubbles. *Journal of Fluid Mechanics 361*, 75–116.

[87] Pickett, L. M. and D. L. Siebers (2004). Soot in diesel fuel jets: effects of ambient temperature, ambient density, and injection pressure. *Combustion and Flame 138*(1), 114–135.

[88] Pollack, G. L. (1991). Why gases dissolve in liquids. *Science 251*(4999), 1323–1330.

[89] Powell, C. F., S. A. Ciatti, S.-K. Cheong, J. Liu, and J. Wang (2004). X-ray absorption measurements of diesel sprays and the effects of nozzle geometry. Technical report, SAE Technical Paper.

[90] Purwar, H., S. Idlahcen, L. Méès, C. Rozé, J.-B. Blaisot, M. Michard, and D. Maligne (2016). Simultaneous high-speed internal and external flow measurements for a high-pressure diesel nozzle. *arXiv preprint arXiv:1609.03853*.

[91] Rayleigh, L. (1917). *On the pressure developed in a liquid during the collapse of a spherical cavity: Philosophical Magazine Series 6, 34, 94–98*.

[92] Reid, B. A., G. K. Hargrave, C. P. Garner, and R. M. McDavid (2013). An optical comparison of the cavitation characteristics of diesel and bio-diesel blends in a true-scale nozzle geometry. *International Journal of Engine Research 14*(6), 622–629.

[93] Reif, K. (2014). *Diesel engine management*. Springer.

[94] Reitz, R. D. and F. V. Bracco (1982). Mechanism of atomization of a liquid jet. *Physics of Fluids (1958-1988) 25*(10), 1730–1742.

[95] Salvador, F. J., J. Martínez-López, J.-V. Romero, and M.-D. Roselló (2013). Computational study of the cavitation phenomenon and its interaction with the turbulence developed in diesel injector nozzles by Large Eddy Simulation (LES). *Mathematical and Computer Modelling 57*(7), 1656–1662.

[96] Schmidt, D. P., C. J. Rutland, and M. L. Corradini (1997). A numerical study of cavitating flow through various nozzle shapes. Technical report, SAE Technical Paper.

[97] Schmidt, D. P., C. J. Rutland, and M. L. Corradini (1999). A fully compressible, two-dimensional model of small, high-speed, cavitating nozzles. *Atomization and sprays 9*(3).

[98] Schmidt, S. J., I. H. Sezal, G. H. Schnerr, and M. Thalhamer (2008). Riemann techniques for the simulation of compressible liquid flows with phase-transition at all Mach numbers-shock and wave dynamics in cavitating 3-D micro and macro systems. In *46th AIAA aerospace sciences meeting and exhibit*, pp. 7–10.

[99] Schnerr, G. H., I. H. Sezal, and S. J. Schmidt (2008). Numerical investigation of three-dimensional cloud cavitation with special emphasis on collapse induced shock dynamics. *Physics of Fluids (1994-present) 20*(4), 040703.

[100] Schnerr, G. H., C. Vortmann, and J. Sauer (2000). Numerical studies of flow in fuel injector nozzles–interaction of separation and cavitation. *Transient Phenomena in Multiphase and Multicomponent Systems: Research Report*, 335–350.

[101] Schrank, K., H. Murrenhoff, and C. Stammen (2013). Measurements of air absorption and air release characteristics in hydraulic oils at low pressure. In *ASME/BATH 2013 Symposium on fluid power and motion control*.

[102] Sezal, I. H., S. J. Schmidt, G. H. Schnerr, M. Thalhamer, and M. Förster (2009). Shock and wave dynamics in cavitating compressible liquid flows in injection nozzles. *Shock waves 19*(1), 49–58.

[103] Soteriou, C., R. Andrews, and M. Smith (1995). Direct injection diesel sprays and the effect of cavitation and hydraulic flip on atomization. Technical report, SAE technical paper.

[104] Sou, A., S. Hosokawa, and A. Tomiyama (2007). Effects of cavitation in a nozzle on liquid jet atomization. *International journal of heat and mass transfer 50*(17), 3575–3582.

[105] Strotos, G., P. Koukouvinis, A. Theodorakakos, M. Gavaises, and G. Bergeles (2015). Transient heating effects in high pressure Diesel injector nozzles. *International Journal of Heat and Fluid Flow 51*, 257–267.

[106] Vogel, A., W. Lauterborn, and R. Timm (1989). Optical and acoustic investigations of the dynamics of laser-produced cavitation bubbles near a solid boundary. *Journal of Fluid Mechanics 206*, 299–338.

[107] Voss, M. (2002). *Numerische, theoretische und experimentelle Untersuchungen zur Kavitationsblasendynamik*. Ph. D. thesis.

[108] Wrona, F. (2005). *Simulation von kavitierenden Strömungen in Hochdrucksystemen*. Ph. D. thesis.

[109] Yuan, W., J. Sauer, and G. H. Schnerr (2001). Modeling and computation of unsteady cavitation flows in injection nozzles. *Mécanique & industries 2*(5), 383–394.

[110] Yuan, W. and G. H. Schnerr (2003). Numerical simulation of two-phase flow in injection nozzles: Interaction of cavitation and external jet formation. *Journal of Fluids Engineering 125*(6), 963–969.